REVIEW

Electrode materials and reaction mechanisms in solid oxide fuel cells: a brief review. III. Recent trends and selected methodological aspects

Ekaterina V. Tsipis · Vladislav V. Kharton

Abstract Continuing previous reviews on mixed-conducting electrodes for intermediate-temperature solid oxide fuel cells (IT SOFCs), this work presents a short overview of novel cathode and anode materials, their electrochemical performance in contact with oxygen anion- and proton-conducting solid electrolytes, and specific features determining possible applications. Priority was given mainly to recent research reports published during the last 2–5 years. Particular emphasis is focused on the relevant methodological aspects, potential limitations and drawbacks, and factors affecting electrode polarization and durability. Typical ranges of the polarization resistances, overpotentials, power densities in the cells with various current collectors, and the electrode materials total conductivity and thermal expansion are compared. The electrode compositions appraised in single-chamber and micro-SOFCs, hydrocarbon- and carbon-fueled cells, high-temperature electrolyzers, and other solid-electrolyte appliances are briefly covered in light of their similarity to the common SOFC materials discussed in the previous parts.

E. V. Tsipis
Chemistry Department, Instituto Tecnológico e Nuclear,
CFMC-UL,
EN 10,
2686-953 Sacavém, Portugal

V. V. Kharton (✉)
Department of Ceramics and Glass Engineering, CICECO,
University of Aveiro,
3810-193 Aveiro, Portugal
e-mail: kharton@ua.pt

Introduction

The progress in the field of solid-state electrochemical devices operating at elevated temperatures, such as solid oxide fuel cells (SOFCs), steam and carbon dioxide electrolyzers, oxygen and hydrogen pumps, and a variety of ceramic reactors, sensors, and analytical appliances, requires continuous search for novel electrode and solid-electrolyte materials with advanced properties, optimization of their fabrication and processing technologies, and efforts to deeper understand the electrochemical reaction mechanisms [1–8]. In particular, the problems associated with relatively high costs of SOFCs and their degradation can be partially solved by decreasing the operation temperatures down to so-called intermediate-temperature (IT) range, 770–1070 K, which makes it possible to use less expensive components, to decrease the role of chemical interaction and thermomechanical incompatibility of the fuel cell stack materials, to facilitate miniaturization, and to improve efficiency of the kilowatt-scale generators [4–10]. On the other hand, lowering the operation temperature leads also to a greater role of electrode polarization which may become critical for the overall performance. This tendency, the approaches to improve electrode properties in the IT range, and the major limitations originating from technological and materials science-related factors all are quite similar for the SOFC-based power generators and other electrochemical devices based on oxygen ion- or proton-conducting solid electrolytes. The present work is centered on the comparative analysis of electrochemical behavior, conductivity, stability, and thermal expansion of the electrode materials recently reported as promising for the fuel cells and electrolyzers. Relevant methodological aspects, potential limitations and drawbacks, and performance of the electrochemical cells are also briefly covered. As for the

previous parts [7, 8], no attempt for a complete overview of all novel compositions, microstructural designs and device configurations, or for a thorough analysis of the microscopic reaction mechanisms was made in this brief review. Furthermore, since priority is given to novel results, in some cases the scarce and preliminary information available in the recent literature may lead to a need for additional investigations and validation employing complementary experimental methods. The references were selected in order to show typical relationships between properties of various electrode materials and systems reported during the last 2–5 years and, in general, to reflect state-of-the-art in this attractive field.

Novel cathode materials: selected compositions and trends

Up to now, the highest level of electrochemical activity under the SOFC cathodic conditions is known for cobalt-containing oxide phases with ABO_3 perovskite structure and their derivatives. With respect to other compositional families, porous cathodes made of perovskite-related cobaltites exhibit minimum overpotentials (η) and area-specific polarization resistances (R_η); representative values are compared in Tables 1 and 2 and Figs. 1, 2, 3, and 4. Consequently, despite the poor thermomechanical compatibility with other cell materials due to very high thermal and chemical expansion, perovskite-type cobaltites are being widely appraised for the IT SOFC cathodes [11, 12, 37, 40–45]. In addition to the fabrication of composite cathodes containing solid-electrolyte components, the standard approaches to suppress thermal and chemical expansivity include an extensive substitution of cobalt and A-site doping which enable, in particular, to decrease oxygen nonstoichiometry variations in the cobaltite lattice. These strategies lead often to lower electronic and ionic conductivities, whereas the polarization resistance may increase or exhibit a minimum at moderate doping levels.

As an example, porous $Sm_{0.5}Sr_{0.5}CoO_{3-\delta}$ cathode in contact with $Ce_{0.8}Sm_{0.2}O_{2-\delta}$ (CSO20) electrolyte was reported to undergo fast degradation both on thermal cycling and during isothermal operation [40]. The partial substitution of cerium for cobalt in $Sm_{1-x}Sr_xCoO_{3-\delta}$ was shown to slightly suppress the lattice expansion, to decrease total conductivity, and to improve cathode performance; however, the cerium solubility limit is low, ≤5 mol% [37]. The highest electrochemical performance of single SOFCs, fabricated with $R_{0.6}Sr_{0.4}Co_{1-x}Fe_xO_{3-\delta}$ (R=La, Nd; x=0, 0.5) perovskite cathodes, $Ce_{0.9}Gd_{0.1}O_{2-\delta}$ (CGO10) interlayer, thin 8 mol% yttria-stabilized zirconia (8YSZ) electrolyte, and Ni–8YSZ anodes via tape casting, co-firing, and screen printing, was achieved for $La_{0.6}Sr_{0.4}CoO_{3-\delta}$ providing a

maximum power density (P_{max}) of ~550 mW cm^{-2} at 1073 K [41]. The substitution of Nd for La and Fe for Co in $R_{0.6}Sr_{0.4}Co_{1-x}Fe_xO_{3-\delta}$, improving the materials compatibility, results in a worse fuel cell performance. Notice that the negative effect of iron incorporation is much more pronounced in comparison with A-site doping [41]. Moreover, the thermal and chemical expansion of iron-substituted cobaltites remains high [8].

For $SrCo_{1-x}Sb_xO_{3-\delta}$ cathodes applied onto $Ce_{0.8}Nd_{0.2}O_{2-\delta}$ (CNO20) electrolyte, the composition with x=0.05 was found to exhibit the highest conductivity and the lowest polarization resistance, varying from 0.009 to 0.23 Ωcm^2 at 873–1173 K [11]. The stabilization of tetragonal (x=0.05–0.15) or cubic (x=0.2) perovskite-like structures suppresses abrupt changes in the lattice expansion at elevated temperatures, characteristic of the parent strontium cobaltite due to phase transitions associated with thermal disorder and oxygen stoichiometry variations [11]. The apparent thermal expansion coefficient (TEC) tends, however, to increase with x, reaching 29.3×10^{-6} K^{-1} at 673–1273 K and x=0.15 [11]. Similar effects were found in the $SrCo_{1-x}Nb_xO_{3-\delta}$ system considered for potential cathode applications in lanthanum gallate-based cells [42]. For the tetragonal double perovskite $Sr_2Co_{1-x}Fe_xNbO_{5+\delta}$, the total conductivity and cathode performance decrease with increasing x [12]. Doping of $SrCoO_{3-\delta}$ with iron stabilizes the perovskite structure, but does not reduce the lattice expansivity down to the level appropriate for electrode applications in the fuel cells with common solid electrolytes, such as YSZ, gadolinia- or samaria-doped ceria (CGO/CSO), and strontium- and magnesium-codoped lanthanum gallate (LSGM) [7, 8]. Sr (Co,Fe)$O_{3-\delta}$ and its analogs exhibit also extensive oxygen vacancy ordering processes on cooling and on modest reduction, finally resulting in the formation of brownmillerite-type phases with significantly lower ionic and electronic conduction. As partial substitution of Ba for Sr suppresses vacancy ordering and lowers the oxygen content variations, a significant attention is drawn to the (Ba, Sr)(Co,Fe)$O_{3-\delta}$ system, particularly $Ba_{0.5}Sr_{0.5}Co_{0.8}Fe_{0.2}O_{3-\delta}$ (BSCF) [13, 43, 44, 46–49]. On the other hand, the problems of interaction between the cathode material and CO_2 and/or water vapor, which become very important in the IT range, increase on barium incorporation [46]. Furthermore, the cubic BSCF perovskite was demonstrated to gradually decompose into a perovskite phase mixture on cooling in air below 1173 K [47–49], making the use of BSCF questionable. The apparent TEC of $Ba_{0.5}Sr_{0.5}Co_{1-x}Fe_xO_{3-\delta}$ (x=0.2–0.8) contributed by chemical expansivity achieves 29.8×10^{-6} K^{-1} at 298–1273 K and $p(O_2)=10^{-5}$ atm, depending on sample prehistory [49]. This may be responsible for the minimum polarization resistance observed at rather low (1173 K) sintering temperature of such electrodes applied onto CGO10 electrolyte [44].

Table 1 Properties of selected cobaltite- and ferrite-based cathode materials in air

Composition	$\sigma^{1073\,K}$ (S/cm)	Average TEC		Polarization resistance at 1073 K		Reference
		T (K)	$\alpha \times 10^6$ (K^{-1})	Electrolyte	R_η (Ω cm^2)	
$SrCo_{0.95}Sb_{0.05}O_{3-\delta}$	178	673–1273	19.35	CNO20	0.02	[11]
$Sr_2Co_{0.9}Fe_{0.1}NbO_{6-\delta}$	5.7			CGO10	0.34[a]	[12]
$La_{0.5}Sr_{0.5}Co_{0.8}Fe_{0.2}O_{3-\delta}$				LSGM(10 20)	0.23	[13]
$PrBa_{0.5}Sr_{0.5}Co_2O_{5+\delta}$		1173		CGO10	0.05	[14]
$SmBa_{0.5}Sr_{0.5}Co_2O_{5+\delta}$		973	21.9	CGO10	0.02	[14]
		1173	22.9	8YSZ	1.35	
				8YSZ/CGO10 interlayer	0.01	
$Sm_{0.5}Sr_{0.5}CoO_{3-\delta}$				LSGM(10 20)	0.18	[13]
$Sm_{0.5}Sr_{0.5}Co_{0.8}Fe_{0.2}O_{3-\delta}$				LSGM(10 20)	0.26	[13]
$GdBa_{0.5}Sr_{0.5}Co_2O_{5+\delta}$		1173		CGO10	0.05	[14]
$Ba_2CoMo_{0.5}Nb_{0.5}O_{6-\delta}$	1.2	873–1173	18.7	CSO20	0.05[a]	[15]
				LSGM(10 20)	0.04	[13]
$Ba_{1.2}Sr_{0.8}CoO_{4+\delta}$				CGO10	0.3	[16]
$YBaCo_4O_{7+\delta}$	74	750–1273	7.61	LSGM(9.8 20)	0.08	[17, 18]
$YBaCo_{3.2}Fe_{0.8}O_{7+\delta}$		750–1273	10	LSGM(9.8 20)	0.11	[17]
$YBaCo_3ZnO_{7+\delta}$	19	293–1273	7.43	CGO20	0.05	[19, 20]
				CGO20	0.26	[21]
$TbBaCo_3ZnO_{7+\delta}$		298–1173	9.45	CGO20	0.07	[21]
$Ca_3Co_4O_{9-\delta}$		1093	10	CGO10	0.68[a]	[22]
$Sr_{0.9}K_{0.1}FeO_{3-\delta}$	26			LSGM(20 17)	0.2[b]	[23]
$(La_{0.8}Sr_{0.2})_{0.95}Fe_{0.8}Ni_{0.2}O_{3-\delta}$				CGO10	0.5	[24]

$\sigma^{1073\,K}$ is the total conductivity at 1073 K. α is the linear TEC averaged in the given temperature range

8YSZ 8 mol% Y_2O_3-stabilized ZrO_2 ($Zr_{0.85}Y_{0.15}O_{1.93}$), *CGO10* $Ce_{0.9}Gd_{0.1}O_{1.95}$, *CGO20* $Ce_{0.8}Gd_{0.2}O_{1.9}$, *CSO20* $Ce_{0.8}Sm_{0.2}O_{1.9}$, *CNO20* $Ce_{0.8}Nd_{0.2}O_{1.9}$, *LSGM(10 20)* $La_{0.9}Sr_{0.1}Ga_{0.8}Mg_{0.2}O_{3-\delta}$, *LSGM(20 17)* $La_{0.8}Sr_{0.2}Ga_{0.83}Mg_{0.17}O_{3-\delta}$, *LSGM(9.8 20)* $(La_{0.9}Sr_{0.1})_{0.98}Ga_{0.8}Mg_{0.2}O_{3-\delta}$

[a] Extrapolated

[b] Estimated from the polarization curve

If compared to the disordered perovskite analogs, substantially lower TECs are characteristic of the layered cobaltites where the state of Co cations is often more stable (Table 1). While the $A_{n+1}B_nO_{3n+1}$ Ruddlesden–Popper (RP)-type phases containing cobalt in the B sublattice suffer from an insufficient thermodynamic stability under the SOFC cathode fabrication and operation conditions, a substantially high mixed conductivity and fast oxygen exchange kinetics are known also for other layered cobaltites, such as the double perovskites $A_2CoBO_{5+\delta}$ (A = Sr, Ba; B = Nb, Mo) and $RBaCo_2O_{5+\delta}$ (R = Pr, Gd, Y), and heavily doped $YBaCo_4O_{7+\delta}$ [8, 12, 14–21, 38, 50–55]. Typical electrochemical properties of these materials are illustrated in Figs. 1, 2, 3, 4, and 5 and in Table 1. In particular, the B-site cation-ordered double perovskite $Ba_2CoMo_{0.5}Nb_{0.5}O_{5+\delta}$ has a considerably lower total conductivity (σ) compared to BSCF but exhibits a similar electrochemical activity, a better structural stability due to the presence of higher-valence cations in the B sublattice, and a reduced reactivity with CSO20 [15]. The electrode

layers of the A-site cation-ordered $PrBaCo_2O_{5+\delta}$ applied onto CSO20 electrolyte showed an area-specific resistance of 0.4 Ω cm^2 at 873 K in air [50]. Fast surface exchange and substantially high oxygen diffusivity in the IT range were reported for $GdBaCo_2O_{5+\delta}$, leading to an excellent cathode performance [38] (Fig. 3). Analogously, the polarization resistance of $SmBa_{0.5}Sr_{0.5}Co_2O_{5+\delta}$ electrodes sintered on CGO10 substrates at 1273 K was as low as 0.092 Ω cm^2 at 973 K [14] (Fig. 5). On the contrary, $Ba_{1.2}Sr_{0.8}CoO_{4+\delta}$ with K_2NiF_4-type structure [16] shows a worse performance compared to the perovskite-type cobaltites in contact with ceria-based electrolytes. Similar trends are known for the RP-type nickelate families where the electronic conductivity and electrochemical activity both tend to decrease with increasing concentration of the A-site cations, forming rock-salt like $(AO)_2$ layers in the crystal lattice [8]. For nickelate and cuprate systems, the compounds with K_2NiF_4-type structure are often considered for the cathode applications as their thermodynamic stability is maximum compared to other ternary compounds such as

Table 2 Properties of selected Ni-, Cu-, and Mn-containing cathode materials in air

Composition	$\sigma^{1073\ K}$ (S/cm)	Average TEC		Polarization resistance		Reference
		T (K)	$\alpha \times 10^6$ (K^{-1})	Electrolyte	R_η^{1073K} (Ω cm^2)	
$La_2NiO_{4+\delta}$	59	548–1173	13.8	LSGM(10 20)	2.0	[25, 26]
	76.4	400–1290	13.6			[27, 28]
$La_3Ni_2O_{7-\delta}$	52[a]	548–1173	13.7	LSGM(10 20)	1.5	[25, 26]
$La_4Ni_3O_{10-\delta}$	86[a]	548–1173	13.5	LSGM(10 20)	0.9	[25, 26]
				LSAO	2.2	[28]
$La_4Ni_{2.9}Cu_{0.1}O_{10-\delta}$				LSAO	1.6	[28]
$La_{3.95}Sr_{0.05}Ni_2CoO_{10-\delta}$				LSAO	2.7	[28]
$La_2Ni_{0.9}Co_{0.1}O_{4\pm\delta}$				LSGM(10 20)	0.6	[25]
$La_2Ni_{0.8}Cu_{0.2}O_{4+\delta}$	64.6	400–1240	13.3	LSGM(9.8 20)	0.62	[29, 30]
		323–1273	13.9	LSGM(10 20)	2.8	[31]
				8YSZ	6.1	[31]
				LSAO	1.54	[30]
$La_2Ni_{0.5}Cu_{0.5}O_{4+\delta}$	31.9	300–900	13.4	LSGM(9.8 20)	1.6	[28]
		900–1370	14.5	LSAO	2.2	
$La_2CuO_{4+\delta}$	6.3	323–1273	10.6	LSGM(10 20)	5.3	[31]
$Pr_2Ni_{0.8}Cu_{0.2}O_{4+\delta}$	167.9	300–1030	13.2	LSGM(9.8 20)	0.29	[27]
		1030–1150	17.5			
		1210–1280	12.9			
$La_{1.9}Sm_{0.1}NiO_{4\pm\delta}$	82			LSGM(20 20)	3.1	[25]
$La_{0.95}Sr_{0.05}NiO_{4\pm\delta}$				CGO10	0.65	[32]
$LaSr_2Mn_{1.6}Ni_{0.4}O_{7-\delta}$	22.2	300–900	12.5	LSAO	24	[28]
		900–1370	14.4			
$Gd_{0.6}Ca_{0.4}Mn_{0.9}Ni_{0.1}O_{3-\delta}$	137.7	550–900	10.8	LSAO	20	[28]
		900–1370	12.1			
$Sr_{0.7}Ce_{0.3}Mn_{0.9}Cr_{0.1}O_{3-\delta}$	296.8	550–950	12.0	LSAO	10.2	[28]
		950–1370	15.1			
$SrMn_{0.6}Nb_{0.4}O_{3-\delta}$	18.9	300–800	11.3	LSAO	31	[28]
		800–1200	12.3			

LSGM(20 20) $La_{0.8}Sr_{0.2}Ga_{0.8}Mg_{0.2}O_{3-\delta}$, *LSAO* $La_{10}Si_5AlO_{26.5}$

[a] Porous samples

perovskite; the situation in the cobaltite systems is opposite. This factor, in combination with relatively high concentration of alkaline earth metal cations, leads usually to a fast interaction of K_2NiF_4-type cobaltites, such as $Ba_{1.2}Sr_{0.8}CoO_{4+\delta}$, with carbon dioxide and water vapor present in atmospheric air. Regardless of the structural and thermodynamic factors, the fabrication of composite cathodes comprising cobaltite and solid-electrolyte components enables to lower thermomechanical strains, to enlarge the electrochemical reaction zone, and thus to improve electrode performance (Fig. 6).

The results discussed above make it necessary to add several comments regarding methodological aspects of the cathode tests. First of all, the measurements of cathodic polarization resistance are usually performed in model cells where the geometric electrode-surface area is 0.5–10 cm^2

and precise determination of low R_η values (<0.01–0.05 Ω cm^2) is often difficult. In fact, the integral polarization resistance in these conditions becomes comparable to the resistances of current collectors, leads, and electrical contacts, leading to the necessity to decrease electrode area. For porous electrode layers, this possibility is, however, limited due to rising role of the boundary conditions and current distribution inhomogeneities; dense microelectrodes provide an excellent tool to study electrochemical reaction mechanisms, but their behavior may substantially differ from that of the porous cathodes (e.g., [58]). Second, in many literature reports on the novel electrode materials, their appraisal is based on total conductivity data and electrochemical performance observed in various model cells. A number of critical aspects, such as thermodynamic stability under the potential
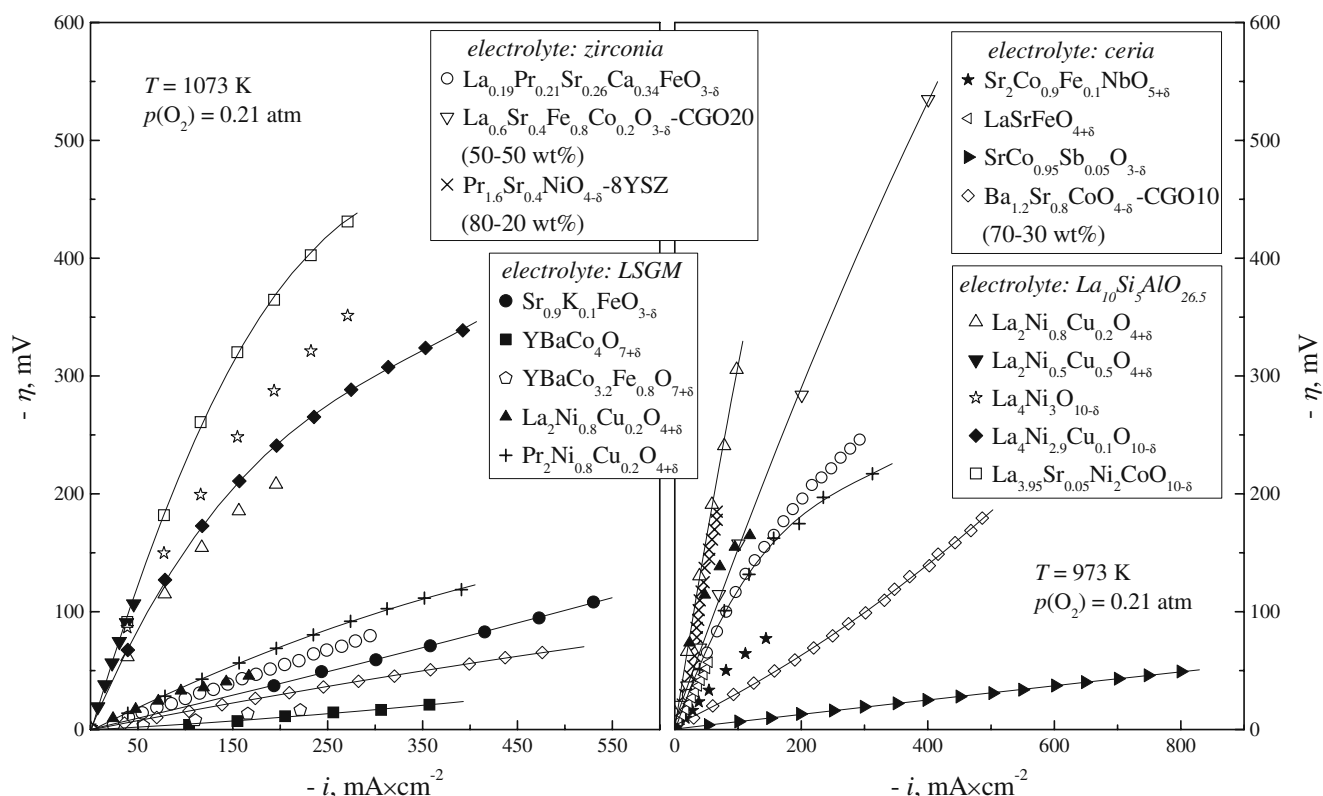
Fig. 1 Comparison of the cathodic overpotentials of various half-cells with porous mixed-conducting electrodes at 1073 K (*left*) and 973 K (*right*) in air [11, 12, 16–18, 23, 27–30, 33–36]. Zirconia-based electrolytes are 8YSZ (8 mol% Y_2O_3-stabilized ZrO_2) or SSZ (Sc_2O_3-stabilized ZrO_2). Ceria-based electrolytes include CGO10 ($Ce_{0.9}Gd_{0.1}O_{1.95}$), CGO20 ($Ce_{0.8}Gd_{0.2}O_{1.9}$), CSO10 ($Ce_{0.9}Sm_{0.1}O_{1.95}$), and CNO20 ($Ce_{0.8}Nd_{0.2}O_{1.9}$). The composition of Sr- and Mg-codoped lanthanum gallate (LSGM) is $(La_{0.9}Sr_{0.1})_{0.98}$-$Ga_{0.8}Mg_{0.2}O_{3-\delta}$ or $La_{0.8}Sr_{0.2}Ga_{0.83}Mg_{0.17}O_{3-\delta}$; 4–6-μm-thick samaria-doped ceria interlayer between the $La_{0.19}Pr_{0.21}Sr_{0.26}Ca_{0.34}$-$FeO_{3-\delta}$ electrode and solid-electrolyte membrane was used in [33]

application conditions and lattice expansivity, become thus excluded from consideration. For example, the apparent TECs of the A-site cation-ordered cobaltites with double perovskite structure are still high, limiting their compatibility with common solid electrolytes [18]; the cobaltites with other layered structures possess often a lower stability compared to their perovskite-type analogs and undergo various phase transitions on thermal and redox cycling [8, 17, 18, 51, 53, 54]. Another source of possible degradation phenomena may appear when the cations that form highly volatile oxides at intermediate temperatures in oxidizing atmospheres (e.g., Sb, Mo, V, Bi, or K) are present in the cathode. Appraisal of such materials requires, at least, long-term stability tests under the operation conditions. Also, the use of X-ray diffraction (XRD) analysis of the powder mixtures after heat treatments, without other complementary techniques, is often insufficient for any conclusion regarding negligible interaction of the components, such as perovskite cobaltites and doped ceria in the composite cathodes, when no new phases can be formed but cation interdiffusion between the phases may be significant. The interfacial and transport properties of ceria-based solid electrolytes and mixed-conducting composites are very sensitive to local inhomogeneities, which may even appear in thin surface layers of ceria grains due to the incorporation of tri- and divalent cations from the perovskite phase [59, 60]. In such cases, electron microscopy and diffraction studies in combination with thermodynamic analysis are often desirable.

Oxide materials derived from recently discovered RBa-Co_4O_7 (R = lanthanide or Y), whose crystal structure consists of closely packed alternating triangular and Kagomé layers of corner-sharing Co tetrahedra, attract a growing interest due to their unusual oxygen sorption and transport properties [17–21, 53, 54]. Porous $YBaCo_4O_7$-based cathodes exhibit very high electrochemical activity in contact with doped $LaGaO_3$ and ceria solid electrolytes at 873–1073 K (Figs. 1, 2, 3, 4, and 6). However, at atmospheric oxygen pressure, $YBaCo_4O_7$-based compounds appear thermodynamically stable only above approximately 1123–1173 K and metastable at lower temperatures. A slow oxygen uptake at 1000–1200 K causes complete decomposition of $YBaCo_4O_{7+\delta}$ into a mixture of perovskite-like phases and binary oxides when

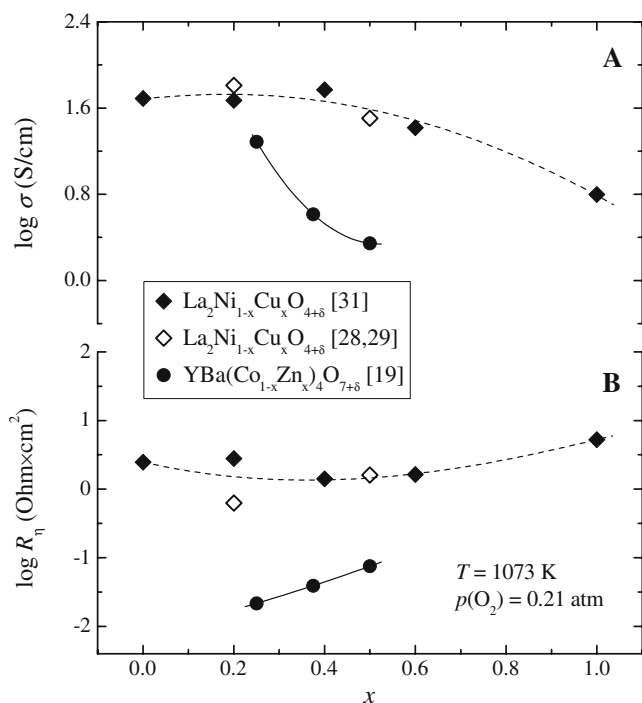Fig. 2 Composition dependencies of the total electrical conductivity of YBa(Co$_{1-x}$Zn$_x$)$_4$O$_{7+\delta}$ [19] and La$_2$Ni$_{1-x}$Cu$_x$O$_{4+\delta}$ [28, 29, 31] (a) and cathodic polarization resistance of YBa(Co$_{1-x}$Zn$_x$)$_4$O$_{7+\delta}$–Ce$_{0.8}$Gd$_{0.2}$O$_{1.9}$ (50–50 wt.%) composite electrodes applied onto Ce$_{0.8}$Gd$_{0.2}$O$_{1.9}$ [19] and La$_2$Ni$_{1-x}$Cu$_x$O$_{4+\delta}$ in contact with LSGM [28, 29, 31] (b)
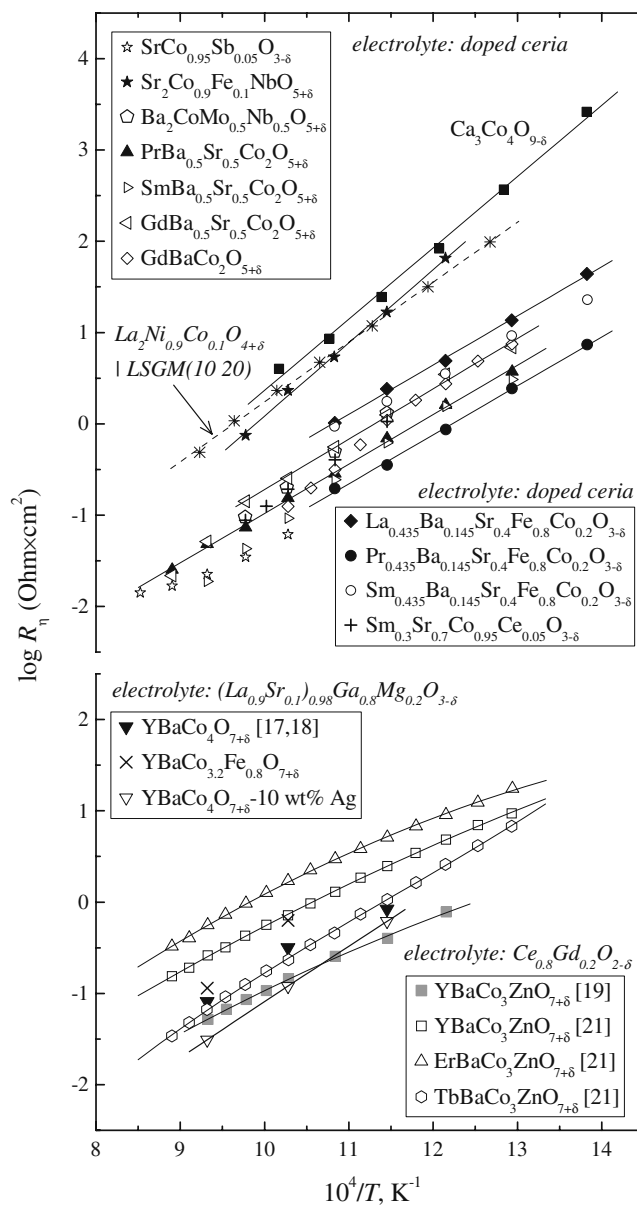

Fig. 3 Temperature dependencies of the area-specific polarization resistance of cobalt-containing cathodes in contact with ceria- and LSGM-based solid electrolytes in air [11, 12, 14, 15, 17–19, 21, 22, 25, 37–39]

the average cobalt oxidation state approaches 3+; the decomposition is accompanied by a conductivity jump and dramatic volume contraction presenting a serious drawback for electrochemical applications. In the RBa(Co, M)$_4$O$_{7+\delta}$ (R = Y, Er, Tb, Ca, In, and M = Zn, Fe, Al) series, several compositions such as YBaCo$_{4-x}$Zn$_x$O$_{7+\delta}$ (1≤x≤2) were found stable at the SOFC operation temperatures and thermomechanically compatible with the electrolyte materials [19–21]. Although the substitution of Zn^{2+} for Co$^{2+/3+}$ decreases electronic conductivity and cathode performance (Figs. 2 and 3), YBaCo$_3$ZnO$_{7+\delta}$ and composite YBa-Co$_3$ZnO$_{7+\delta}$–CGO20 (50–50 wt.%) cathodes under open-circuit conditions exhibit low R_η values, comparable to those of the materials derived from perovskite-type cobaltites, whereas the cathodic overpotentials seem rather high [19, 20]. The electrochemical activity of porous RBa-Co$_3$ZnO$_{7+\delta}$ electrodes increases in the sequence Er < Y < Tb ([21]; Figs. 3 and 4). While wide practical use of the terbium-containing electrodes may hardly be expected due to economic reasons, the latter trend indicates a possibility to improve performance of RBa(Co,M)$_4$O$_{7+\delta}$ electrodes by partial substitution of R^{3+}. The misfit compound Ca$_3$Co$_4$O$_{9-\delta}$, where the crystal structure is built of alternating CdI2-type and rock-salt slabs, also shows moderate expansion and was proposed as a promising cathode

material [22]. The performance of porous Ca$_3$Co$_4$O$_{9-\delta}$ electrodes is similar to that of layered nickelates (Figs. 3 and 7) and can be improved by CGO10 additions. In the case of Ca$_3$Co$_4$O$_{9-\delta}$ and RBa(Co,Zn)$_4$O$_{7+\delta}$, further assessment of thermal stability and possible interaction with the gaseous species present in air are, however, necessary.

As for the cobaltite-based materials, perovskite-type ferrites exhibit very high thermal and chemical expansion limiting their electrode applications. In the case of R$_{0.5}$AE$_{0.5}$FeO$_{3-\delta}$ (R = La–Sm; AE = Sr, Ba) perovskites, increasing the difference between R^{3+} and AE^{2+} cation radii increases oxygen deficiency and lowers ionic and electronic
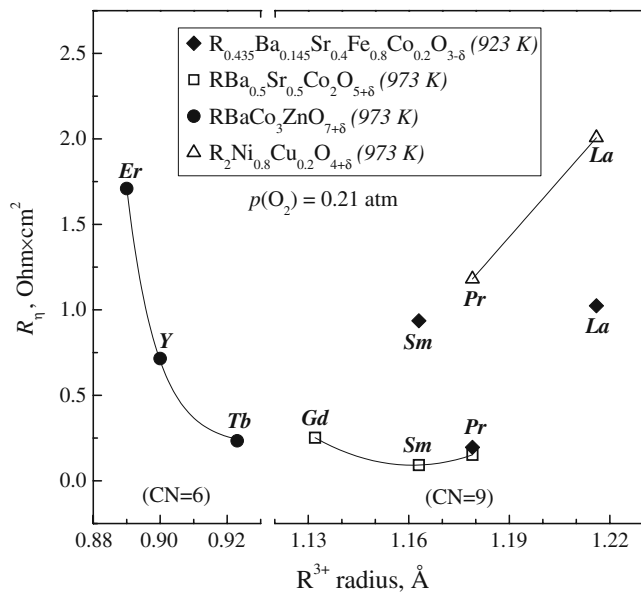
Fig. 4 Comparison of the polarization resistances vs. radius of A-site cations (R^{3+}) for ferrite- and cobaltite-based cathodes in contact with gadolinia-doped ceria (CGO) [14, 21, 39] and nickelate-based cathodes in contact with $(La_{0.9}Sr_{0.1})_{0.98}Ga_{0.8}Mg_{0.2}O_{3-\delta}$ [27, 29]. *CN* coordination number of R^{3+}

Fig. 6 Polarization resistances of CGO-containing composite cathodes in contact with $Ce_{0.9}Gd_{0.1}O_{1.95}$ (CGO10) [14, 16] and $Ce_{0.8}Gd_{0.2}O_{1.9}$ (CGO20) [20] solid electrolytes at 973 K and TECs of $SmBa_{0.5}Sr_{0.5}Co_2O_{5+\delta}$–CGO10 composite ceramics [14], in air

conductivities, whereas the role of surface exchange kinetics in the oxygen permeation processes tends to decrease on Ba^{2+} doping and on decreasing R^{3+} size in $R_{0.5}Sr_{0.5}FeO_{3-\delta}$ series [62]. In correlation with this behavior, the incorporation of Ba^{2+} reduces polarization resistance of $R_{0.58-x}Ba_xSr_{0.4}Fe_{0.8}Co_{0.2}O_{3-\delta}$ (R = La, Pr, Sm) electrodes in contact with ceria-based electrolyte [39]; the
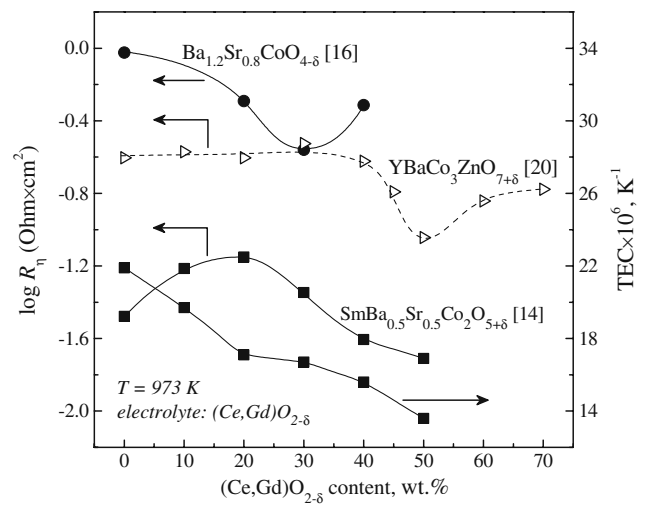
best performance observed for $x=0.145$ and R = Pr is close to the level of undoped cobaltites (Figs. 3 and 4). The total conductivity and cathode performance of rhombohedral $R_{0.5}AE_{0.5}FeO_{3-\delta}$ (R = La and/or Pr; AE = Sr, Ca or/and Ba) was reported to increase with average A-site cation radius [63]. Very interesting results [33] were obtained on the mixed solid solutions $R_{1-x}AE_xFeO_{3-\delta}$ (R = La, Pr, Nd; AE = Ca, Sr), synthesized fixing the average A-site cation radius and cation size mismatch in order to isolate the effect of divalent dopant concentration from the steric effects. The
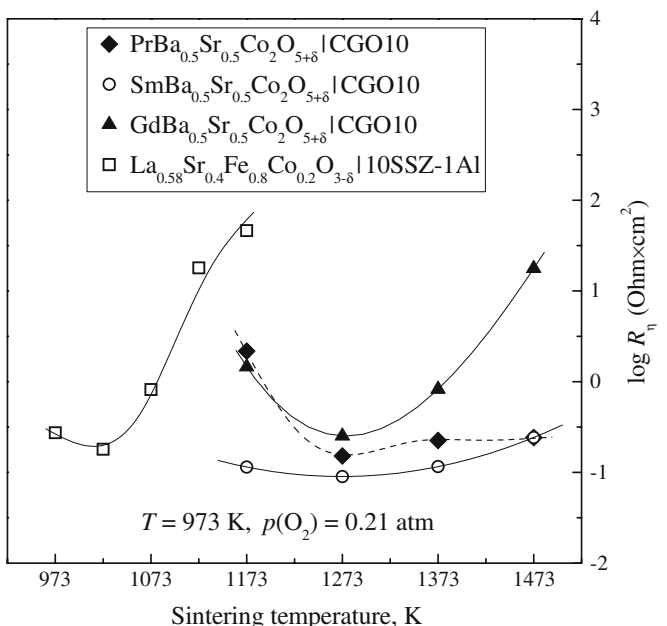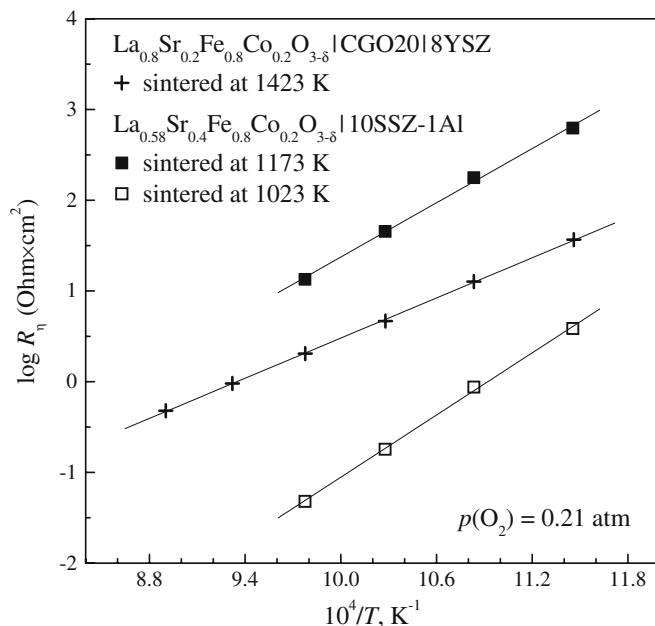

Fig. 5 Comparison of the area-specific polarization resistances of cobaltite [14] and ferrite-cobaltite cathodes [56, 57], deposited onto solid-electrolyte surface and sintered at various temperatures. 10SSZ-1Al corresponds to 89 mol% ZrO_2–10 mol% Sc_2O_3–1 mol% Al_2O_3
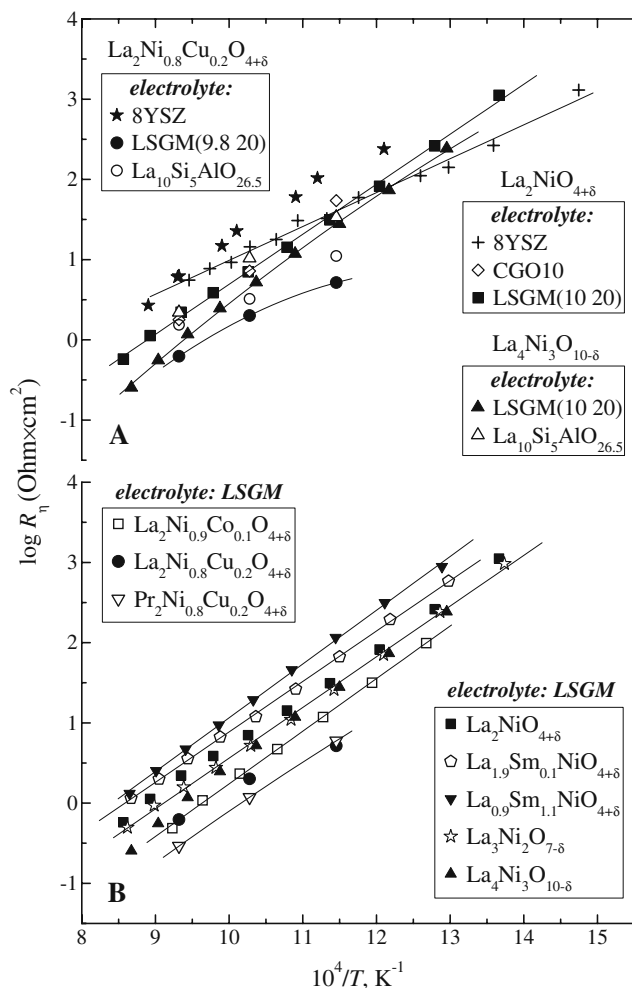
Fig. 7 Temperature dependencies of the polarization resistance of porous [25–31, 61] and cone-shaped [32] nickelate cathodes in contact with various solid electrolytes in air

maximum total conductivity, predominantly p-type electronic in air, was found for $La_{0.19}Pr_{0.31}Sr_{0.26}Ca_{0.24}FeO_{3-\delta}$ ceramics, whereas minimum cathodic overpotentials in contact with scandia-stabilized zirconia (SSZ) and CSO were observed for $La_{0.19}Pr_{0.21}Sr_{0.26}Ca_{0.34}FeO_{3-\delta}$ [33], thus indicating correlations with the oxygen vacancy ordering processes rather than with electronic transport. For $La_{0.8}AE_{0.2}FeO_{3-\delta}$ (AE = Ca, Sr, Ba), the highest ionic conductivity and lowest polarization resistance of the composite cathodes calcined at 1373 K were found for $La_{0.8}Sr_{0.2}FeO_{3-\delta}$ [64]. Quite low overpotentials (Fig. 1) and high power densities (Table 3) were observed in the model cells with $La_{0.8}Sr_{0.2}Ga_{0.83}Mg_{0.17}O_{3-\delta}$ (LSGM(20 17)) solid electrolyte and porous electrodes of Co-free $Sr_{0.9}K_{0.1}FeO_{3-\delta}$ perovskite [23]. The effects of potassium doping on the phase stability and interaction with the electrolyte membranes and also potential volatilization and hydration phenomena require, however, a careful evaluation. It should also be mentioned that, as for cobaltite-based materials,

improved thermomechanical properties can be expected for the layered ferrite phases where, again, increasing concentration of the A-site cations may raise stability problems. As a particular example, at 973 K, the $LaSrFeO_{4+\delta}$ porous electrode layers sintered onto CSO10 at 1273 K show an open-circuit polarization resistance of 3.95 Ω cm^2 and cathodic overpotential of −57 mV at the current density of −55 mA cm^{-2} [34]. These values are close to other materials with K_2NiF_4-type structure (Table 2; Fig. 1).

The incorporation of $Ni^{2+/3+}$ and Cu^{2+} cations in the cobaltite- and ferrite-based perovskites is often used as a suitable strategy to optimize their properties, in particular thermal expansion, total conductivity, and sinterability. Note that effects of these dopants on the electronic and ionic transport depend on the concentration of other acceptor-type substituents in the perovskite lattice; the perovskite phase stability tends to decrease on doping [8, 90–94]. For comparison, the polarization resistance of $(La_{0.6}Sr_{0.4})_{0.99}Co_{0.9}Ni_{0.1}O_{3-\delta}$ and $(La_{0.8}Sr_{0.2})_{0.99}Co_{0.8-}Ni_{0.2}O_{3-\delta}$ electrodes in contact with CGO10 electrolyte is approximately 0.1 Ω cm^2 at 973 K in air [91]. The introduction of Sr^{2+} in perovskite-type $La_{1-y}Sr_yFe_{1-x}Ni_xO_{3-\delta}$ increases the oxygen deficiency and ionic transport at elevated temperatures but leads to a lower stability as reflected by narrowing the solid solution domain at 1373 K down to $x\approx0.25$ at $y=0.10$ and $x\approx0.12$ at $y=0.20$ in air [92]. The average TECs of $La_{1-y}Sr_yFe_{1-x}Ni_xO_{3-\delta}$ ($x=0.1$–0.4, $y=0.1$–0.2) vary in the ranges (12.4–13.4)× 10^{-6} K^{-1} at 700–1150 K and (14.2–18.0)×10^{-6} K^{-1} at 1150–1370 K, rising with strontium and nickel content. These additives increase total conductivity, whereas the substitution of nickel for iron has a weak negative effect on the ionic conduction, suggesting the defect cluster formation involving oxygen vacancies and Ni^{2+} [92]. Perovskite-type $(La_{1-y}Sr_y)_zFe_{1-x}M_xO_{3-\delta}$ ($x=0.2$–0.8; $y=0.2$—0.4; $z=$ 0.8–1.1; M = Ni, Cu) were proposed as alternative SOFC cathode materials [24, 95, 96]. However, the initial performance and long-term stability of $(La_{0.8}Sr_{0.2})_{0.95}Fe_{0.8-}Ni_{0.2}O_{3-\delta}$ are both inferior with respect to (La,Sr)(Fe,Co) $O_{3-\delta}$ cathodes [24]. For $(La_{0.8}S_{0.2})_{0.95}Fe_{1-x}M_xO_{3-\delta}$, the substitution level is limited by the dopant solubility, close to 20 mol% Ni or Cu. Doping with copper and decreasing z in $(La_{1-y}Sr_y)_zFe_{1-x}M_xO_{3-\delta}$ lower the melting point and, consequently, the sintering temperature [95, 96]. These factors make it possible to suppress interaction with solid-electrolyte ceramics, but may also promote microstructural instability of the porous electrodes at the SOFC operation temperatures. As for many other perovskite electrodes [8], the A-site cation deficiency in $(La_{1-y}Sr_y)_zFe_{1-x}M_xO_{3-\delta}$ is favorable to decrease thermal expansion and reactivity with 8YSZ. The Ni-substituted materials exhibit the highest conductivity in these compositional families but possess also a higher reactivity with YSZ if compared to the parent

Table 3 Examples of the maximum power density in various single SOFCs

Cathode	Anode	Electrolyte/thickness	Fuel	T (K)	P_{max} (mW cm^{-2})	Reference
$Sm_{0.5}Sr_{0.5}CoO_{3-\delta}$	$Ni_{9.6}Fe$ (10 wt.% Fe_2O_3 coated NiO)	LSGM(10 20), 6 μm|CSO20, 0.5 μm	Wet H_2	973	1.79	[65]
$La_{0.6}Sr_{0.4}CoO_{3-\delta}$–CGO10 (50–50 wt.%)	Ni–CGO10 (50 wt.% NiO), Ni_6Fe_7 support	CGO10/25 μm	H_2	923	0.68	[66]
$SrCo_{0.8}Fe_{0.2}O_{3-\delta}$	$Ni_{3.8}Fe$–CSO20 (50–50 wt.%)	LSGM(20 17)/0.3 mm, CSO20 interlayer	Wet H_2	1073; 973	1.43; 0.62	[67]
$SrCo_{0.8}Fe_{0.2}O_{3-\delta}$	CoFe–CSO20 (50–50 wt.%)	LSGM(20 17)/0.3 mm, CSO20 interlayer	Wet H_2	1073	1.07	[68]
$Sm_{0.5}Sr_{0.5}Fe_{0.8}Co_{0.2}O_{3-\delta}$	$Ce_{0.8}Fe_{0.2}O_{2-\delta}$	LSGM/0.88 mm	Wet CH_4	1073	0.05	[69]
$La_{0.6}Sr_{0.4}CoO_{3-\delta}$	$La_{0.2}Sr_{0.7}TiO_{3-\delta}$ (CGO20+Cu)-infiltrated	8YSZ/75 μm	Wet H_2	1023	0.50	[70]
$La_{0.65}Sr_{0.3}MnO_{3-\delta}$–8YSZ (50–50 wt.%)	$Sr_{0.88}Y_{0.08}TiO_3$–8YSZ (50–50 wt.%), $(CeO_{2-\delta}+Ru)$-infiltrated	8YSZ/10 μm	H_2; 10 ppm H_2S–H_2	1073	0.51; 0.47	[71]
$La_{0.65}Sr_{0.3}MnO_{3-\delta}$–8YSZ (50–50 wt.%)|LSM	$La_{0.4}Sr_{0.6}Ti_{0.4}Mn_{0.6}O_{3-\delta}$–8YSZ (65–35 vol.%)	8YSZ/0.2 mm	Wet H_2; Wet CH_4	1129	0.43[a]; 0.06	[72]
$La_{0.6}Sr_{0.4}Fe_{0.8}Co_{0.2}O_{3-\delta}$–CGO10|LSFC	$La_{0.8}Sr_{0.2}Cr_{0.82}Ru_{0.18}O_{3-\delta}$	LSGM(10 20)/0.4 mm	Wet H_2	1073	0.53	[73]
$Gd_{0.4}Sr_{0.6}CoO_{3-\delta}$	$(La_{0.75}Sr_{0.25})_{0.95}Cr_{0.5}Mn_{0.5}O_{3-\delta}$	LSGMCo/0.6 mm	Wet H_2	1123	0.30[a]	[74]
$SrCo_{0.8}Fe_{0.2}O_{3-\delta}$	$La_{0.75}Sr_{0.25}Cr_{0.5}Mn_{0.5}O_{3-\delta}$	LSGM(20 17)/0.3 mm, CLO interlayer	Dry H_2; Dry CH_4	1123	0.21; 0.10	[75]
$SrCo_{0.8}Fe_{0.2}O_{3-\delta}$	$La_{0.75}Sr_{0.25}Cr_{0.5}Mn_{0.5}O_{3-\delta}$	LSGM(20 17)/0.25 mm	Dry H_2; Dry CH_4	1073; 1123	0.18; 0.25	[76]
$La_{0.75}Sr_{0.25}Cr_{0.5}Mn_{0.5}O_{3-\delta}$	$La_{0.75}Sr_{0.25}Cr_{0.5}Mn_{0.5}O_{3-\delta}$	LSGM(10 20)/1.5 mm	Wet 5% H_2	1073	0.05	[13]
$Ba_{0.5}Sr_{0.5}Co_{0.8}Fe_{0.2}O_{3-\delta}$	$La_{0.75}Sr_{0.25}Cr_{0.5}Mn_{0.5}O_{3-\delta}$		Wet 5% H_2	1073	0.12	[13]
$La_{0.8}Sr_{0.2}MnO_{3\pm\delta}$	$La_{0.75}Sr_{0.25}Cr_{0.5}Mn_{0.5}O_{3-\delta}$	LSGM(10 20)/0.12 mm	Wet H_2	1073	0.57	[77]
$(La,Sr)MnO_{3\pm\delta}$	$La_{0.75}Sr_{0.25}Cr_{0.5}Mn_{0.5}O_{3-\delta}$	8YSZ/0.25 mm	Wet H_2	1173	0.28	[78]
$La_{0.8}Sr_{0.2}MnO_{3\pm\delta}$	$La_{0.75}Sr_{0.25}Cr_{0.5}Mn_{0.5}O_{3-\delta}$	YSZ/83 μm	Dry H_2; Dry CH_4	1123	0.20; 0.03	[79]
CSO20-infiltrated	$La_{0.75}Sr_{0.25}Cr_{0.5}Mn_{0.5}O_{3-\delta}$ CSO20-infiltrated		Dry H_2; Dry CH_4	1123	0.40; 0.08	
	$La_{0.75}Sr_{0.25}Cr_{0.5}Mn_{0.5}O_{3-\delta}$ Ni-infiltrated		Dry H_2; Dry CH_4	1123	1.00; 0.36	
	$La_{0.75}Sr_{0.25}Cr_{0.5}Mn_{0.5}O_{3-\delta}$ (CSO20+Ni)-infiltrated		Dry H_2; Dry CH_4	1123	1.14; 0.42	
$La_{0.75}Sr_{0.25}Cr_{0.5}Mn_{0.5}O_{3-\delta}$–YSZ graded	$La_{0.8}Sr_{0.2}MnO_{3\pm\delta}$–YSZ graded	YSZ/0.3 mm, CGO20 interlayer	Wet H_2; Wet CH_4	1173	0.47; 0.2	[80]
Pt	$La_{0.75}Sr_{0.25}Cr_{0.5}Mn_{0.5}O_{3-\delta}$–YSZ (50–50 wt.%)	YSZ/1 mm	CH_4; C_2H_5OH	1073	0.02; 0.01	[81]
Pt	$La_{0.75}Sr_{0.25}Cr_{0.5}Mn_{0.5}O_{3-\delta}$–YSZ (50–50 wt.%), Pd-infiltrated	YSZ/1 mm	CH_4; C_2H_5OH	1073	0.05; 0.11	

Table 3 (continued)

Cathode	Anode	Electrolyte/thickness	Fuel	T (K)	P_{max} (mW cm^{-2})	Reference
$La_{0.8}Sr_{0.2}FeO_{3-\delta}$–YSZ (40–60 wt.%)	$La_{0.8}Sr_{0.2}Cr_{0.5}Mn_{0.5}O_{3-\delta}$–YSZ (45–65 wt.%)	YSZ/60 μm	Wet H_2	973	0.11	[82]
$La_{0.8}Sr_{0.2}FeO_{3-\delta}$–YSZ (40–60 wt.%)	$La_{0.8}Sr_{0.2}Cr_{0.5}Mn_{0.5}O_{3-\delta}$–YSZ (45–65 wt.%), Pd-infiltrated	YSZ/60 μm	Wet H_2	973	0.50	[82]
$La_{0.8}Sr_{0.2}MnO_{3\pm\delta}$–YSZ (50–50 wt.%)	8YSZ impregnated with Cu-$La_{0.75}Sr_{0.25}Cr_{0.5}Mn_{0.5}O_{3-\delta}$ (35–65 wt.%)	8YSZ/50 μm	Dry H_2	1073	0.21	[83]
			CH_4		0.06	
			C_4H_{10}		0.13	
$SrCo_{0.8}Fe_{0.2}O_{3-\delta}$	Cu–$La_{0.75}Sr_{0.25}Cr_{0.5}Mn_{0.5}O_{3-\delta}$ (20–80 wt.%)	LSGM(20 17)/0.3 mm, CLO interlayer	Dry H_2	1123	0.86	[75]
			Dry CH_4		0.48	
$SrCo_{0.8}Fe_{0.2}O_{3-\delta}$	Cu–$La_{0.75}Sr_{0.25}Cr_{0.5}Mn_{0.5}O_{3-\delta}$ (20–80 wt.%), sputtered Pt	LSGM(20 17)/0.25 mm	Dry H_2	1123	0.85	[76]
			Dry CH_4		0.52	
$Pr_{0.7}Ca_{0.3}Cr_{0.6}Mn_{0.4}O_{3-\delta}$	$Pr_{0.7}Ca_{0.3}Cr_{0.6}Mn_{0.4}O_{3-\delta}$	8YSZ/0.37 mm	Wet H_2	1223	0.25	[84]
			Wet CH_4	1223	0.16	
$La_{0.8}Sr_{0.2}Sc_{0.2}Mn_{0.8}O_{3+\delta}$	$La_{0.8}Sr_{0.2}Sc_{0.2}Mn_{0.8}O_{3-\delta}$	10SSZ/0.3 mm	Wet H_2	1173	0.31	[85]
			Wet CH_4	1173	0.13	
$La_{0.6}Sr_{0.4}Fe_{0.8}Co_{0.2}O_{3-\delta}$–CGO10 (50–50 wt.%)	$LaSr_2Fe_2CrO_{9-\delta}$–CGO10 (50–50 wt.%)	CGO10/0.3 mm	Wet H_2	1073	0.30	[86]
$Sr_{0.9}K_{0.1}FeO_{3-\delta}$		LSGM(10 20)/0.4 mm	Wet H_2	1073	0.37	
	$Sr_2MgMoO_{6-\delta}$	LSGM(20 17)/0.3 mm	H_2	1073	0.68	[34]
$SrCo_{0.8}Fe_{0.2}O_{3-\delta}$	$Sr_2MgMoO_{6-\delta}$	LSGM(20 17)/0.3 mm, CLO4 interlayer	Dry H_2	1073	0.84	[87, 88]
			Wet H_2		0.81	
			Dry CH_4		0.44	
			Wet CH_4		0.35	
$La_{0.6}Sr_{0.4}Fe_{0.2}Co_{0.8}O_{3-\delta}$	$Sr_2MgMoO_{6-\delta}$	LSGM(20 20)/0.6 mm with CGO20 interlayer	Wet H_2	1073	0.27	[89]
			Wet H_2		0.33	
$SrCo_{0.8}Fe_{0.2}O_{3-\delta}$	$Sr_2MnMoO_{6-\delta}$	LSGM(20 17)/0.3 mm, CLO4 interlayer	Dry H_2	1073	0.65	[87, 88]
			5 ppm H_2S–H_2		0.57	
$SrCo_{0.8}Fe_{0.2}O_{3-\delta}$	$Sr_2Mg_{0.9}Cr_{0.1}MoO_{6-\delta}$	LSGM(20 17)/0.3 mm interlayer	Dry H_2	1073	0.79	
			5 ppm H_2S–H_2		0.61	
$SrCo_{0.8}Fe_{0.2}O_{3-\delta}$	$Sr_{1.2}La_{0.8}MgMoO_{6-\delta}$	LSGM(20 17)/0.3 mm, CLO5 interlayer	Dry CH_4	1073	0.47	[89]
			Wet CH_4		0.49	
			Wet C_2H_6		0.19	
			Wet C_3H_8		0.17	

In most cases, "wet H_2" and "wet CH_4" correspond to the gas humidified under ambient conditions (~3% H_2O)

10SSZ 10 mol% Sc_2O_3-stabilized ZrO_2, CLO5 $Ce_{0.4}La_{0.5}O_{2-\delta}$, CLO4 $Ce_{0.6}La_{0.4}O_{2-\delta}$, LSGMCo $La_{0.8}Sr_{0.2}Ga_{0.8}Mg_{0.15}Co_{0.05}O_{3-\delta}$

[a] Extrapolated

ferrites, a result of reduced thermodynamic stability of the doped perovskite phases; no indication of chemical reaction or cation interdiffusion between $(La_{0.8}Sr_{0.2})_{0.95}Fe_{0.8}Ni_{0.2}O_{3-\delta}$ and gadolinia-doped ceria (CGO) was revealed by XRD [96, 97]. At the same time, despite the lower electrical conductivity, $La_{0.8}Sr_{0.2}FeO_{3-\delta}$ was reported to provide a higher electrode performance than $La_{0.7}Sr_{0.3}Fe_{0.8}Ni_{0.2}O_{3-\delta}$ and $LaNi_{0.6}Fe_{0.4}O_{3-\delta}$ applied onto YSZ with CSO20 interlayer [98]. The effect of A-site cation nonstoichiometry on the electrochemical activity of $La_{1-\lambda}Fe_{0.4}Ni_{0.6}O_{3-\delta}$ was investigated using model cone-shaped electrodes and CGO10 electrolyte [98]; increasing λ results in a separation of NiO, inhibiting the oxygen reduction reaction.

The main advantages of RP-type nickelates $(R,Sr)_{n+1}Ni_nO_{3n+1}$ (R = La, Pr, Nd) whose structure is built of n perovskite-like layers alternating with one rock-salt sheet are moderate TECs and very low chemical expansivity in combination with substantially high mixed conductivity [8, 9, 25–27, 29, 31, 32, 61, 99–102]. The electrochemical behavior of these materials is illustrated in Figs. 1, 2, 4, and 7; Table 2 lists the values of TECs, total conductivity, and polarization resistance for selected compositions. Increasing n leads usually to higher ionic and electronic conduction [25–27]. These effects are associated with increasing concentration of Ni–O–Ni bonds responsible for the electronic transport, progressive delocalization of the p-type electronic charge carriers, higher dimensionality of the electron and ion transfer, and increasing vacancy migration contribution to the oxygen ion diffusivity. Note that, except for oxygen hyperstoichiometric $La_2NiO_{4+\delta}$ and its analogs where anion diffusion is essentially dominated by the interstitial migration, most RP nickelates are oxygen-deficient at elevated temperatures [103, 104]. As a particular consequence, the electrochemical activity of $La_{n+1}Ni_nO_{3n+1-\delta}$ cathodes becomes substantially higher when n increases from 1 to 3 [25, 26]. Analogous trends are known for praseodymium nickelate electrodes where $Pr_4Ni_3O_{10-\delta}$ is formed due to oxidative decomposition of undoped [61] or Cu-doped [27] $Pr_2NiO_{4+\delta}$ phase with K_2NiF_4-like structure. Modest A-site deficiency was found to decrease the polarization resistance of $Nd_{1-x}NiO_{4+\delta}$ porous layers in contact with 8YSZ solid electrolyte [61]. An opposite trend was, however, reported in [99] where $La_3Ni_2O_{7-\delta}$ cathode was found to show higher over-potentials than $La_2NiO_{4+\delta}$ in contact with CSO20–2 mol% Co-doped ceramics. When discussing this behavior, one should note that the relatively high concentration of A-site cations in the RP phases compared to their perovskite-type analogs may substantially influence topotactic reactions and cation interdiffusion with solid-electrolyte membranes, as for the other factors including the Gibbs free energy of formation of the electrode material phase or the presence of high-diffusivity additives. As an example, the reaction

between $La_2Ni_{1-x}Cu_xO_{4+\delta}$ (x=0–1) and 8YSZ yielding insulating $La_2Zr_2O_7$ pyrochlore is observed at rather low temperatures, such as 1173 K [31]. The interaction becomes more pronounced with increasing x, leading to cathode performance deterioration [31]. Consequently, the layered nickelate-cuprate electrodes should preferably be used in contact with other solid electrolytes (Fig. 7a) when no blocking layers are formed at the electrode/electrolyte interface, and/or in combination with protective interlayers.

The factors related to the electrode–electrolyte interaction and interdiffusion processes become crucial in the case of silicate-based solid electrolytes, such as apatite-type $La_{10-x}(SiO_4)_6O_{2\pm\delta}$ and their derivatives. These electrolytes possess a substantially high oxygen ionic conductivity, moderate thermal expansion, low electronic conduction in a wide range of oxygen chemical potentials, and low costs, thus making it possible to consider them for potential use in SOFCs and other electrochemical devices [105–107]. The performance of mixed-conducting cathodes in contact with silicate ceramics is, however, worse in comparison with other solid electrolytes; the high polarization resistance originates primarily from the surface diffusion of silica, partially blocking the electrochemical reaction zone, without formation of secondary phases detectable by XRD [28, 30]. From the thermodynamic point of view, silica spreading may be promoted when moisture is present in air supplied into the cathode chamber. These processes explain very poor performance of $La_{0.75}Sr_{0.25}Mn_{0.8}Co_{0.2}O_{3-\delta}$-based cathode layers co-sintered with $La_9SrSi_6O_{26.5}$ electrolyte at 1673 K, when no diffusion of the electrode components into the apatite membrane was detected [108]. The electrochemical behavior of a large series of porous cathodes, including $La_{0.8}Sr_{0.2}Fe_{0.8}Co_{0.2}O_{3-\delta}–Ce_{0.8}Gd_{0.2}O_{1.9}$ (CGO20), $La_{0.7}Sr_{0.3}MnO_{3-\delta}–CGO20$, $SrMn_{0.6}Nb_{0.4}O_{3-\delta}$, $Sr_{0.7}Ce_{0.3}Mn_{0.9}Cr_{0.1}O_{3-\delta}$, $Gd_{0.6}Ca_{0.4}Mn_{0.9}Ni_{0.1}O_{3-\delta}$, $La_2Ni_{1-x}Cu_xO_{4+\delta}$ (x=0.2–0.5), $La_2Ni_{0.8}Cu_{0.2}O_{4+\delta}–Ag$, $LaSr_2Mn_{1.6}Ni_{0.4}O_{7-\delta}$, $La_4Ni_{3-x}Cu_xO_{10-\delta}$ (x=0–0.1), and $La_{3.95}Sr_{0.05}Ni_2CoO_{10-\delta}$, was studied at 873–1073 K in contact with $La_{10}Si_5AlO_{26.5}$ electrolyte [28, 30]. While the level of ionic conductivity in the latter apatite-type phase is higher than that of YSZ in the intermediate-temperature range [107], in all cases the polarization resistances and overpotentials of nickelate-based cathodes are substantially higher than those of similar layers applied onto LSGM. Examples are presented in Figs. 1, 7a, and 8 and in Table 2. As compared to the intergrowth nickelate materials, the polarization of manganite-based electrodes is high (Fig. 8), in correlation with the lower values of oxygen ionic and electronic conductivities [28]. The performance of mixed-conducting cathodes applied onto $La_{10}Si_5AlO_{26.5}$ can be improved by reducing the temperature used for electrode sintering [30]. Qualitatively similar results were obtained for $La_{0.8}Sr_{0.2}MnO_{3\pm\delta}$, $La_{0.7}Sr_{0.3}FeO_{3-\delta}$, $La_{0.6}Sr_{0.4}Co_{0.2}$-
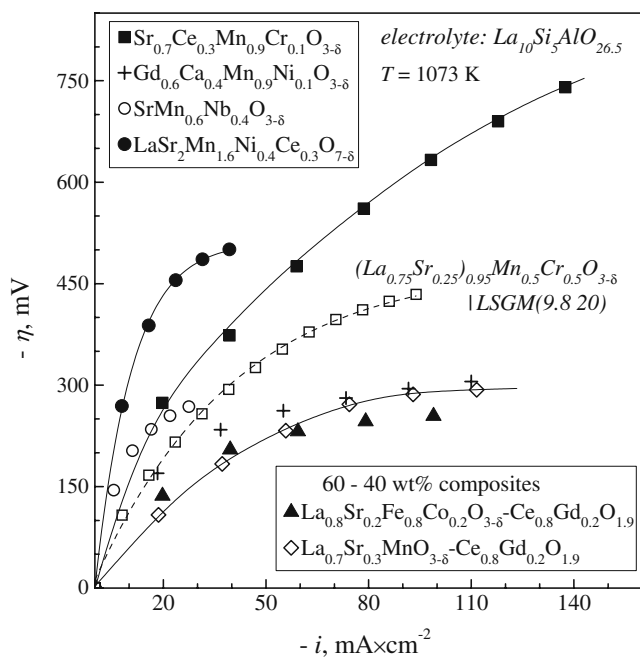
Fig. 8 Cathodic polarization curves of Fe-, Cr-, and Mn-containing electrode layers in contact with apatite-type $La_{10}Si_5AlO_{26.5}$ solid electrolyte [28, 30]. The data on $(La_{0.75}Sr_{0.25})_{0.95}Cr_{0.5}Mn_{0.5}O_{3-\delta}$ applied onto $(La_{0.9}Sr_{0.1})_{0.98}Ga_{0.8}Mg_{0.2}O_{3-\delta}$ electrolyte [109] are shown for comparison. Pt mesh current collectors were used in all cases

$Fe_{0.8}O_{3-\delta}$, and $La_{0.6}Sr_{0.4}Co_{0.8}Fe_{0.2}O_{3-\delta}$ cathodes in contact with $La_{10}Si_{5.5}Al_{0.5}O_{26.75}$ solid electrolyte [110]. Since processing of dense silicate ceramics usually requires very high temperatures, a number of attempts were made to optimize the fabrication conditions of apatite-based electrochemical cells. In the case of tape casting and co-sintering of $La_9SrSi_6O_{26.5}$ electrolyte and $La_{0.75}Sr_{0.25}Mn_{0.8}Co_{0.2}O_{3-\delta}$ cathode at 1673 K, no cation diffusion was detected by energy-dispersive spectroscopy [111]; at the same time, silica spreading and electrode poisoning may still be expected to play an important role. The anode-supported single SOFCs were fabricated by atmospheric DC plasma spraying of $La_{9.7}(Si_{5.7}Mg_{0.3})O_{26.3}$ films onto $Ni–La_{9.7}(Si_{5.7}Mg_{0.3})O_{26.3}$ substrates, followed by heat treatments in a reducing atmosphere [112]; the cell with $La_{0.6}Sr_{0.4}Fe_{0.8}Co_{0.2}O_{3-\delta}$ cathode showed power densities of 22–80 mW/cm^2 at 873–1073 K with 50% H_2–50% Ar fuel. As for the silicate solid electrolytes, significant limitations associated with the cell materials interaction can be envisaged when using Bi_2O_3-containing electrodes, although the exceptionally high ionic conductivity and fast surface exchange of bismuth oxide-based materials are advantageous for the electrochemical reaction kinetics [113]. As an example, at 973 K, the area-specific polarization resistance of undoped, 5 mol% Ca- and 5 mol% Sr-doped $Bi_2Ru_2O_7$ pyrochlore electrodes in contact with ceria-based electrolyte was 1.45, 1.24, and 1.41 Ω cm^2, respectively [114]. Additions of 20 mol% erbia-stabilized δ-Bi_2O_3 (31–44 wt%) further reduce the electrode

resistance down to 0.08–0.11 Ω cm^2 [114]. Due to high reactivity and high thermal expansion of Bi_2O_3-containing materials, the latter family of electrode compositions seems more promising for the electrochemical cells based on doped $Bi_4V_2O_{11}$ (BIMEVOX) solid electrolytes [113, 115].

Cermet and oxide SOFC anodes

The major approaches in the developments of SOFC anode materials include an optimization of cermet compositions and microstructures, involving graded electrode layers and nano-structured components, and a search for novel oxide phases with high electrochemical activity, a sufficient electronic conductivity and improved tolerance to various poisoning phenomena, and stable in a wide range of oxygen chemical potentials [5, 7, 8, 10, 116–118]. Continuous attention is therefore drawn to the cermets containing Ni and ceria-based components. The use of ceria is often necessary to suppress carbon deposition and to promote hydrocarbon oxidation; in addition, reduced $CeO_{2-\delta}$-based solid solutions exhibit mixed oxygen ionic and n-type electronic conductivity that can be moderately enhanced by acceptor-type doping [115]. At the same time, ceria-based anodes without any metallic component display quite a poor performance, even when current collectors of Au ink and Pt paste are used [13, 69]. The electrochemical activity of $Ni–Ce_{0.8}Ti_{0.2}O_{2-\delta}$ (60 wt.% NiO) was found higher compared to $Ni–CeO_{2-\delta}$ cermet anode in 10% CH_4-containing fuel, a result of higher conductivity of the doped ceria [119]. A $Ni–Cu–CeO_{2-\delta}$ (14–16–70 vol.%) anode sintered at a reduced temperature, 1173 K, onto CGO10 electrolyte displayed $R_\eta < 0.1$ Ω cm^2 at 873 K in wet 50% H_2 [120]. The incorporation of redox-stable components with moderate thermal expansion, such as YSZ, is often desirable to reduce the role of dimensional instabilities caused by the local $p(O_2)$ variations and minor TEC mismatch (e.g., [8, 28] and references cited). Taking into account the durability issues related to carbon deposition and sulfur poisoning, numerous efforts are centered on decreasing nickel content in the cermets and on the use of other transition metals and alloys. Representative examples are given in Figs. 9 and 10 and in Table 3. The anode assemblies consisting of one Ni–CGO10 functional layer and a $Ni–La_{0.9}Mn_{0.8}Ni_{0.2}O_{3-\delta}$ contact layer were proposed to reduce nickel content [125]. The redox tolerance appraisal at 1123 K showed that the driving force for the anode performance degradation is nickel agglomeration, occurring if even Ni content is below the percolation threshold. Although nickel should be reduced under anodic conditions and should segregate from $La_{0.9}Mn_{0.8}Ni_{0.2}O_{3-\delta}$, the perovskite structure was kept after 100 redox cycles using 50% H_2O–H_2 [125]. Quantum mechanical calculations employing

density functional theory to calculate the stability of surface-adsorbed hydrogen atoms, oxygen atoms, and hydroxyl radicals for a variety of metals (Mn, Fe, Co, Ni, Cu, Ru, Rh, Pd, Ag, Pt, Au) showed that the anode electrochemical activity should be highest for Ni that has an intermediate oxygen adsorption energy [126]. The activity was found to decrease when oxygen binding energy increases (Ru, Co, Fe, Mn) and decreases (Rh, Pd, Pt, Au), without correlations with the stability of surface-adsorbed hydrogen [126]. The copper-based anodes in combination with ceria catalysts, which may be of interest for hydrocarbon-fueled SOFCs due to low catalytic activity of Cu toward the C–C bond formation, exhibit a poor electrochemical performance and undergo fast degradation [8, 118, 127, 128].

The changes in electronic structures of supported catalysts, induced by the formation of surface alloys, were measured and analyzed in light of the chemical activities and catalytic performance in accordance with the *d*-band model [129]. One particular conclusion was that the antibonding adsorbate–Ni states for Sn/Ni catalysts are populated to a higher degree than the antibonding states for monometallic Ni, decreasing the strength of the interaction between adsorbates (O, C, OH, CO, CH_x) and Ni sites on the Sn/Ni substrate. The catalytic behavior of Cu and bimetallic CuNi composites with CeO_2-based oxides (20–80 and 40–60 wt.%) for direct oxidation of dry methane at temperatures up to 1173 K was analyzed by temperature-programmed reduction and oxidation and X-ray photoelec-
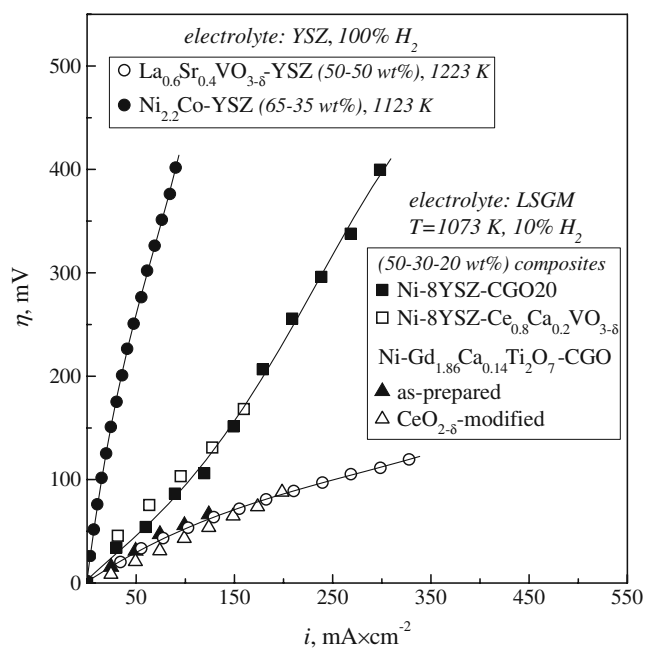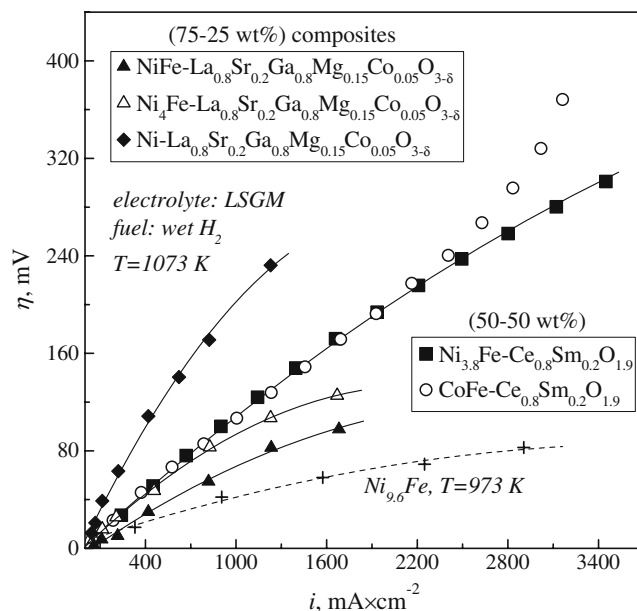

Fig. 10 Anodic overpotentials of (Ni,Fe)–LSGM [124], (Ni,Fe)–CSO [67], and (Co,Fe)–CSO [68] cermet electrodes at 1073 K, compared to a $Ni_{9.6}Fe$ alloy-containing anode at 973 K [65]. The latter three anodes were deposited onto $Ce_{0.8}Sm_{0.2}O_{2-\delta}$ (CSO20) interlayer [65, 67, 68]. The current collectors were made of Pt mesh [67, 68] and Au mesh [68]. H_2 humidified under ambient conditions (~3% H_2O) was used in all cases

tron spectroscopy (XPS) [130]; the catalytic activity appears to depend not only on the presence of nickel but also on the nature of substituents in ceria (e.g., Gd or Tb).

Despite some drawbacks associated, in particular, with oxidation under high current densities, systematic attempts are made to introduce metallic Co and Fe in the cermets [65–69, 123, 124, 131, 132]. For example, composite anodes containing YSZ and bimetallic $Ni_{1-x}Co_x$ and $Ni_{1-x}Cu_x$ were tested in H_2, CH_4, and H_2S–CH_4 gas mixtures [123]. Copper additions were shown to increase metal particle size and to lower SOFC performance, while the use of cobalt has an opposite effect. In both cases, the performance tends to quickly degrade in dry CH_4 due to carbon deposition and anode delamination from YSZ solid electrolyte [123]. On the other hand, $Ni_{2.22}Co$–YSZ (70 wt.% oxide) cermets demonstrated a higher activity in 10% H_2S–CH_4 than in H_2 due to the formation of a sulfidated alloy (Ni–Co–S). Figure 10 and Table 3 present selected results illustrating the performance of Ni–Fe alloys proposed for the anode layers [65], anode supports [66], or cermet components [67, 131]. The maximum power density of an anode-supported single cell, using humidified H_2 fuel and comprising a Ni–Fe alloy produced by reduction of 10 wt.% Fe_2O_3-coated NiO, was reported to decrease after one thermal cycle from 1790 to 1620 mW cm^{-2} at 973 K [116]. A composite $Ni_{8.56}Fe$–MgO–LSGM(10 20) (87.2–2.5–10 wt.%) anode was reported to exhibit a sufficient stability under CH_4 atmosphere at 973 K, a high tolerance against

Fig. 9 Anodic overpotentials of $La_{0.6}Sr_{0.4}VO_{3-\delta}$–YSZ composite [121] and various Ni- [122] and $Ni_{2.2}Co$-containing [123] cermet electrodes with current collectors made of Pt-mesh [122] and Pt–Rh mesh embedded in the electrode layer [123], in H_2-containing atmospheres. Experimental conditions are given above the legends

carbon deposition, and lower overpotentials compared to MgO-free $Ni_{8.56}$Fe–LSGM (90–10 wt.%) cermet, particularly due to an increased basicity and surface activity [131]. Compared to other compositions of the Ni–Fe alloys, the best performance was reported for $Ni_{3.81}$Fe–CSO20 (50–50 wt.%) cermet; under open-circuit conditions, the area-specific polarization resistance was 0.105 Ω cm^2 at 1073 K [67]. The Ni–Fe–$La_{0.8}Sr_{0.2}Ga_{0.8}Mg_{0.15}Co_{0.05}O_{3-\delta}$ composites were also considered for the SOFC anode applications [122], although cobalt is likely to segregate from the lanthanum gallate phase under anodic conditions when partial decomposition of the perovskite solid solution may occur.

The progress achieved in the field of oxide ceramic anodes is also substantially driven by the problems associated with carbon deposition and sulfur poisoning. Due to the oxide phase stability requirements, the choice of parent oxide systems for the ceramic anodes is essentially limited to titanates, chromites, molybdates, and vanadates;

as for the SOFC cathodes, a maximum attention is focused on the perovskite-related compounds. Important examples and typical properties are compared in Tables 3, 4, and 5 and Figs. 9, 11, 12, 13, 14a, 15a, and 16. It should be separately mentioned that pre-reduction of many oxide anode materials, primarily titanates, has often a very positive impact on the final anode performance (e.g., [70]). The electrochemical activity depends therefore on the porous layer prehistory in combination with other performance-determining factors [8]; in many cases, this leads to contradictive results and experimental artifacts. Irrespective of these factors, a relatively good sulfur tolerance in 10–40 ppm H_2S–humidified H_2 was reported for the anode formed of $Sr_{0.88}Y_{0.08}TiO_{3-\delta}$–8YSZ porous backbone infiltrated with ceria and Ru (particle sizes of 30–200 nm) [71]. While copper additions were shown to improve the performance of $La_4Sr_8Ti_{11}Mn_{0.5}Ga_{0.5}O_{37.5-\delta}$–YSZ anodes [138], the total conductivity and catalytic

Table 4 Total electrical conductivity and thermal expansion of selected anode materials under oxidizing and reducing conditions

Composition	Total conductivity			Average TEC			Reference
	T (K)	Atmosphere or p (O_2) (atm)	σ (S/cm)	T (K)	Atmosphere or p (O_2) (atm)	$\alpha \times 10^6$ (K^{-1})	
$La_{0.2}Sr_{0.7}TiO_{3-\delta}$	1173	5% H_2	25^a	300–1273 300–1273	0.21 5% H_2	8.6 9.5	[70]
$La_{0.4}Sr_{0.6}Ti_{0.4}Mn_{0.6}O_{3-\delta}$	1083	0.21 10^{-18}	22.6 1.5	303–1373	0.21	11.9	[72]
$LaCr_{0.5}Mn_{0.5}O_{3-\delta}$	1073	100% H_2	3.7				[133]
$La_{0.8}Sr_{0.2}Cr_{0.5}Mn_{0.5}O_{3-\delta}$	1073	100% H_2	1.3				
$(La_{0.75}Sr_{0.25})_{0.95}Cr_{0.5}Mn_{0.5}O_{3-\delta}$				337–708 793–1229	0.21 0.21	8.9 10.1	[80]
$(La_{0.75}Sr_{0.25})_{0.95}Cr_{0.5}Mn_{0.5}O_{3-\delta}$	1173	0.21 10^{-18}	30.6 2.2	373–923 923–1223 1223–1523 923–1223 923–1223	0.21 0.21 0.21 6×10^{-4} 5×10^{-21}–3×10^{-14}	10.8 12.7 14.1 12.5 11.7	[134]
$La_{0.75}Sr_{0.25}Cr_{0.5}Mn_{0.5}O_{3-\delta}$	1173	10^{-21}	1.5	434–1173	0.21	13.7	[80, 135]
$La_{0.75}Sr_{0.25}Cr_{0.5}Mn_{0.5}O_{3-\delta}$–8YSZ (50–50 wt.%)				564–1173	0.21	12.2	[135]
$Sr_2MgMoO_{6-\delta}$	1073	0.21 5% H_2	3×10^{-3} 0.8				[89]
		5% H_2 10^{-18}	4.3 8.5	382–633 691–1074	0.21 0.21	11.7 12.7	[87, 88]
$Sr_{1.4}La_{0.6}MgMoO_{6-\delta}$	1073	5% H_2	5.0				[89]
$Sr_2MnMoO_{6-\delta}$	1073	10^{-18} 10^{-20}	5.7 7.9				
$CaV_{0.5}Mo_{0.5}O_{4-\delta}$	973– 1173	0.21	10^{-5}– 10^{-4}	473–1173	0.21	10	[136]
$CaV_{0.5}Mo_{0.5}O_{3-\delta}$	1123 1123	10^{-18} 10^{-20}	320 445	473–1173	10% H_2	13	

α is the linear TEC averaged in the given temperature range

^{a} Pre-reduced sample

Table 5 Total polarization resistance at 1073 K and activation energy for the area-specific electrode conductivity of various anode layers under open-circuit conditions in H$_2$-containing atmospheres

Composition	Current collector	Electrolyte	R_η^{1073K} (Ω cm²)	Activation energy		Reference
				T (K)	E_a (kJ/mol)	
Sr$_{0.88}$Y$_{0.08}$TiO$_{3-\delta}$–8YSZ (50–50 wt.%)	Pt mesh + paste	8YSZ	2.6			[71]
Modified with CeO$_{2-\delta}$			1.3			
Ru			0.8			
CeO$_{2-\delta}$+Ru			0.5			
La$_{0.4}$Sr$_{0.6}$Ti$_{0.4}$Mn$_{0.6}$O$_{3-\delta}$–8YSZ (65–35 vol.%)	Au paste	8YSZ	0.5[a]	1003–1129		[72]
Sr$_{0.94}$Ti$_{0.9}$Nb$_{0.1}$O$_{3-\delta}$–8YSZ (50–50 wt.%)	Pt paste	8YSZ	16.3			[137]
LaCr$_{0.5}$Mn$_{0.5}$O$_{3-\delta}$	Pt mesh	YSZ	3.3			[133]
La$_{0.8}$Sr$_{0.2}$Cr$_{0.5}$Mn$_{0.5}$O$_{3-\delta}$	Pt mesh	YSZ	8.6			
(La$_{0.75}$Sr$_{0.25}$)$_{0.95}$Cr$_{0.5}$Mn$_{0.5}$O$_{3-\delta}$	Pt wire	LSGM(9.8 20)	35.6			[109]
Modified with Ni			5.1			
Ni + CeO$_{2-\delta}$			4.8			
(La$_{0.75}$Sr$_{0.25}$)$_{0.95}$Cr$_{0.5}$Mn$_{0.5}$O$_{3-\delta}$	Pt mesh	LSGM(9.8 20)	2.8	973–1073	66	[109]
Modified with CeO$_{2-\delta}$			1.3	973–1073	87	
La$_{0.75}$Sr$_{0.25}$Cr$_{0.5}$Mn$_{0.5}$O$_{3-\delta}$	Au mesh + paste	LSGM(10 20)	0.16			[77]
La$_{0.75}$Sr$_{0.25}$Cr$_{0.5}$Mn$_{0.5}$O$_{3-\delta}$	Au mesh + paste	8YSZ	0.6			[80]
La$_{0.75}$Sr$_{0.25}$Cr$_{0.5}$Mn$_{0.5}$O$_{3-\delta}$	Pt paste	LSGM(10 20)	0.3	973–1073	45	[13]
La$_{0.75}$Sr$_{0.25}$Cr$_{0.5}$Fe$_{0.5}$O$_{3-\delta}$	Pt paste	LSGM(10 20)	1.6	973–1073	66	[13]
La$_{0.75}$Sr$_{0.25}$Cr$_{0.5}$Al$_{0.5}$O$_{3-\delta}$	Pt paste	LSGM(10 20)	0.4	973–1073	62	[13]
Pr$_{0.7}$Ca$_{0.3}$Cr$_{0.5}$Mn$_{0.5}$O$_{3-\delta}$	Pt paste	8YSZ	32	1073–1223	130	[84]
La$_{0.75}$Sr$_{0.25}$Cr$_{0.5}$Mn$_{0.5}$O$_{3-\delta}$–YSZ (50–50 wt.%)	–	YSZ	1.3			[81]
Modified with Pd			0.9			
La$_{0.75}$Sr$_{0.25}$Cr$_{0.5}$Mn$_{0.5}$O$_{3-\delta}$–YSZ (50–50 wt.%)	Pt ink	8YSZ	7.5[a]	1123–1223	105	[138]
La$_{0.75}$Sr$_{0.25}$Cr$_{0.5}$Mn$_{0.5}$O$_{3-\delta}$–CSO15 (75–25 wt.%)	Pt paste	LSGM(10 20)	0.4	973–1073	62	[13]
Cu–La$_{0.75}$Sr$_{0.25}$Cr$_{0.5}$Mn$_{0.5}$O$_{3-\delta}$–YSZ (10–50–40 wt.%)	Pt ink	8YSZ	4.4	973–1223	110	[138]
LaCr$_{0.5}$Mn$_{0.5}$O$_{3-\delta}$–CGO (50–50 wt.%)	Pt mesh	YSZ	0.21			[133]
La$_{0.8}$Sr$_{0.2}$Cr$_{0.5}$Mn$_{0.5}$O$_{3-\delta}$–CGO (50–50 wt.%)	Pt mesh	YSZ	0.74			
LaSr$_2$Fe$_2$CrO$_{9-\delta}$–CGO10 (50–50 wt.%)	sputtered Au grid	LSGM(10 20)	0.3			[86]
Sr$_2$MgMoO$_{6-\delta}$	Pt paste	LSGM(20 20)	0.9	848–1173	77	[139]
Sr$_2$MgMoO$_{6-\delta}$–LSGM(20 20) (50–50 wt.%)	Pt paste	LSGM(20 20)	0.8			[139]
Sr$_2$MgMoO$_{6-\delta}$–CGO20 (50–50 wt.%)	Pt paste	LSGM(20 20)	0.7			[139]

[a] Extrapolated

activity of pure titanates are, however, quite low, limiting their applicability. For instance, at 1123 K in 97% H$_2$–3% H$_2$O gas mixture, the polarization resistance of porous Sr$_{0.94}$Ti$_{0.9}$Nb$_{0.1}$O$_{3-\delta}$–8YSZ (50–50 wt.%) layer in contact with 8YSZ electrolyte and Pt-paste current collector was 16.3 Ω cm², increasing on further redox cycling [137]. The role of Pt/electrode interface in the latter case was assumed negligible based on the comparison with literature data on Pt electrodes. Notice that effects of metal-containing paste current collectors in the electrochemical measurements can only be neglected when no surface spreading and/or metal penetration to the electrochemical reaction zone may occur; if microstructural alterations during long-term operation are significant, such assumptions require careful validation.

For the La$_{0.4}$Sr$_{0.6}$Ti$_{1-x}$Mn$_x$O$_{3-\delta}$ (x=0–0.6) series, the composition with x=0.6 possesses the highest conductivity ([138] and Table 4). This composition exhibits also a moderate TEC, chemical expansion of 0.5% on redox

cycling, and a substantial electrochemical activity with Au-paste current collector under humidified H_2, though the performance in methane becomes much worse (Table 3). A similar combination of properties is known for another perovskite family, $La_{1-x}Sr_xCr_{1-y}Mn_yO_{3-\delta}$ ($x=0–0.3$; $y\leq 0.5$), which shows a relatively good electrode performance in combination with metal current collectors under reducing conditions (Figs. 11, 12, 14, and 15; Table 5), a sufficient dimensional stability and sulfur tolerance [74–84, 109, 133–135, 140–144]. With respect to titanate-based compositions, the main disadvantages of $(La,Sr)(Cr,Mn)O_{3-\delta}$ relate to chromium oxide volatilization at elevated temperatures and phase separation under ambient conditions when Cr^{6+} species may be formed, as typical for the perovskite-type chromites [90]. On the other hand, many titanates tend to hydration in the IT range. The cermets containing $La_{0.75}Sr_{0.25}Cr_{0.5}Mn_{0.5}O_{3-\delta}$ (LSCM) and copper were found to exhibit lower polarization resistances than $Cu–CeO_2$ in 5% H_2 and to have a better adhesion to YSZ [128]. Since additions of Pd to the dense LSCM film led only to a small decrease of the anodic polarization resistance in H_2-containing atmospheres, the oxygen ionic conduction was suggested as an electrochemical reaction rate-determining

factor [143]. The ionic transport in LSCM is indeed low, although the oxygen vacancy concentration and ionic conductivity both increase under reducing conditions [109]. Consequently, CeO_2- and ZrO_2-based additives and interlayers decrease the electrode polarization [76, 79–82, 109, 133, 134, 138, 140, 141, 143]. An optimum composition of the LSCM–CGO composite anodes was identified for the component ratio of 33:67 wt.% [140]. For the majority of chromite- and titanate-based anodes, critical limitations are, however, associated with electronic transport and catalytic activity. As an example, the total conductivity of LSCM varies in the range 20–40 S/cm under oxidizing and moderately reducing conditions and decreases down to 1–5 S/cm on reduction [78, 80, 109]. In the case of model cells, the limiting effects of in-plane resistance and, often, electron transfer in the vicinity of the electrochemical reaction zone can be avoided using specific current collectors, including pastes of Pt, Au, or Ag [74, 75, 77, 79, 80, 82, 84, 137, 138]. Analogously, sputtering of even small amounts of Pt over the Cu–LSCM layer improved the anode performance [76]. Any wide use of noble metals in the power generators and other electrochemical devices is impossible due to economic reasons,
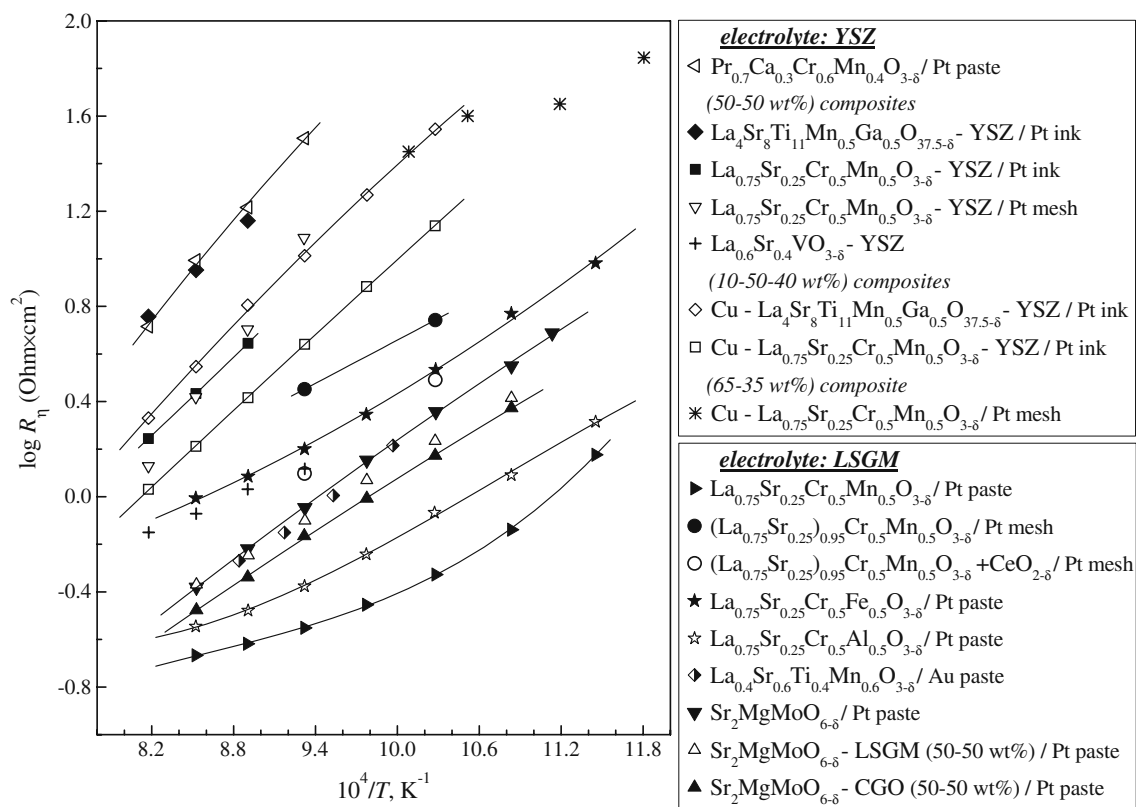

Fig. 11 Comparison on the area-specific polarization resistances of various cermet and oxide anodes in contact with LSGM and YSZ electrolytes [13, 72, 84, 109, 121, 128, 135, 138, 139]. The measurements were performed in diluted H_2 atmospheres, except for $La_{0.6}Sr_{0.4}VO_{3-\delta}$–YSZ measured in 100% H_2 [121] and $La_{0.75}Sr_{0.25}Cr_{0.5}Mn_{0.5}O_{3-\delta}$–YSZ studied in humidified (3% H_2O) CH_4 [135]. The current collectors are specified in the legend after anode composition
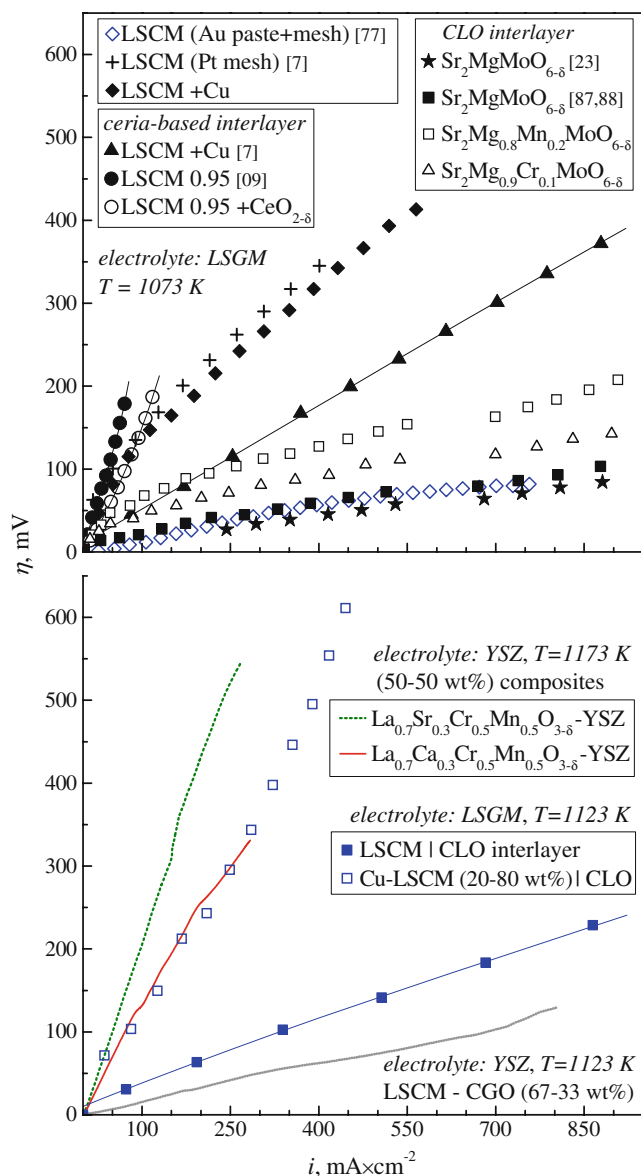
Fig. 12 Polarization curves of $(La,Sr)_{1-x}Cr_{0.5}Mn_{0.5}O_{3-\delta}$ [75–77, 109, 140, 141] and $Sr_2(Mg,M)MoO_{6-\delta}$ [23, 87, 88] based anodes, as-prepared and surface-modified with $CeO_{2-\delta}$ or Cu, in contact with various solid electrolytes with or without ceria-based interlayers. The measurements were performed in hydrogen atmospheres, except for [109] where wet 10% H_2 was used. LSCM, LSCM 0.95, and CLO are $La_{0.75}Sr_{0.25}Cr_{0.5}Mn_{0.5}O_{3-\delta}$, $(La_{0.75}Sr_{0.25})_{0.95}Cr_{0.5}Mn_{0.5}O_{3-\delta}$, and lanthanum-substituted ceria, respectively. The current collector types are indicated in *parentheses* for selected cells. In the case of $Sr_2(Mg,M)MoO_{6-\delta}$ anodes, Pt mesh with a small amount of Pt paste was used as a current collector

Fig. 13 Comparison of the area-specific polarization resistances of various composite anodes applied onto YSZ electrolyte [135, 138, 140] and LSGM with $(Ce,La)O_{2-\delta}$ interlayer [75]. The current collector types are indicated in *parentheses*

catalyst additives in the LSCM-based anodes, especially when operating in hydrocarbon fuels. For example, the additions of 0.5–9 wt.% Pd, Rh, Ni, Fe, or ceria enable to substantially reduce polarization of $(La_{0.75}Sr_{0.25})_{1-z}Cr_{0.5}Mn_{0.5}O_{3-\delta}$ anodes applied onto YSZ and LSGM in H_2- and CH_4-containing atmospheres [79, 82, 109]. Surface deposition of Pd nanoparticles enhances the electrocatalytic activity of porous LSCM-based layers in methane and ethanol, with a minor effect in H_2 [75, 81, 143]. The incorporation of Ni has a higher positive impact on the anode performance with respect to ceria-based phases [79, 109].

If compared to $La_{0.75}Sr_{0.25}Cr_{0.5}Mn_{0.5}O_{3-\delta}$, Sr-free $LaCr_{0.5}Mn_{0.5}O_{3\pm\delta}$ was reported to have better properties, namely a higher thermochemical stability, electronic conductivity, and anode performance in humidified H_2 [133]. For $La_{0.7}AE_{0.3}Cr_{0.5}Mn_{0.5}O_{3-\delta}$, the highest electrochemical activity was claimed for AE = Ca, whereas the barium solubility limit is below 30 mol% [141]. Moderate doping of LSCM with cerium improves the anode performance without an essential influence on the total conductivity. At 1173 K, $La_{0.65}Ce_{0.1}Sr_{0.25}Cr_{0.5}Mn_{0.5}O_{3-\delta}|8YSZ$ anode displayed polarization resistances of 0.2 and 1.6 Ω cm^2 in humidified H_2 and CH_4, respectively [145].

The polarization resistance of $La_{0.8}Sr_{0.2}Cr_{1-x}Ru_xO_{3-\delta}$–CGO10 (50–50 wt.%) composite anodes with x=0–0.25, applied onto LSGM(10 20), was shown to decrease during

whereas the current collectors made of stainless steels or $LaCrO_3$-based ceramics possess considerably higher contact and/or bulk resistances. These factors make it necessary to use LSCM and its analogs in combination with metal additives, such as Ni or Cu [75, 76, 79, 83, 109, 128, 138]. At the same time, the relatively low catalytic activity of LSCM [144] also leads to the necessity of metal or oxide
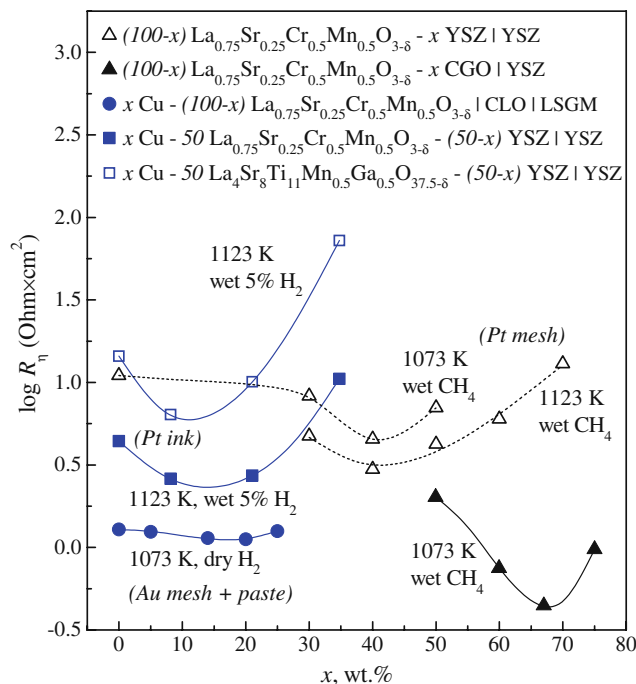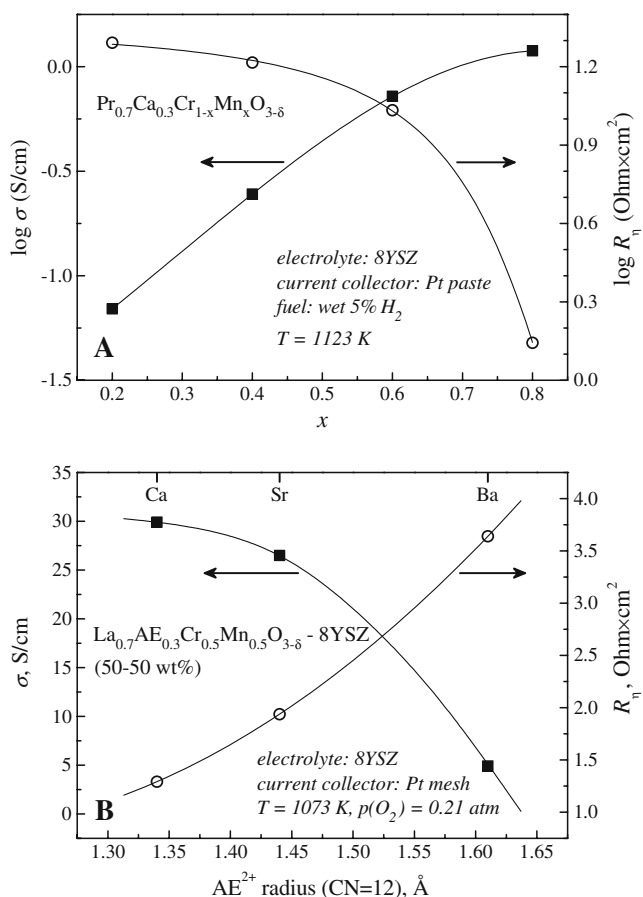
Fig. 14 Total electrical conductivity of dense ceramics and area-specific polarization resistance of porous anodes of $Pr_{0.7}Ca_{0.3}Cr_{1-x}Mn_xO_{3-\delta}$, at 1123 K in humidified 5% H_2–Ar [84] (**a**) and the conductivity of $La_{0.7}AE_{0.3}Cr_{0.5}Mn_{0.5}O_{3-\delta}$ ceramics and polarization resistance of porous $La_{0.7}AE_{0.3}Cr_{0.5}Mn_{0.5}O_{3-\delta}$–YSZ composite cathodes at 1073 K in air [141] (**b**)

Fig. 15 Current-overpotential dependencies of $(La_{0.75}Sr_{0.25})_{0.95}Cr_{0.5}Mn_{0.5}O_3$-based anodes in humidified 10% H_2–90% N_2 atmosphere (**a**) and $(La_{0.75}Sr_{0.25})_{0.95}Cr_{0.5}Mn_{0.5}O_3$-based cathodes in air (**b**), illustrating the effect of current collector configuration [109]. All data correspond to $(La_{0.9}Sr_{0.1})_{0.98}Ga_{0.8}Mg_{0.2}O_{3-\delta}$ solid electrolyte and 1073 K [109]. *Inset* shows the configurations of Pt current collectors

the initial period of SOFC operation before reaching a minimum [73]. The rate of these changes and the electrode performance both increase with increasing x, a result of higher density of Ru surface nanoparticles observed by transmission electron microscopy (TEM). The measured initial surface coverage by Ru nanoparticles was consistent with a model where ruthenium supply to the surface is limited by the Ru bulk out-diffusion, but the coverage saturation requires longer times [73]. Another alternative anode composition, $La_{0.75}Sr_{0.25}Cr_{0.5}Fe_{0.5}O_{3-\delta}$, was reported to be active for CH_4 reforming and total oxidation, depending on the oxygen nonstoichiometry level [146]. At 1123 K, its polarization resistances in contact with 8YSZ electrolyte and Au mesh fixed with a small amount of Au paste were 1.79 and 1.15 Ω cm^2 in wet 5% H_2 and wet 100% H_2, respectively [146]. The R_η values of $La_{0.75}Sr_{0.25}Cr_{0.5}Fe_{0.5}O_{3-\delta}$ anodes, applied onto LSGM and coated with Pt paste, are found higher compared to LSCM [13]. The $LaSr_2Fe_2CrO_{9-\delta}$ perovskite that belongs to the same compositional family appears stable under the

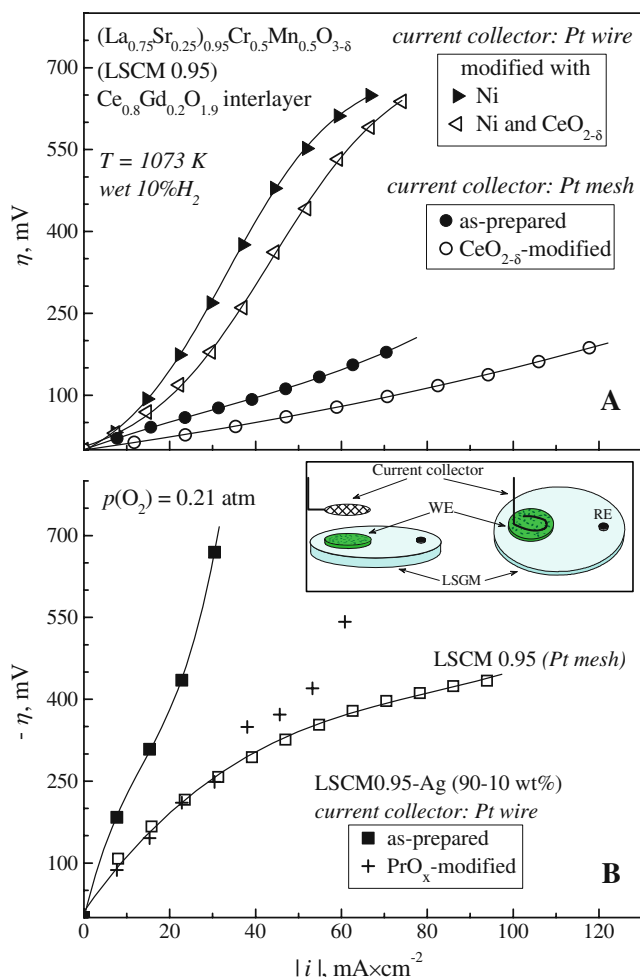SOFC anode conditions up to approximately 1073 K [86]. The performance of $LaSr_2Fe_2CrO_{9-\delta}$–CGO10 (50–50 wt.%) composite anode was slightly better in the cells with LSGM (10 20) electrolyte in comparison to CGO10, under humidified H_2 at 1073 K [86]. $La_{0.8}Sr_{0.2}Sc_{0.2}Mn_{0.8}O_{3-\delta}$, showing higher electrical conductivity and electrocatalytic activity than LSCM under both anodic and cathodic conditions, was also reported to have a sufficient chemical and structural stability due to the backbone effect of Sc^{3+} in the perovskite lattice [85]. In all these cases, however, thorough experimental appraisal of the long-term stability and possible surface-segregation phenomena in highly reducing atmospheres is necessary.

The double $Sr_2Mg_{1-x}M_xMoO_{6-\delta}$ (M = Mn, Cr) perovskites were proposed [87, 88] as the anode candidate materials that meet the requirements for long-term stability
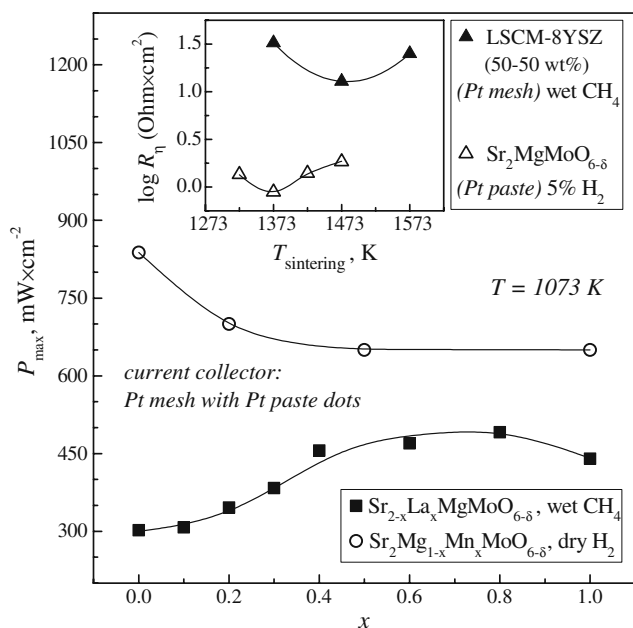
Fig. 16 Maximum power density of model SOFCs with Sr_2MgMoO_6-based anodes [87–89, 139]. The *inset* shows polarization resistances of $La_{0.75}Sr_{0.25}Cr_{0.5}Mn_{0.5}O_{3-\delta}$–YSZ and $Sr_2MgMoO_{6-\delta}$ layers as a function of anode sintering temperature [135, 139]. YSZ [135] and LSGM [87–89, 139] electrolytes were used with $(Ce,La)O_{2-\delta}$ interlayer [87–89]; the current collector type is indicated in *italic*

with a tolerance to sulfur and display a superior electrochemical performance in H_2 and CH_4 (Figs. 11, 12, and 16; Tables 3 and 5). After introducing 5 and 50 ppm H_2S in H_2, approximately 1% and 16% power output degradation was observed for the cells with $Sr_2MgMoO_{6-\delta}$ (SMM) anode and Pt mesh with a small amount of Pt paste as a current collector [87, 88]. The TECs of SMM ceramics vary in the range 11.7–12.7 in air at 380–1070 K (Table 4). The incorporation of La^{3+} into $Sr_{2-x}La_xMgMoO_{6-\delta}$ up to $x=0.8$ improves performance of the cells using hydrocarbon fuels, especially in the presence of water vapor [89]. Above 1073–1273 K, $Sr_2MgMoO_{6-\delta}$ was found to chemically interact with CGO, LSGM, and YSZ, thus making it necessary to introduce buffer layers between the anode and solid electrolyte [89, 139]. Also, reduction above 1173 K results in decomposition of $Sr_2MgMoO_{6-\delta}$ into a mixture of $n=2$ Ruddlesden–Popper phase with a significantly higher Mo/Mg cation ratio, MgO, and Mo; the reduced material was intergrown with the perovskite matrix [147]. XPS and XRD analyses of $Sr_2MgMoO_{6-\delta}$ powders annealed in air and diluted CH_4 atmospheres show that the surface is mainly formed by $SrMoO_4$ scheelite and metal carbonates [139]. Another Mo-containing perovskite, $CaV_{0.5}Mo_{0.5}O_{3-\delta}$, exhibits total conductivity over 520 S cm^{-1} under reducing conditions (10% H_2–90% N_2) at 300–1170 K and was thus proposed for SOFC anodes, though heating in air above 773 K leads to transition of the orthorhombic perovskite into the tetragonal scheelite phase

[136]. This transformation is reversible on further reduction. The TECs of both oxidized and reduced phases are rather similar, 10 and 13×10^{-6} K^{-1}, respectively (Table 4). In the $La_{1-x}Sr_xVO_{3-\delta}$ ($x=0.2$–0.5) series, the perovskite phases also exist under reducing conditions only [121]. These vanadates were found chemically compatible with YSZ, at least up to 1573 K [121]. At 1173 K, $La_{0.6}Sr_{0.4}VO_{3-\delta}$–YSZ (50–50 wt.%) composite anodes showed the polarization resistances of 0.85 and 1.38 Ω cm^2 and overpotentials of 130 and 200 mV at current densities of 200 mA/cm^2 in pure H_2 and wet CH_4, respectively (Fig. 9).

The recent literature data briefly considered in this section indicate that, in fact, there is no exact boundary between the cermet and oxide ceramic anode materials. For most oxide compositions, an introduction of metallic component(s) is still necessary, either as additives in the electrode bulk or as additional layers applied onto the surface of anode ceramic matrix in order to provide adequate current collection and to improve catalytic activity. Moreover, as for the cermet electrodes, most oxide anodes known up to now exhibit a reasonable performance only in combination with solid-electrolyte additives or buffer layers, preferably made of doped ceria. The high-conductivity perovskite vanadates and molybdates (e.g., [121, 136, 148]) are unstable in oxidizing environments and may partially decompose when the anodic current density is high; serious drawbacks may also originate from the volatilization and surface diffusion phenomena, as for the Mo- and V-containing cathodes. Experimental assessment of these materials should include time dependencies of overpotentials and/or power density in combination with complementary techniques such as XPS and TEM.

Alternative cell concepts: single-chamber, micro-, and symmetrical SOFCs

A comprehensive overview on the developments of single-chamber solid oxide fuel cells (SC-SOFCs) can be found in [149, 150]. In this concept, a mixture of fuel and oxidant is supplied to the anode and cathode, which are placed in one gas chamber and are catalytically active for the oxidation and reduction processes, respectively. Key advantages of this approach are associated with easier fabrication and miniaturization compared to the conventional SOFC configurations. However, while the electrolyte membrane quality becomes less important and porous membranes may even be beneficial for SC-SOFCs [151], there appear stringent requirements to the reaction selectivities provided by the electrode materials and to safety of using mixed gases in one chamber. The existing electrode materials provide rather poor cell efficiency and low fuel utilization,

typically <10% [149, 150, 152]. Nevertheless, most reports available in the literature are focused on attempts to adapt conventional SOFC electrode materials to the SC design (Table 6). Notice also that, apart from the microstructural effects discussed below, the performance of SC-SOFCs depends strongly on the gas molar ratio and flow rate (see Fig. 17, Table 6, and references therein). In addition, the catalytic oxidation reactions may result in substantial heating of the electrodes, temperature variations along the cell, and deviations from the initial fuel–air composition [149, 150, 153, 160, 161]. For instance, due to the temperature shift, the Ni–YSZ|8YSZ|La$_{0.8}$Sr$_{0.2}$MnO$_{3\pm\delta}$–YSZ cells exhibit a better performance when small cathodes are located at the inlet, at the CH$_4$/O$_2$ ratio equal to 1:1 [153]. The Ru–CeO$_{2-\delta}$|Ni–CSO|CSO15 (20 μm)|BSCF–CSO cells with Ag-paste and Ag–BSCF current collectors show P_{max} values of 247 mW/cm^2 at C$_3$H$_8$/O$_2$=4:9 when the temperature is maintained at 853 K without external heating [121].

The SC-SOFC cathodes are not only supposed to be active for oxygen reduction but should also be inert for any reaction with fuels. The major material-related trends remain, in general, similar to those for the conventional SOFC cathodes exposed to air [149, 150]. The catalytic activity of layered La$_{0.8}$Sr$_{0.2}$MnO$_{3\pm\delta}$–8YSZ/La$_{0.8}$Sr$_{0.2}$MnO$_{3\pm\delta}$ cathodes sintered at 1373 K increases on heating and decreases when higher sintering temperatures are used [162]. Above 973 K,

the conversion of oxygen species may exceed 30%. However, the half-cells achieve a better performance at 873 K than at 973 K since the catalytic combustion processes become more complex [162]. Despite the problems originating from excessive sintering, interaction with solid electrolyte, and a significant activity for fuel oxidation, Sm$_{0.5}$Sr$_{0.5}$CoO$_{3-\delta}$ cathodes possess a lower resistance and enable higher power outputs than La$_{0.6}$Sr$_{0.4}$CoO$_{3-\delta}$, LaNi$_{0.6}$Fe$_{0.4}$O$_{3-\delta}$, or lanthanum strontium manganite (LSM) in methane–air gas mixtures [163]. Highest performance of the CSO-based cells with R$_{0.7}$Sr$_{0.3}$Fe$_{0.8}$Co$_{0.2}$O$_{3-\delta}$ (R = La, Pr, Gd) cathodes in CH$_4$–air was achieved for R = Pr [152]. At the same time, LSFC exhibits, again, a considerable activity toward electrochemical oxidation of CH$_4$ [164]. BSCF cathodes were reported to have an exceptionally high activity for electrochemical reduction of oxygen and a sufficiently low activity for methane oxidation [165]. The power density generated by the anode-supported Ni–CSO (60–40 wt.%)|CSO15 (20 μm)|BSCF–CSO (70–30 wt.%) cell with Ag current collectors was as high as 760 mW/cm^2 at the nominal furnace temperature of 923 K (cell temperature ~1060 K) when methane, oxygen, and helium flow rates were 87, 80, and 320 ml/min, respectively [165].

The SC-SOFC anodes should be catalytically active and selective for only partial oxidation of fuel and electrochemical oxidation of the produced synthesis gas, a mixture of

Table 6 Selected examples of the maximum power density in various planar SC-SOFCs operating in hydrocarbon–air gas mixtures, reported in 2008–2009

Cathode/current collector	Electrolyte/ thickness	Anode/current collector	CH$_4$/O$_2$ ratio	T (K)[b]	P_{max} (mW cm^{-2})	Reference
Electrolyte-supported cells						
La$_{0.8}$Sr$_{0.2}$MnO$_{3\pm\delta}$–8YSZ (50–50 wt.%)|LSM/Au mesh	8YSZ/0.5 mm	Ni–8YSZ (45 wt.% NiO)|Ni/Au mesh	1:1	973	114	[153]
La$_{0.8}$Sr$_{0.2}$MnO$_{3\pm\delta}$/Au mesh	8YSZ/0.4 mm	Ni–CSO20/Ni mesh	4:5[a]	973	12	[154]
La$_{0.7}$Sr$_{0.3}$Fe$_{0.8}$Co$_{0.2}$O$_{3-\delta}$/Ag paint	CSO17/0.3 mm	Ni–CSO17 (60 wt.% NiO)/Pt paint	2:1	873	49	[152]
Pr$_{0.7}$Sr$_{0.3}$Fe$_{0.8}$Co$_{0.2}$O$_{3-\delta}$/Ag			2:1	873	65	
Gd$_{0.7}$Sr$_{0.3}$Fe$_{0.8}$Co$_{0.2}$O$_{3-\delta}$/Ag			2:1	873	46	
AgO–La$_{0.5}$Sr$_{0.5}$CoO$_{3-\delta}$–CGO20 (10–80–10 wt.%)/the same ink	CGO20-2 wt.% Co/ 0.2 mm	Ni–CGO20 (90–10 wt.%)/the same ink	9:10	1013	280	[155]
Sm$_{0.5}$Sr$_{0.5}$CoO$_{3-\delta}$/porous Au film	CSO17/0.4 mm	Ni–Pd–CSO17 (63 wt.% NiO, 7 wt.% PdO)/porous Pt film	2:1	873	97	[156]
(La$_{0.8}$Sr$_{0.2}$)$_{0.98}$MnO$_{3\pm\delta}$-8YSZ (70–30 wt.%), width 93 μm/Au mesh + paste	8YSZ/0.2 mm, gap size 0.25 mm	Ni–8YSZ (55 wt.% NiO, width 93 μm)/Au mesh + paste	2:1	973	10.5[c]	[157]
Anode-supported cells						
La$_{0.7}$Sr$_{0.3}$MnO$_{3-\delta}$ impregnated with CSO20/Ag paste	8YSZ/8 μm	Ni–8YSZ (50 wt.% NiO)/Ag paste	3:2	1123	416	[158]
Ba$_{0.5}$Sr$_{0.5}$Co$_{0.8}$Fe$_{0.2}$O$_{3-\delta}$-CSO20 (70–30 wt.%)/Ag paste	CSO20/20–30 μm	Ni–CSO20/Ag paste	1:1	873	570	[159]

[a] ΣHC(CH$_4$+C$_2$H$_6$+C$_3$H$_8$+C$_4$H$_{10}$, 1000 ppm each):O$_2$, Ar balance

[b] The furnace temperature is given. The real cell temperature is usually higher due to exothermic partial oxidation of the fuel (see text)

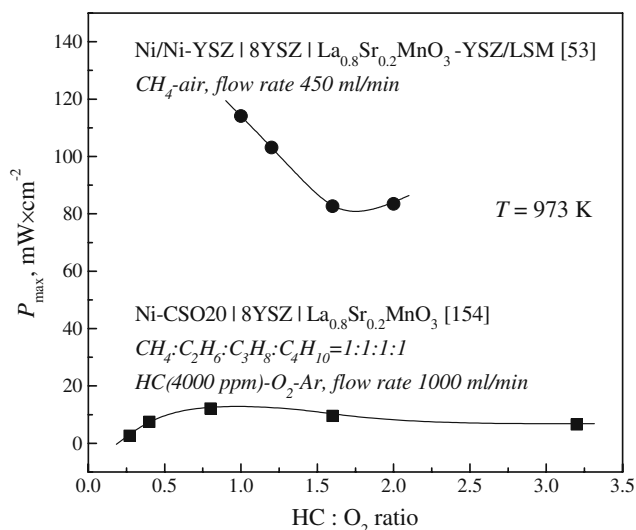[c] Cell with one pair of coplanar electrodes

Fig. 17 Maximum power density of the electrolyte-supported planar single-chamber cells at 973 K as a function of hydrocarbon to oxygen ratio [153, 154]. In all cases, the total gas flow rate was kept constant. Au meshes [153] and Ni and Au meshes [154] were used as current collectors

CO and H_2. The optimum theoretical situation, when the direct electrochemical total oxidation of hydrocarbons occurs at the SC-SOFC anode, was never achieved in practice to a detectable extent. Although carbon deposition is suppressed in fuel–air mixtures, the use of Ni-containing composites may still be problematic due to redox instability of the anode layers and a tendency to form nickel oxide and even volatile hydroxide; these processes decrease the anode conductivity and catalytic activity and cause microstructural degradation [150, 166]. At temperatures higher than 823 K, the $Ni–Ce_{0.9}Zr_{0.1}O_{2−\delta}$ catalysts can promote methane conversion up to 90%, with H_2 and CO as the main products and negligible carbon formation. Additions of Ru catalyst into the Ni–CSO anode improve the cell performance under C_4H_{10}–air at 473–573 K due to favoring hydrogen formation; the use of Pd has an opposite effect [161]. Nevertheless, the incorporation of Pd in the Ni-containing composites has often a positive impact on the anode performance and Ni reducibility ([150, 167] and references cited). Analogously, Ni–Pd–CSO composites were proposed as the anodes for IT SC-SOFC operating under CH_4–air mixtures [156]. The power densities in the cells with CSO electrolyte and $Sm_{0.5}Sr_{0.5}CoO_{3−\delta}$ cathode were found comparable to those of conventional SOFCs comprising similar materials, though porous Pt and Au films were employed as anode and cathode current collectors [156]. Notice that the use of metal grids resulted in a lower performance [156]. Reduced NiO–$(La_{0.75}Sr_{0.25})_{0.9}Cr_{0.5}Mn_{0.5}O_{3−\delta}$ anode layers were tested in [168]. The Ni–CSO20 anodes appear substantially active in CH_4, C_2H_6, C_3H_8, and C_4H_{10} containing atmospheres

[154]. Pre-reduction of the anode before cathode deposition was reported to be more effective than in situ reduction in methane–air gas mixtures [159].

The choice of solid-electrolyte composition for the SC-SOFCs is usually limited to zirconia- and ceria-based materials, although LSGM, $BaLaIn_2O_{5.5}$, $BaCe_{0.8}Y_{0.2}O_{3−\delta}$, $SrCe_{0.95}Yb_{0.05}O_{3−\delta}$, and $CaZr_{0.9}In_{0.1}O_{3−\delta}$ were also tested in the electrolyte-supported cells [163, 168–171]. The performance of model SC-SOFCs based on YSZ, CSO, and LSGM electrolytes compared in [163, 172] was found maximum for LSGM at 873–1073 K and for CSO at 623–723 K, with a Ni–CSO anode and $Sm_{0.5}Sr_{0.5}CoO_{3−\delta}$ cathode. If considering the electrolyte membrane microstructure, one interesting approach is based on the use of porous solid electrolyte, allowing the reaction gases to pass consecutively through the cathode, electrolyte, and anode [173]. The possibility to fabricate a cell stack based on this design has recently been demonstrated [150, 151].

Due to complex catalytic and mass transfer phenomena, the importance of composition, microstructure, and geometry of SC-SOFCs current collectors becomes even greater than for the dual-chamber cells. Quite often, Ag current collectors are used both for the single model cells and for SC-SOFC stacks [151, 158–160, 165, 174]. In order to assess the Ag current collector stability, micro-tubular Ni–YSZ|YSZ|LSM cells with Ag-paste and current-collecting wires for both electrodes were prepared and tested in CH_4–air at 1023 K and an operating voltage of 0.5 V [175]. The results reveal a progressively increasing porosity in the Ag wires with time, leading finally to rupture, due to the formation of silver oxide as well as volatilization and partial melting. Such degradation processes may also be contributed by the cell overheating, as predicted by 2-D axisymmetric numerical modeling [176]. On the other hand, use of small silver additives in the cathode layers is advantageous [155], as for the dual-chamber arrangement. Pt possesses a substantial catalytic activity in the methane–air mixtures, whereas Au is considered essentially inert but interacts with Ni to form eutectic above 1073 K [150]. Integrated Pt-mesh current collectors were embedded into the electrode layers of the Ni–CGO20|CGO10|$Sm_{0.5}Sr_{0.5}CoO_{3−\delta}$ cells, which showed a high open-circuit voltage (OCV) and a power density of 468 mW/cm^2 at 873 K in CH_4–air [177]. In the case of microelectrodes, providing an appropriate current collection is associated with serious challenges [150, 178].

The micro-SOFC (μ-SOFC) concept implies not only the small overall size and higher energy density but also wide use of the microfabrication technologies including those employed in microelectronics [177]. Downscaling of the SC-SOFCs with coplanar electrodes located at the same side of solid-electrolyte membrane is considered feasible

and relatively easy. The efficiency and fuel utilization in this case are, however, lower than for the symmetric cells [150]. The Ni–8YSZ or Ni–CGO10 anodes and $(La_{0.8}Sr_{0.2})_{0.98}MnO_{3\pm\delta}$–8YSZ or $(La_{0.6}Sr_{0.4})_{0.995}Fe_{0.8}Co_{0.2}O_{3-\delta}$ cathodes applied onto 8YSZ substrate via direct-write microfabrication were evaluated for single-chamber micro-SOFCs with coplanar interdigitated (comb-like) electrode configuration [179]. At 973 K in CH_4–air mixture, the best cell performance was obtained for Ni–YSZ and LSM–YSZ electrode pair, regardless of the chemical interaction between the cathode and anode during sintering. The issues related to preferable shapes, to the geometries and electrochemical properties of electrodes, and to the electrolyte thickness are analyzed in [180]. One should separately note that the performance of the cells with coplanar microelectrodes is significantly dependent of the electrode width having both lower and upper limits [157]. Below the lower limit, neither a stable difference in the oxygen chemical potentials nor OCV can be established; exceeding the higher limit leads to an excessively high resistance. For an interelectrode gap of 250 μm, an optimum electrode width was suggested to lie between 550 and 850 μm [157].

The feasibility of using micro-hotplates, a technology platform initially developed in the field of sensors, was demonstrated for the example of $La_{0.6}Sr_{0.4}Co_{0.2}Fe_{0.8}O_{3-\delta}$ thin-film cathodes deposited by spray pyrolysis [181]. Post-deposition annealing steps in an external furnace and use of integrated heater of the micro-hotplate showed that, despite bending, these micro-hotplates are suitable for a maximum operation temperature of 1073 K and long-term operation at 973 K. Thin-film μ-SOFCs were fabricated with Pt anode and $La_{0.6}Sr_{0.4}Co_{0.8}Fe_{0.2}O_{3-\delta}$ cathode using sputtering, lithography, and etching [182]. An alternative dual-chamber cell design with 20-μm-thick solid electrolyte sintered onto the ring of the same material was proposed [183, 184]; at 873 K in wet H_2, the cells with reduced NiO–CGO20 (40–60 wt.%) anode, $Sm_{0.5}Sr_{0.5}CoO_{3-\delta}$ cathode, and Pt-paste current collectors show P_{max} values of 270 and 290 mW/cm² when using CGO20 and LSGM(10 20) electrolytes, respectively. Another configuration for the coplanar cell was fabricated by applying the Ni–8YSZ and $La_{0.7}Sr_{0.3}MnO_{3-\delta}$ electrodes, impregnated with CSO20, in two parallel grooves on YSZ substrate in order to extend a conductive channel of the ionic transport and to form a gas separator between the electrodes, thus providing lower ohmic resistance and higher OCV [174]. The functional layers of nanocrystalline $La_{0.6}Sr_{0.4}Co_{0.8}Fe_{0.2}O_{3-\delta}$ and doped zirconia with thicknesses of 50–300 nm were formed using photolithography, radiofrequency sputtering, lift-off process, and photon-assisted synthesis for potential use in μ-SOFCs [185–187].

The fuel utilization is improved in the micro-tubular (MT) SC-SOFCs, where gas intermixing between the electrodes is avoided and the gases pass a longer distance over the electrode surface. The 2-D distributed finite element model of a MT hollow-fiber SOFCs was used in combination with TPB lengths measured by focused ion beam-SEM technique to predict the effects of anode microstructure on the distribution of current density and anode activation polarization [188]. As for the planar cells, substantially high thermal gradients were revealed theoretically and experimentally along the micro-tubes, which may even cause damages of the cell components at the gas inlet where the temperature rise is higher [176, 189]. The anode-supported, mixed-reactant MT-SOFC with YSZ electrolyte, Ni–YSZ anode, LSM cathode, and silver ink applied to enhance electrical conductivity of both electrodes and catalytic activity of the cathode was prepared and tested [190]; at 1023 K, the OCV of 1.05 V and P_{max}=122 mW/cm² were achieved at CH_4/air ratio of 1:4.76. However, the performance degradation rate was as high as 0.05% per 24 h, and current density fluctuations due to redox cycles over the nickel surface were observed [190]. The preparation conditions were adjusted to obtain dense thin-film $CGO10/Zr_{0.89}Sc_{0.1}Ce_{0.01}O_{2-\delta}$ electrolyte double layers by dip-coating in aqueous suspensions on a porous micro-tubular $Nd_{1.95}NiO_{4+\delta}$ cathode substrate, prepared by cold-isostatic pressing and sintering [191]. The mechanical strength critical for the MT-SOFCs was studied by the example of anode-supported cells consisting of Ni–CGO20 anode, CGO20 electrolyte, and $La_{0.8}Sr_{0.2}Co_{0.6}Fe_{0.4}O_{3-\delta}$–CGO20 cathode, fabricated via extrusion and co-firing [192].

With very rare exceptions, the electrochemical properties of individual electrodes (e.g., polarization resistances and overpotentials) are not assessed in the reports on SC- and micro-SOFCs due to the obvious experimental and methodological problems associated with location and fabrication of the reference electrodes, use of non-equilibrium gas mixtures and porous electrolyte membranes, and limitations to the cell geometry and operation conditions. Instead, the measurements of cell voltage and power output are commonly employed in combination with the outlet gas mixture analysis, giving some information on the electrode selectivities. The electrochemical activity of $(La_{0.8}Sr_{0.2})_{0.98}MnO_{3\pm\delta}$–YSZ composite cathodes for the oxygen reduction reaction in air, evaluated by the standard three-electrode method, was compared for the planar and Ni–YSZ anode-supported closed MT arrangements, with YSZ electrolyte [193]. While the impedance spectra display some differences, the total polarization resistances and overpotential values appear similar. Increasing the MT cell sintering temperature from 1373 to 1423 K was found to improve the cathode performance [193]. Anode-supported

hollow-fiber SOFC with 12-μm-thick 8YSZ electrolyte, Ni–YSZ anode, $(La_{0.8}Sr_{0.2})_{0.95}MnO_{3\pm\delta}$–YSZ cathode, and Ag wires/paste current collectors, fabricated by the phase inversion and vacuum assisted coating techniques, was reported to provide a maximum power density of 377 mW/cm^2 at 1073 K using humidified H$_2$ as a fuel and air as an oxidant [194]. The MT-SOFC with $(La_{0.8}Sr_{0.2})_{0.97}MnO_{3\pm\delta}$–CGO (70–30 wt.%) cathode supports fabricated by extrusion, CGO10/10SSZ bilayer electrolyte, reduced NiO–CGO (50–50 wt.%) anode, and Ag current collectors shows a power density of 352 mW/cm^2 at 1023 K, with humidified H$_2$ and O$_2$ [195]. A honeycomb design suitable for compact SOFC modules with high volumetric power densities due to a large electrode-surface area was proposed in [196]. The cathode-supported SOFC prepared via extrusion of an LSM honeycomb monolith and a slurry-injection method for channel surface coating of the electrolyte/anode bi-layers exhibits power densities of approximately 1200 mW/cm^3 at 873 K with flowing humidified H$_2$ fuel and O$_2$ oxidant. Various concepts of micro-SOFCs are reviewed in [178, 197, 198].

Finally, despite the lower electronic conductivity and poorer electrochemical activity compared to other cathode materials under oxidizing conditions (cf. Tables 1, 2, 4, and 7), the perovskite-type solid solutions derived by Mn doping into chromite and titanate matrixes stable in a wide $p(O_2)$ range attract a growing interest for potential use in the so-called symmetrical SOFCs where the cathode and anode are made of the same or similar compositions [13, 84, 85, 109, 110, 141]. The advantages of this "symmetrical" concept include (a) reducing the number of steps for the SOFC fabrication, (b) lower costs, and (c) a possibility to reverse the configuration. The latter regime may be important, in particular, for removing carbon and sulfur deposited at the anode surface. The cathodic overpotentials of porous $R_{1-x}AE_xCr_{1-y}Mn_yO_{3-\delta}$ electrodes in air are, however, relatively high, in correlation with their transport properties (Figs. 8, 14b, and 15b). In order to illustrate the limiting effects of electronic conductivity, Fig. 15 compares the anodic and cathodic polarization curves of LSCM-based electrodes, observed in the cells with two configurations of Pt current collector shown in the inset [109]. The overall overpotentials are substantially higher when Pt wire is used, although the maximum distance between any point of LSCM-based electrode and Pt was approximately 1.5 mm [109]. This confirms an increasing role of the in-plane resistance and current-constriction effects when the electronic conductivity of the electrode material is lower than 50 S/cm [7, 8]. For $Pr_2Ni_{0.8}Cu_{0.2}O_{4+\delta}$ cathode having the total conductivity of 168 S/cm at 1073 K [27], these limitations can be neglected (Table 8). Analogously, the electrochemical activity of $La_{0.7}AE_{0.3}Cr_{0.5}Mn_{0.5}O_{3-\delta}$ (AE = Ca, Sr, Ba) cathodes decreases in the sequence Ca > Sr > Ba,

in correlation with their electrical conductivity in air [141] (Fig. 14b). The performance of $Pr_{0.7}Ca_{0.3}Cr_{1-y}Mn_yO_{3-\delta}$ (y= 0.2–0.8), where increasing manganese concentration leads to a higher conductivity and to lower anode and cathode polarization resistances [84], is also insufficient for use without highly conducting additives or extra layers. At 1223 K, the symmetrical SOFC with 0.37-mm-thick 8YSZ electrolyte, $Pr_{0.7}Ca_{0.3}Cr_{0.6}Mn_{0.4}O_{3-\delta}$ electrodes, and current collectors formed by deposition of Pt ink shows power densities of 250 and 160 mW cm^{-2} in humidified H$_2$ and CH$_4$ fuels, respectively (Table 3). Since perovskite-type $La_{0.8}Sr_{0.2}Mn_{0.8}Sc_{0.2}O_{3-\delta}$ has a higher conductivity than LSCM both in oxidizing and reducing atmospheres, the P_{max} values of a symmetric electrolyte-supported cell with $La_{0.8}Sr_{0.2}Mn_{0.8}Sc_{0.2}O_{3-\delta}$ layers and 0.3-mm-thick scandia-stabilized zirconia electrolyte were 310 and 130 mW cm^{-2} at 1173 K in H$_2$ and CH$_4$, correspondingly [85]. These examples illustrate one important problem arising on the use of symmetrical SOFC electrodes in the reversible configurations. Namely, the moderate level of electronic transport in known oxide materials stable under both oxidizing and reducing conditions, such as LSCM, makes it necessary to incorporate current-collecting layers and/or electrode components. For the conventional configuration, this problem can be solved applying pastes and/or meshes of transition metals (e.g., Ni or its alloys) in the anode compartment and pastes of highly conductive oxides (e.g., doped cobaltite perovskites or RP-type nickelates) for the cathode. These components become all unstable in the reverse regime when the redox stability, high conductivity, and low contract resistance may only be provided by noble metals.

Hydrocarbon-fueled and direct-carbon SOFCs

The direct electrochemical oxidation of dry hydrocarbons on the surface of oxide mixed conductors is quite slow [199], but may often be promoted at high current densities [83]. As a rule, operation of the cells fueled by methane and higher hydrocarbons occurs via the anodic electrochemical oxidation of gaseous products formed on either reforming (external or internal) or cracking (on metallic catalysts or in the gas phase) [7, 199]. As nickel is catalytically active toward both these processes, large amounts of steam or CO$_2$ are necessary to avoid the carbon deposition onto Ni-containing cermets; alternatively, components with high catalytic activity to the carbon oxidation, such as ceria-based compounds, should be incorporated in the anode layers. At the same time, the endothermic nature of catalytic reforming may cause local thermomechanical stresses and cell failure [199, 200]. Information on the microscopic mechanisms of hydrocarbon oxidation in

Table 7 Total polarization resistance at 1073 K and apparent activation energy for the area-specific electrode conductivity of $(La_{0.75}Sr_{0.25})_{1-x}$ $Cr_{0.5}M_{0.5}O_{3-\delta}$-based electrodes in contact with LSGM, under open-circuit conditions in air

Composition	Current collector	R_η^{1073K} (Ω cm^2)	T (K)	E_a (kJ/mol)	Reference
$(La_{0.75}Sr_{0.25})_{0.95}Cr_{0.5}Mn_{0.5}O_{3-\delta}$	Pt wire	24.1	873–1073	27	[109]
Ag–$(La_{0.75}Sr_{0.25})_{0.95}Cr_{0.5}Mn_{0.5}O_{3-\delta}$ (10–90 wt.%)	Pt wire	22.3			
Ag–$(La_{0.75}Sr_{0.25})_{0.95}Cr_{0.5}Mn_{0.5}O_{3-\delta}$, PrO$_x$-infiltrated	Pt wire	8.2			
$(La_{0.75}Sr_{0.25})_{0.95}Cr_{0.5}Mn_{0.5}O_{3-\delta}$	Pt mesh	13.5			
$La_{0.75}Sr_{0.25}Cr_{0.5}Mn_{0.5}O_{3-\delta}$	Pt paste	17.6	873–923	47	[13]
			923–1073	137	
$La_{0.75}Sr_{0.25}Cr_{0.5}Fe_{0.5}O_{3-\delta}$	Pt paste	34.8	873–973	14	[13]
			973–1073	98	
$La_{0.75}Sr_{0.25}Cr_{0.5}Al_{0.5}O_{3-\delta}$	Pt paste	1.4	873–923	118	[13]
			923–1073	185	

SOFCs is still very scarce due to serious experimental limitations, namely the presence of several parallel processes that are current and overpotential dependent, involve solid surfaces and electrode–electrolyte interface, and occur with gas volume and temperature changes affecting multicomponent diffusion in the porous media. The relevant experiments require also to focus a special attention on the gas tightness of solid-electrolyte membranes and sealing, since air leakages into the fuel chamber suppress carbon formation [199, 200]. The use of oxygen-permeable sealants, such as silver [201], and electrolytes with significant electronic transport [115] is often inappropriate for this purpose.

Whatever the microscopic mechanisms, a variety of approaches are being tested to overcome problems arising due to carbon deposition in the hydrocarbon-fueled SOFCs (e.g., [202–207] and references cited). For example, porous disks of CGO-impregnated FeCr were appraised as a gas diffusion layer of methane-fueled cells [203]. At 1073 K and ambient pressure, the major reaction in this layer was CO_2-reforming of CH_4 and subsequent oxidation of carbon monoxide at the Ni–YSZ anode; rather surprisingly, H_2 conversion was reported negligible [203]. An internal reforming layer of $Cu_{1.3}Mn_{1.7}O_4$ spinel, where highly dispersed nano-Cu particles are formed after in situ reduction by CH_4, was shown to improve stability of Ni–CSO anode-supported cells, with P_{max}=311 mW/cm^2 at 973 K [204]. The Ni–YSZ|Pt|8YSZ|$La_{0.8}Sr_{0.2}MnO_{3\pm\delta}$ cell, with 1-mm-thick electrolyte and 0.1 wt.% Ir-impregnated CeO_2 catalyst layer coated over the anode, was operated both under the gradual internal reforming conditions and using pure dry methane at 1173 K, yielding a current density of about 0.1 A/cm^2 at 0.6 V during 120 h [205]. In spite of a minor deterioration in the performance, no carbon deposition was observed [205]. Analogously, the incorporation of Rh-alumina catalyst and porous zirconia-based

barrier layers made it possible to improve the performance stability of CH_4-fueled Ni–YSZ (50–50 wt.%) anodes [200, 201].

The methane conversion over LSFC–YSZ anodes was found to occur via CH_4 cracking and electrochemical oxidation of hydrogen and carbon [164]. In the case of Cu-$La_{0.75}Sr_{0.25}Cr_{0.5}Mn_{0.5}O_{3-\delta}$-8YSZ layers exposed to CH_4 and C_4H_{10}, hydrocarbon cracking dominates under the conditions close to open circuit [141]. The prevailing electrode reaction mechanism changes to the total electrochemical oxidation on increasing current density when oxygen content in LSCM increases, as suggested by the measurements of the cell OCV, carbon deposition rates, and catalytic behavior of LSCM [141]. A relatively poor cell performance (Table 3) was assigned to the ohmic losses at the anode. Various anodes including Ni–SSZ and Ni–CGO cermets, CGO, and $La_{0.85}Sr_{0.15}MnO_{3-\delta}$–CGO composite were employed for rechargeable cells where the solid carbon is supplied by thermal decomposition of hydrocarbon fuel [67, 207]. In principle, these cells could also be classified as direct-carbon (DC) SOFCs as their operation is based on the electrochemical oxidation of carbon deposits.

Table 8 Comparison of cathodic overpotentials for porous Ag–$(La_{0.75}Sr_{0.25})_{0.95}Cr_{0.5}Mn_{0.5}O_{3-\delta}$ (10–90 wt.%) and $Pr_2Ni_{0.8}Cu_{0.2}O_{4+\delta}$ electrodes in contact with LSGM(9.8 20) and different current collector configurations and total conductivity of dense oxide ceramics in air, at 1073 K [27, 109]

Composition	σ (S/cm)	η (mV) at $i=$ −30 mA cm^{-2}	
		Pt wire	Pt mesh
$(La_{0.75}Sr_{0.25})_{0.95}Cr_{0.5}Mn_{0.5}O_{3-\delta}$	25.0	−669	−254
$Pr_2Ni_{0.8}Cu_{0.2}O_{4+\delta}$	167.9	−11	−10

The DCSOFC is one type of solid oxide fuel cells utilizing solid carbon, which is directly fed into the anode compartment. During the last years, a variety of DCSOFCs with different solid carbonaceous fuels were tested [208–213]. The choice of anode material and cell configuration is determined by methods for delivering solid fuel to the electrochemical reaction zone [208, 211]; Table 9 lists several examples. In simplest arrangements, the powdered fuel may be applied or pressed onto the solid-electrolyte surface, thus serving also as an anode [209, 210]. Amorphous carbon materials provide usually higher power densities as compared to crystalline graphite [210]. The cells based on fluidized-bed (FB) configuration were suggested [211–214] to exploit different gasification approaches; their comparison can be found in [212]. Note that carbon gasified into carbon monoxide by re-circulating carbon dioxide, without steam, can be used for the SOFC arrangement coupled to a Boudouard-type FB dry gasifier [211, 214]. Another concept [215] is based on a merged SOFC and molten carbonate fuel cell technology with the anodes comprising molten alkaline metal carbonates and/or oxides (e.g., eutectic mixtures of K_2CO_3, Li_2CO_3, and/or Na_2CO_3), which facilitate oxygen transport from the solid oxide electrolyte to the surface of solid fuel [208, 215–220]. The slurries of carbon particles provide electronic transport in the molten carbonate-containing anodes, thus acting as both an anode component and a fuel. The direct oxidation and Boudouard conversion both contribute to the overall reaction [219]. Implementation of this approach requires, however, periodic replacements of the cell components due to their degradation [216, 217]. In particular, YSZ electrolyte was found stable in molten Na/

K carbonate mixture at 1123 K at least for 24 h, but lithium zirconate is formed in Li/K carbonate at 973 K; ceria seems quite stable in both cases [217]. A carbon–air semi-fuel cell/battery concept was demonstrated [217–220] employing Ni mesh or porous Ni–YSZ anode layers, YSZ electrolyte, and Pt-paste or porous LSM–YSZ cathodes; the co-sintered tape-casted cells were immersed in K_2CO_3+ Li_2CO_3 (38–62 mol.%) melt with a dispersed super S carbon or pyrolyzed MDF. Irrespective of the model cell configuration, the most significant technological challenges are related to pre-treatment and continuous feeding of the solid carbon fuels, cell stacking, and scaling up of DCSOFCs. The stability problems of solid-electrolyte membranes, including their mechanical and thermal shock behavior, optimum thickness, and effects of minor physical leakages, also need to be carefully addressed. From the methodological point of view, serious efforts are necessary to identify the anodic reaction mechanisms in DCSOFCs. In addition to the problems associated with elaboration of appropriate reference electrodes and local variations of the oxygen chemical potential, these mechanisms may be substantially altered in the presence of moisture, sulfur, and chloride impurities characteristic of raw coal.

Lastly, the liquid tin anode SOFCs with Sn/SnO_2 melt as an anode, YSZ electrolyte, and lanthanum strontium manganite (LSM) cathode were found suitable for a continuous operation using JP-8 fuel, with prospects to utilize coal and other fuels [221–223]. In the case of JP-8 that contains ~1400 ppm sulfur, the cell stack achieved a power density of 120 mW/cm^2 and fuel utilization higher than 40% [222]. In addition, such an anode stores energy, enabling the cell to deliver power if the fuel flow is

Table 9 Performance of various DC-SOFCs with planar or tubular zirconia-based electrolyte

Cathode	Electrolyte/thickness	Anode	Fuel	T (K)	P_{max} (mW cm^{-2})	Reference
$La_{0.84}Sr_{0.16}MnO_3$	$(ZrO_2)_{0.90}(HfO_2)_{0.02}(Y_2O_3)_{0.08}$/ 0.12 mm	Carbon black	Carbon black	1275	50	[209]
				1073	10	
Pt or Pt–YSZ	PSZ[a]/1.3 mm	Pt or Pt–YSZ	Synthetic carbon bed fluidized by He	1173	1	[213]
LSM	YSZ/0.2 mm	Ni–ceria		1173	22	[213]
LSM	YSZ/10 μm	Ni–YSZ	Activated carbon bed	1178	220	[212]
Perovskite	YSZ/8–10 μm	Ni–YSZ	Coal bed fluidized by CO_2	1123	450	[214]
LSM	YSZ/0.3–0.8 mm	Fuel (~40 vol.%) in molten mixture of K_2CO_3+Li_2CO_3+Na_2CO_3	Raw coal	1223	110	[215]
			Biomass	1223	70	
				1173	40	
			Tar	1173	80	

[a] Partially stabilized zirconia

interrupted. At the same time, anodic polarization may induce problems due to the formation of SnO_2, which has a poor solubility in liquid tin and partially blocks the solid-electrolyte surface [221, 224, 225]. When molten Bi was used, the anode polarization resistance remains low, <0.25 Ω cm^2 at 973 K, until essentially all bismuth metal is oxidized to Bi_2O_3 [225]. The volatilization of bismuth oxide and its corrosion activity at elevated temperatures may, however, limit application of the Bi-based anodes.

Electrodes for high-temperature fuel cells with proton-conducting electrolytes: selected remarks

Use of high-temperature (870–1070 K) proton conductors as alternative solid-electrolyte materials in the fuel cells is expected to provide important improvements, primarily a simplified water management as steam forms at the cathode side [226]. Enhanced sulfur and coking tolerance was reported for $BaCe_{0.7}Zr_{0.1}Y_{0.2-x}Yb_xO_{3-\delta}$ exhibiting a fast diffusion of both protons and oxygen-ion vacancies [227]. Among the main issues limiting practical applications of the high-temperature proton conductors (PCs), one may note a non-negligible electronic conduction in certain ranges of the oxygen and hydrogen chemical potentials and a limited chemical stability in CO_2- and SO_x-containing atmospheres. The latter problem is typical for the compositions with high barium content, despite their high protonic conductivity. In this respect, the recently discovered proton conductors based on rare-earth orthoniobates $RNbO_4$ [226, 228, 229] may be advantageous compared to the well-known cerate and zirconate perovskites. Since the electrode performance depends on the transport mechanisms in solid electrolytes and other their properties [7], the electrochemical behavior of similar electrodes may differ in the cases when oxygen anion and proton conductors are used. Systematic studies are hence necessary to examine already known electrode materials in contact with the proton-conducting electrolytes, at least for the most promising compositions and microstructural engineering approaches. The main methodological aspects of the electrode polarization analysis in the PC-based cells are similar to those well-established for the oxygen anion conductors. Experimental limitations may appear under the external conditions when electron transference numbers are significant, as typical for many proton-conducting phases in oxidizing and highly reducing atmospheres with low partial pressures of water vapor or hydrogen (e.g., [230, 231]); due to short-circuiting of the working and reference electrodes, the electronic transport may lead to underestimated overpotentials and should be taken into account. The presence of two migrating ionic species, protons and oxygen anions, requires a precise control of both $p(H_2O)$ and $p(O_2)$ or p

(H_2) at the electrodes since the polarization depends, in general, on the fluxes of each ionic charge carrier. On the other hand, advanced experimental techniques for the analysis of microscopic mechanisms become available due to the possibility to use D_2 and D_2O in combination with various spectroscopic methods. Selected data on the performance of oxide, metal, and cermet electrodes in contact with proton-conducting solid electrolytes are presented in Fig. 18 and Table 10.

The double perovskite $Ba_2Ca_{0.79}Nb_{0.66}Ta_{0.55}O_{6-\delta}$ proton conductor was reported to be stable against chemical reaction with $La_{0.8}Sr_{0.2}MnO_{3-\delta}$ and $Sm_{0.5}Sr_{0.5}CoO_{3-\delta}$ at 1073–1273 K [232]. The polarization resistance of these and Pt electrodes in wet gas mixtures is lower than that in atmospheric air, with minimum values for LSM. The overall performance is, however, much worse than that for
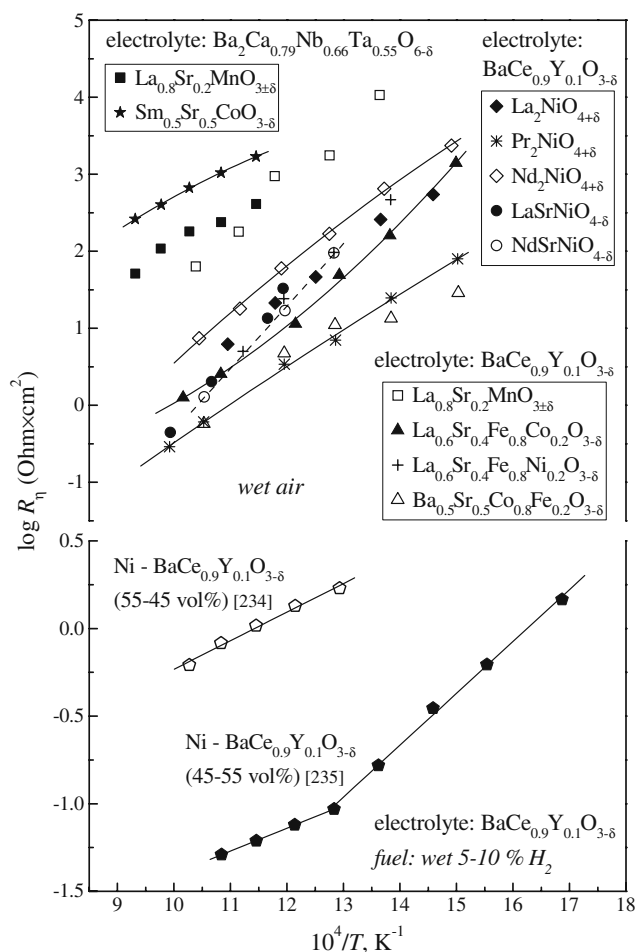

Fig. 18 Temperature dependencies of the area-specific polarization resistances of various oxide cathodes [232, 233] and cermet anodes [234, 235] in the electrochemical cells with proton-conducting solid electrolytes and Pt-mesh [233, 235] or Pt-disk [234] current collectors. The gases supplied to the electrodes were humidified under ambient conditions (~3% H_2O), except for the data on $Ba_2Ca_{0.79}Nb_{0.66}Ta_{0.55}O_{6-\delta}$-based cells [232] where ambient air was used

Table 10 Total polarization resistance at 973 K and activation energy for the area-specific electrode conductivity of metal and oxide electrodes in contact with proton-conducting solid electrolytes under open-circuit conditions

Electrode composition	Current collector	Electrolyte	Atmosphere	R_η^{973K} (Ω cm^2)	Activation energy		Reference
					T (K)	E_a (kJ/mol)	
Pt	Pt wire	$Ba_2Ca_{0.79}Nb_{0.66}Ta_{0.55}O_{6-\delta}$	Air	78	873–1073	84	[232]
$La_{0.8}Sr_{0.2}MnO_{3\pm\delta}$	Pt wire	$Ba_2Ca_{0.79}Nb_{0.66}Ta_{0.55}O_{6-\delta}$	Air	186.5	873–1073	120	
$La_{0.8}Sr_{0.2}MnO_{3\pm\delta}$	Pt mesh	$BaCe_{0.9}Y_{0.1}O_{3-\delta}$	Wet air	57[a]	730–960	127	[233]
$Sm_{0.5}Sr_{0.5}CoO_{3-\delta}$	Pt wire	$Ba_2Ca_{0.79}Nb_{0.66}Ta_{0.55}O_{6-\delta}$	Air	682.5	873–1073	126	[232]
$La_{0.6}Sr_{0.4}Fe_{0.8}Co_{0.2}O_{3-\delta}$	Pt mesh	$BaCe_{0.9}Y_{0.1}O_{3-\delta}$	Wet air	1[a]	670–980	120	[233]
$La_{0.6}Sr_{0.4}Fe_{0.8}Ni_{0.2}O_{3-\delta}$	Pt mesh	$BaCe_{0.9}Y_{0.1}O_{3-\delta}$	Wet air	1[a]	720–890	142	
$Ba_{0.5}Sr_{0.5}Co_{0.8}Fe_{0.2}O_{3-\delta}$	Pt mesh	$BaCe_{0.9}Y_{0.1}O_{3-\delta}$	Wet air	0.8[a]	670–950	67	
$La_2NiO_{4+\delta}$	Pt mesh	$BaCe_{0.9}Y_{0.1}O_{3-\delta}$	Wet air	3[a]	690–910	104	
$Pr_2NiO_{4+\delta}$	Pt mesh	$BaCe_{0.9}Y_{0.1}O_{3-\delta}$	Wet air	0.4[a]	670–1010	91	
$Nd_2NiO_{4+\delta}$	Pt mesh	$BaCe_{0.9}Y_{0.1}O_{3-\delta}$	Wet air	6[a]	670–960	109	
$LaSrNiO_{4-\delta}$	Pt mesh	$BaCe_{0.9}Y_{0.1}O_{3-\delta}$	Wet air	0.9[a]	840–1010	174	
$NdSrNiO_{4-\delta}$	Pt mesh	$BaCe_{0.9}Y_{0.1}O_{3-\delta}$	Wet air	0.8[a]	780–950	155	
Pt		$SrCe_{0.95}Yb_{0.05}O_{3-\delta}$	Wet H$_2$	0.4–1[a]	520–1080	58–84	[236]
Ni–$BaCe_{0.9}Y_{0.1}O_{3-\delta}$ (55–45 vol.%)	Pt disk	$BaCe_{0.9}Y_{0.1}O_{3-\delta}$	Wet 5% H$_2$	0.6	773–973	31	[234]
Ni–$BaCe_{0.9}Y_{0.1}O_{3-\delta}$ (45–55 vol.%)	Pt mesh	$BaCe_{0.9}Y_{0.1}O_{3-\delta}$	Wet 10% H$_2$	0.04[a]	590–780 780–923	57 25	[235]

[a] Extrapolated or interpolated

the cells with oxygen ionic conductors; this fact was explained by a limiting role of protonic transport at the electrolyte and electrode interfaces and/or water effusion through micropores [232]. Cobalt diffusion from the electrodes into the electrolyte surface layers may have a positive impact on both electronic and protonic conductivities [237]. However, 10 mol% Co doping of $BaCe_{0.5}Zr_{0.4}(Y,Yb)_{0.1-x}Co_xO_{3-\delta}$ lowers its chemical stability in H_2O/H_2 and CO_2. In the series comprising $La_{0.8}Sr_{0.2}MnO_{3\pm\delta}$, $La_{0.6}Sr_{0.4}Fe_{0.8}Co_{0.2}O_{3-\delta}$, $La_{0.6}Sr_{0.4}Fe_{0.8}Ni_{0.2}O_{3-\delta}$, $Ba_{0.5}Sr_{0.5}Co_{0.8}Fe_{0.2}O_{3-\delta}$, $R_2NiO_{4+\delta}$ (R = La, Nd, Pr), and $RSrNiO_{4-\delta}$ (R = La, Nd) cathodes in contact with $BaCe_{0.9}Y_{0.1}O_{3-\delta}$ (BCY10) electrolyte in 3% H_2O–air atmosphere, BSCF and $Pr_2NiO_{4+\delta}$ were identified as most promising, regardless of the lower total conductivity compared to $La_{0.6}Sr_{0.4}Fe_{0.8}M_{0.2}O_{3-\delta}$ and $LaSrNiO_{4-\delta}$

Table 11 Performance of various single planar PC-SOFCs fueled by wet H$_2$

Cathode	Electrolyte/thickness (μm)	Anode	T (K)	P_{max} (mW cm^{-2})	Reference
$Pr_2NiO_{4+\delta}$	$BaCe_{0.9}Y_{0.1}O_{3-\delta}$/40	Ni–$BaCe_{0.9}Y_{0.1}O_{3-\delta}$ (45 vol.% Ni)	923	130[a]	[235]
$La_{0.6}Sr_{0.4}Fe_{0.8}Co_{0.2}O_{3-\delta}$– $BaCe_{0.7}Zr_{0.1}(Y,Yb)_{0.2}O_{3-\delta}$	$BaCe_{0.7}Zr_{0.1}(Y,Yb)_{0.2}O_{3-\delta}$/10	Ni–$BaCe_{0.7}Zr_{0.1}(Y,Yb)_{0.2}O_{3-\delta}$ (65 wt.% NiO)	923	660	[227]
$PrBa_{0.5}Sr_{0.5}Co_2O_{5+\delta}$	$BaCe_{0.7}Zr_{0.1}Y_{0.2}O_{3-\delta}$/20	Ni–$BaCe_{0.7}Zr_{0.1}Y_{0.2}O_{3-\delta}$ (60 wt.% NiO)	973	520	[239]
$SmBa_{0.5}Sr_{0.5}Co_2O_{5+\delta}$	$BaCe_{0.5}Zr_{0.3}Y_{0.16}Zn_{0.04}O_{3-\delta}$/17	Ni–$BaCe_{0.5}Zr_{0.3}Y_{0.16}Zn_{0.04}O_{3-\delta}$ (60 wt.% NiO)	973	306	[240]
$Ba_{0.5}Sr_{0.5}Co_{0.8}Fe_{0.2}O_{3-\delta}$	$Ba_2(In_{0.8}Ti_{0.2})_2O_{5.2-x}(OH)_{2x}$/35	Ni–$Ba_2(In_{0.8}Ti_{0.2})_2O_{5.2}$ (50 wt.% Ni)	773	22[b]	[242]

[a] Pt-mesh current collectors
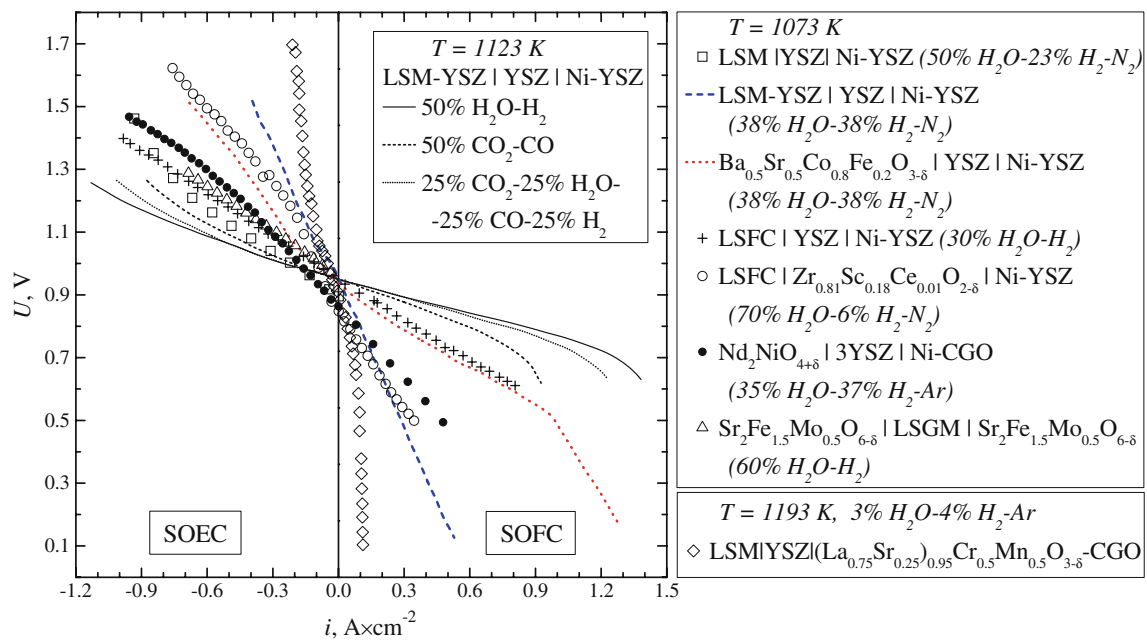
[b] Au-mesh current collectors

Fig. 19 Current–voltage curves of various Ni–YSZ cermet electrode-supported [248, 252, 253], electrolyte-supported [250, 251, 258, 261], and a porous ferritic steel-supported [262] SOFCs/SOECs. LSM and LSFC are $La_{0.8}Sr_{0.2}MnO_{3\pm\delta}$ and $La_{0.6}Sr_{0.4}Fe_{0.8}Co_{0.2}O_{3-\delta}$ or unspecified. BSCF is $Ba_{0.5}Sr_{0.5}Co_{0.8}Fe_{0.2}O_{3-\delta}$. The indicated gas mixtures were supplied onto the SOEC cathode/SOFC anode, whereas the oxygen electrodes were operated in air or pure O_2. Pt mesh [248, 250, 251, 262], Pt wires and paste [253], Au paste and mesh [261], and Pt and Au pastes [258] were used as current collectors

Table 12 Comparison of the electrolysis currents at 1.3 V and hydrogen production rates in single SOECs

Anode	Electrolyte/ thickness (μm)	Cathode	Cathode atmosphere	T (K)	i (A cm^{-2})	H$_2$ production (ml cm^{-2} h^{-1})	Reference
LSM	YSZ	Ni–YSZ	70% H$_2$O– 14% H$_2$– N$_2$	1073	1.06		[248]
LSM–YSZ	YSZ/30	Ni–YSZ (60 wt.% NiO)	54% H$_2$O– 23% H$_2$– N$_2$	1123	0.46	100	[253]
BSCF, CGO10 interlayer	YSZ/30	Ni–YSZ (60 wt.% NiO)	54% H$_2$O– 23% H$_2$– N$_2$	1123	0.61	135	
LSFC–CGO20, CGO20 interlayer	$Zr_{0.81}Sc_{18}Ce_{0.01}O_{2-\delta}$/10	Ni–$Zr_{0.81}Sc_{18}Ce_{0.01}O_{2-\delta}$	60% H$_2$O– 4% H$_2$–Ar	923	0.57		[263]
LSFC	$Zr_{0.81}Sc_{18}Ce_{0.01}O_{2-\delta}$/155	Ni–YSZ	70% H$_2$O– 6% H$_2$–Ar	1073	0.35		[250]
				1123	0.68		
LSFC	YSZ/40	Ni–YSZ (50 wt.% NiO)	30% H$_2$O– H$_2$	1073	0.77		[262]
Nd$_2$NiO$_{4+\delta}$	3YSZ/90	Ni–CGO	37% H$_2$O– 35% H$_2$– Ar	1073	0.64		[251]
				1123	0.87		
La$_{0.4}$Ba$_{0.6}$CoO$_{3-\delta}$	LSGM(10 20)/500	Ni–Fe (90–10 wt.%), Ni–CSO20 (10–90 wt.%) interlayer	25% H$_2$O– N$_2$	1073	0.31		[257]
Sr$_2$Fe$_{1.5}$Mo$_{0.5}$O$_{6-\delta}$	LSGM(10 20)	Sr$_2$Fe$_{1.5}$Mo$_{0.5}$O$_{6-\delta}$	60% H$_2$O– H$_2$	1173	0.85	380	[258]
LSM	YSZ/250	$(La_{0.75}Sr_{0.25})_{0.95}Cr_{0.5}Mn_{0.5}O_{3-\delta}$ –CGO	3% H$_2$O– 4% H$_2$–Ar	1193	0.15		[261]

LSM $La_{0.8}Sr_{0.2}MnO_{3\pm\delta}$ or unknown, *LSFC* $La_{0.6}Sr_{0.4}Fe_{0.8}Co_{0.2}O_{3-\delta}$ or unknown

[233]. No chemical interaction between these materials and BCY10 was observed at 923 K in humidified air during 3 weeks [233]. The electrochemical activity of $Sm_{0.5}Sr_{0.5}CoO_{3-\delta}$-$BaCe_{0.8}Sm_{0.2}O_{3-\delta}$, BSCF-$BaCe_{0.8}Sm_{0.2}O_{3-\delta}$, $PrBaCuFeO_{5+\delta}$, $SmBaCuFeO_{5+\delta}$, $SmBaCuCoO_{5+\delta}$, $BaCe_{0.5}Fe_{0.5}O_{3-\delta}$, and $BaCe_{0.5}Bi_{0.5}O_{3-\delta}$ cathodes applied onto $BaCe_{0.8}Sm_{0.2}O_{3-\delta}$ and $BaCe_{0.7}Zr_{0.1}Y_{0.2}O_{3-\delta}$ solid electrolytes was also evaluated ([238] and references cited), although possible influence of Ag-paste current collectors should be additionally examined in the present case.

Apart from the other requirements to the PC-SOFC anode materials, these should exhibit mixed protonic and electronic conductivity [226]. As hydrogen dissolves in metallic Ni, nickel-based cermets are often employed for the anodes. Typical examples include Ni–BCY10 [234, 235] and Ni–Ba$(Ce,Zr)_{0.8}(Y,M)_{0.2}O_{3-\delta}$ (M = Yb, Zn) [227, 239, 240]. The cermet anode made of Ni and nanocrystalline BCY10 was found to possess a relatively low polarization resistance in contact with BCY10 electrolyte under wet 5% H_2, ~1 Ω cm^2 at 873 K (Fig. 18) [234]. Notice, however, that this composition is stable in diluted H_2, while severe degradation occurs after exposure to CO_2 at 973 K. No chemical reaction between $La_{0.995}Ca_{0.005}NbO_{4-\delta}$ and nickel substrate was detected by XPS of in situ reduced samples [241]. The electrode morphology issues are discussed in [236] by the example of Pt layers.

In most cases, the anode-supported PC-SOFC configurations are selected [235, 239–242] as the anodic polarization is usually lower than cathodic, whereas moderate levels of the solid-electrolyte conductivity make it necessary to use thin electrolyte layers. Typical performances of single PC-SOFCs are compared in Table 11. The cells with thin-film $La_{0.995}Sr_{0.005}NbO_{4-\delta}$ electrolyte, cathodes made of $CaTi_{0.9}Fe_{0.1}O_{3-\delta}$, $La_2NiO_{4+\delta}$ and $La_4Ni_3O_{10-\delta}$, and Ni–$La_{0.995}Sr_{0.005}NbO_{4-\delta}$ cermet anodes were produced by a versatile process combining tape casting, spin coating, and screen printing [229]. While formation of La_3NbO_7 and $La(Nb,Ni)O_3$ secondary phases is possible at the $La_2NiO_{4+\delta}$/$La_{0.995}Sr_{0.005}NbO_{4-\delta}$ interface, the $CaTi_{0.9}Fe_{0.1}O_{3-\delta}$ and $La_4Ni_3O_{10-\delta}$–$La_{0.995}Sr_{0.005}NbO_{4-\delta}$ cathodes showed a good adhesion and negligible interfacial reaction with the electrolyte. An interesting hybrid system of two different SOFCs, one being based on the oxygen ionic conductor and another with proton-conducting electrolyte, was proposed in [236]. Due to internal reforming of CH_4, the former cell can produce electrical power and an exhaust gas containing H_2 and CO that can be used for the PC cell operation. The remaining CO reacts further with H_2O via the water gas-shift reaction to produce extra hydrogen in the PC-SOFC, thus reducing carbon deposition and improving the overall system efficiency [243].

High-temperature electrolyzers and electrochemical reactors

As for SOFCs, perovskite-related materials and Ni-based cermets are widely employed for the electrodes of other electrochemical systems, such as solid oxide electrolysis cells (SOECs) [244–247]. Moreover, the high-temperature steam electrolysis (HTSE) for hydrogen production is often performed by reversing the operation regime of SOFCs made of conventional materials, including Ni cermets [248–253]. The overall electrolysis reaction rate was suggested to be limited by nickel oxidation and steam diffusion in the H_2/H_2O electrode, at least at moderate levels of the absolute humidity (<70 vol.%) [248, 254]. As an example, the electrochemical behavior of the cermet electrode composed of NiO–CuO–YSZ–CeO_2 (50–5–40–5 wt.%) impregnated with ceria was studied in contact with YSZ electrode in various atmospheres [255]; increasing steam partial pressure was found to increase hydrogen formation rate and, as a rule, to lower the total electrode polarization. Near the equilibrium potential, gas diffusion limitations of the electrode reaction are indicated by a low-frequency signal in the impedance spectra [255]. Appraising of $LaGaO_3$-based electrolytes for steam electrolysis [256–258] showed, in particular, relatively low cathodic overpotentials of metallic Ni. At 873 K, iron additions in the cathode enable to increase H_2 formation rate, which is the highest at the Ni to Fe weight ratio of 9:1 and reaches 180 μmol cm^{-2} min^{-1} for the electrolyte thickness of 0.2 mm [256]. These tests did not indicate degradation of the lanthanum gallate membranes, which could be expected owing to the reduction of Ga^{3+} cations at electrode–electrolyte interface in highly reducing environments [259]. On the other hand, no degradation was also reported in the symmetrical SOEC with LSGM(10 20) solid electrolyte and perovskite-type $Sr_2Fe_{1.5}Mo_{0.5}O_{6-\delta}$ electrodes [258], although the oxygen chemical potentials under SOEC cathodic conditions are low with respect to the stability limits of perovskite-related ferrite phases [260]. In terms of the cathode stability, the chromite- and titanate-based materials discussed above seem more reliable. For instance, the properties of $(La_{0.75}Sr_{0.25})_{0.95}Cr_{0.5}Mn_{0.5}O_{3-\delta}$ and its composites with YSZ or CGO made it possible to suggest these materials as alternative cathode compositions for YSZ-based SOECs operated under low hydrogen partial pressures [261]. The optimization strategies of the SOEC electrodes are similar to those for SOFCs, briefly discussed above and in the previous parts of this review. Some specific features result from a greater role of concentration polarization in the case of SOEC cathodes, different kinetics of oxygen reduction, and evolution processes on perovskite-related mixed conductors where the relative roles of oxygen diffusivity and ion transfer through the electrolyte/electrode interface tend often to

increase under anodic conditions with respect to the electrode-surface exchange and pronounced microstructural degradation phenomena such as electrode delamination in SOECs.

Porous $La_{0.6}Sr_{0.4}Fe_{0.8}Co_{0.2}O_{3-\delta}$ and $La_{0.8}Sr_{0.2}MnO_{3-\delta}$–YSZ (50–50 vol.%) with optimized microstructures were tested as reversible electrodes for oxygen reduction in the SOFC mode and oxygen evolution in the SOEC regime in the model cells with $Zr_{0.81}Sc_{0.18}Ce_{0.01}O_{2-\delta}$ electrolyte and Ni–8YSZ counter electrodes exposed to 70% H_2O–6% H_2–24% N_2 gas mixture [250]. At 1123 K, the cell with LSFC electrode was reported to be apparently reversible (total polarization resistance of 0.73 Ω cm^2), whereas the activation polarization becomes significant at lower temperatures [250]. In spite of the thermomechanical limitations discussed above, the performance of LSFC and BSCF anodes in the electrolysis cells is generally higher than that of lanthanum-strontium manganites or LSM–YSZ composites [250, 253, 254], as for SOFCs. Several examples are presented in Fig. 19 and Table 12. For comparison, at an applied voltage of 1.4 V, the hydrogen production rate in Ni–YSZ|YSZ|BSCF cell is approximately three times higher than that of Ni–YSZ|YSZ|LSM [254]. BSCF undergoes, however, very fast degradation under the operating conditions [253]; 3 mol.% yttria-stabilized zirconia (3YSZ) electrolyte-supported cell with Ni–CGO and $Nd_2NiO_{4+\delta}$ electrodes was operated reversibly in the SOFC/SOEC modes and showed much higher current densities than those of similar cells with LSM oxygen electrode [251]. The polarization resistances in the latter case were slightly lower for the steam electrolysis processes [251]. An opposite behavior was observed for the cells with LSM, LSFC, and BSCF oxygen electrodes in [250, 253, 254, 262], probably reflecting the relevance of ion diffusion mechanism and dominating ionic charge carriers that contribute to the interfacial exchange processes.

The metal-supported SOECs consisting of a porous steel support, $La_{0.6}Sr_{0.2}Ca_{0.2}CrO_{3-\delta}$ diffusion barrier layer, Ni–YSZ hydrogen electrode, YSZ electrolyte, and LSFC oxygen electrode were tested for the HTSE process during over 2000 h [262]. Long-term testing with a steam content of 43% at 1073 K and a current density of −0.3 A/cm^2 revealed degradation rates of 2.1–3.9% per 1000 h, increasing with time. The polarization resistance tends to increase faster during the electrolysis operation if compared to the fuel cell regime [262]. The time degradation in the SOEC performance was proven to be essentially caused by impurities absorbed at the cathode; cleaning of the inlet gases enables to improve long-term durability [252, 263]. A micro-tubular SOEC consisting of $La_{0.6}Sr_{0.4}Fe_{0.8}Co_{0.2}O_{3-\delta}$–CGO20 air electrode, CGO20 buffer layer, $Zr_{0.81}Sc_{18}Ce_{0.01}O_{2-\delta}$ electrolyte, and supporting Ni–$Zr_{0.81}Sc_{18}Ce_{0.01}O_{2-\delta}$ steam electrode was also produced and tested [264].

The SOECs for CO_2 electrolysis or co-electrolysis of CO_2 and H_2O can be used to recycle carbon dioxide into sustainable hydrocarbon fuels [252, 263]. The mechanisms of electrode reactions and degradation in such cells were studied by transforming the impedance data to the distribution of relaxation times [252]. The degradation of perovskite-type oxygen (positive) electrodes is related to Cr migration from other stack components and to electrode delamination [265]; the latter mechanism was assessed in [266]. The inhibiting role of chromium migration and poisoning is similar to that in SOFCs and makes it necessary to minimize use of Cr-containing materials in the electrochemical cells. This factor might give an argument in favor of titanate-based electrode materials with respect to LSCM; however, numerous other factors such as hydration in wet atmospheres should also be taken into account.

Serious efforts are continuously centered on the experimental assessment and modeling of various SOEC-based systems (e.g., [245–247, 267–269] and references cited). The SOEC performing at elevated pressures necessary for the catalyst operation was proposed to simplify the system [267]. A 16-cm^2 planar Ni–YSZ|YSZ|LSM–YSZ cell where the electrolyte membrane was as thin as 10 μm was tested at 0.4–10 atm [267]. The SOFC performance increased with total pressure by >50%, achieving the power densities of ~955 mW/cm^2 at 1023 K using 80% H_2–20% H_2O as the fuel; the pressure effect on the SOEC performance was found weaker, regardless of a pronounced decrease in the electrode polarization resistances. Another important example refers to the spontaneous electrochemical production of hydrogen and cogeneration of electric power, achieved in the (H_2O, H_2) Pt|YSZ|Pt (C, CO, CO_2) cells with carbon bed loaded onto the anode [269].

The SOFC-based electrochemical reactors can also be used for syngas production via the partial oxidation of methane and other hydrocarbon fuels [201, 203]. As an example, the anode-supported Ni–YSZ (50–50 wt.%)|8YSZ (12 μm)|$La_{0.8}Sr_{0.2}MnO_{3-\delta}$ cells were operated using CH_4 fuel in the regime when oxygen ion fluxes through electrolyte membrane are close to the molar CH_4 flow rates, i.e., the CH_4/O ratio corresponds to the electrochemical partial oxidation [201]. A 88% CH_4 conversion to syngas and a power density of 936 mW/cm^2 were initially achieved. Although the conversion decreases during the first 30–40 h due to Ni nanoparticle sintering and resultant lowering of the anode reforming activity, this can be partly suppressed by the incorporation of Rh/Al_2O_3 catalyst [201]. The SOFC-based devices with catalytically active electrodes are also considered feasible for NO removal from industrial flue gases and power cogeneration [270]. For this goal, the model cells were made of Ni–CGO10 (37.5–62.5 wt.%) anode, YSZ electrolyte, and $La_{0.58}Sr_{0.4}Fe_{0.8}Co_{0.2}O_{3-\delta}$–CGO10 (67–33 wt.%) composite cathodes with small (1.34 wt.%) additions of V_2O_5, used in commercial catalysts for selective catalytic reduction processes, or Cu effective for the direct

electrochemical NO reduction. The NO reduction occurs over the cathode with or without the presence of oxygen; P_{max} is higher for Cu catalyst and increases with O_2 concentration [270]. A proton-conducting cell comprising a thick porous BCY15 anode substrate impregnated with Pt catalyst for dehydrogenation of ethane to ethylene, dense 30-μm-thick BCY15 film and Pt cathode, showed a 90.5% selectivity to ethylene at 36.7% ethane conversion and 216 mW/cm^2 power density at 973 K [271]; the conversion and the reaction selectivity both increase with current density. The possibility to use Ni–CSO20|8YSZ| $La_{0.8}Sr_{0.2}MnO_{3\pm\delta}$ SC-SOFCs with gas mixtures containing parts per million level amounts of CH_4, C_2H_6, C_3H_8, C_4H_{10}, and O_2, as the power generators for exhaust energy recovery, was demonstrated in [154]. Among other applications, one may note catalytic methane sensors [171] based on the SC-SOFC design with high-temperature proton-conducting $SrCe_{0.95}Yb_{0.05}O_{3-\delta}$ or $CaZr_{0.9}In_{0.1}O_{3-\delta}$ and electrodes having different catalytic activities for dry reforming of CH_4.

References

1. Minh NQ, Takahashi T (1995) Science and technology of ceramic fuel cells. Elsevier, Amsterdam
2. Srinivasan S (2006) Fuel cells from fundamentals to applications. Springer, New York
3. Kharton VV (ed) (2009) Solid state electrochemistry I: fundamentals, materials and their applications. Wiley, Weinheim
4. Steele BCH (2001) J Mater Sci 36:1053
5. Menzler NH, Tietz F, Uhlenbruck S, Buchkremer HP, Stöver D (2010) J Mater Sci 45:3109
6. Sun C, Hui R, Roller J (2010) J Solid State Electrochem 14:1125
7. Tsipis EV, Kharton VV (2008) J Solid State Electrochem 12:1039
8. Tsipis EV, Kharton VV (2008) J Solid State Electrochem 12:1367
9. Tarancón A, Burriel M, Santiso J, Skinner SJ, Kilner JA (2010) J Mater Chem 20:3799
10. Gong M, Liu X, Trembly J, Johnson C (2007) J Power Sources 168:289
11. Aguadero A, Pérez-Coll D, de la Calle C, Alonso JA, Escudero MJ, Daza L (2009) J Power Sources 192:132
12. Xia T, Lin N, Zhao H, Huo L, Wang J, Grenier J-C (2009) J Power Sources 192:291
13. Peña-Martínez J, Marrero-López D, Pérez-Coll D, Ruiz-Morales JC, Núñez P (2007) Electrochim Acta 52:2950
14. Kim JH, Cassidy M, Irvine JTS, Bae J (2009) J Electrochem Soc 156:B682
15. Deng ZQ, Smit JP, Niu HJ, Evans G, Li MR, Xu ZL, Claridge JB, Rosseinsky MJ (2009) Chem Mater 21:5154
16. Jin C, Liu J (2009) J All Compd 474:573
17. Tsipis EV, Kharton VV, Frade JR (2006) Solid State Ionics 177:1823
18. Tsipis EV, Kharton VV, Frade JR, Núñez P (2005) J Solid State Electrochem 9:547
19. Kim J-H, Manthiram A (2010) Chem Mater 22:822
20. Kim J-H, Kim YN, Cho SM, Wang H, Manthiram A (2010) Electrochim Acta 55:5312
21. Vert VB, Serra JM, Jordá JL (2010) Electrochem Commun 12:278
22. Nagasawa K, Daviero-Minaud S, Preux N, Rolle A, Roussel P, Nakatsugawa H, Mentré O (2009) Chem Mater 21:4738
23. Hou S, Alonso JA, Goodenough JB (2010) J Power Sources 195:280
24. Duval SBC, Graule T, Holtappels P, Ouweltjes JP, Rietveld G (2009) Fuel Cells 9:911
25. Amow G, Skinner SJ (2006) J Solid State Electrochem 10:538
26. Amow G, Davidson IJ, Skinner SJ (2006) Solid State Ionics 177:1205
27. Kovalevsky AV, Kharton VV, Yaremchenko AA, Pivak YV, Tsipis EV, Yakovlev SO, Markov AA, Naumovich EN, Frade JR (2007) J Electroceram 18:205
28. Yaremchenko AA, Kharton VV, Bannikov DO, Znosak DV, Frade JR, Cherepanov VA (2009) Solid State Ionics 180:878
29. Kharton VV, Tsipis EV, Yaremchenko AA, Frade JR (2004) Solid State Ionics 166:327
30. Tsipis EV, Kharton VV, Frade JR (2007) Electrochim Acta 52:4428
31. Aguadero A, Alonso JA, Escudero MJ, Daza L (2008) Solid State Ionics 179:393
32. Kammer K (2009) Ionics 15:325
33. Vidal K, Rodríguez-Martínez LM, Ortega-San-Martin L, Martínez-Amesti A, Nó ML, Rojo T, Laresgoiti A, Arriortua MI (2009) J Power Sources 192:175
34. Huang J, Jiang X, Li X, Liu A (2009) J Electroceram 23:67
35. Sakitou Y, Hirano A, Hanai K, Matsumura T, Imanishi N, Takeda Y (2007) ECS Trans 7:1305
36. Huang X, Li T, Lu Z, Wang Z, Wei B, Su W (2010) J Phys Chem Solids 71:230
37. Zhang G, Dong X, Liu Z, Zhou W, Shao Z, Jin W (2010) J Power Sources 195:3386
38. Tarancón A, Skinner SJ, Chater RJ, Hernández-Ramírez F, Kilner JA (2007) J Mater Chem 17:3175
39. Vert VB, Serra JM (2009) Fuel Cells 9:663
40. Baek S-W, Bae J, Yoo Y-S (2009) J Power Sources 193:431
41. Torres-Garibay C, Kovar D, Manthiram A (2009) J Power Sources 187:480
42. Wang F, Zhou Q, He T, Li G, Ding H (2010) J Power Sources 195:3772
43. Shao ZP, Haile SM (2004) Nature 431:170
44. Chen C-H, Chang C-L, Hwang B-H (2009) Mater Chem Phys 115:478
45. Zuev AYu, Vylkov AI, Petrov AN, Tsvetkov DS (2008) Solid State Ionics 179:1876
46. Yan A, Liu B, Dong Y, Tian Z, Wang D, Cheng M (2008) Appl Catal B 80:24
47. Arnold M, Gesing TM, Martynczuk J, Feldhoff A (2008) Chem Mater 20:5851
48. Švarcová S, Wiik K, Tolchard J, Bouwmeester HJM, Grande T (2008) Solid State Ionics 178:1787
49. Ovenstone J, Jung J-I, White JS, Edwards DD, Misture ST (2008) J Solid State Chem 181:576
50. Chen D, Ran R, Zhang K, Wang J, Shao Z (2009) J Power Sources 188:96
51. Petrov AN, Cherepanov VA, Zuev AYu (2006) J Solid State Electrochem 10:517
52. Al Daroukh M, Vashook VV, Ullmann H, Tietz F, Arual Raj I (2003) Solid State Ionics 158:141
53. Karppinen M, Yamauchi H, Fjellvåg H, Motohashi T (2008) Eur Patent 1900706
54. Chmaissem O, Zheng H, Huq A, Stephens PW, Mitchell JF (2008) J Solid State Chem 181:664
55. Aksenova TV, Gavrilova LY, Yaremchenko AA, Cherepanov VA, Kharton VV (2010) Mater Res Bull 45:1288

56. Kournoutis VC, Tietz F, Bebelis S (2009) Fuel Cells 9:852
57. Lee S, Song HS, Hyun SH, Kim J, Moon J (2009) J Power Sources 187:74
58. Hansen KK, Hansen KV, Mogensen M (2010) J Solid State Electrochem 14:2107
59. Shaula AL, Kharton VV, Marques FMB, Kovalevsky AV, Viskup AP, Naumovich EN (2006) J Solid State Electrochem 10:28
60. Mori T, Buchanan R, Ou DR, Ye F, Kobayashi T, Kim JD, Zou J, Drennan J (2008) J Solid State Electrochem 12:841
61. Mauvy F, Lalanne C, Bassat J-M, Grenier J-C, Zhao H, Huo L, Stevens P (2006) J Electrochem Soc 153:A1547
62. Kharton VV, Kovalevsky AV, Patrakeev MV, Tsipis EV, Viskup AP, Kolotygin VA, Yaremchenko AA, Shaula AL, Kiselev EA, Waerenborgh JC (2008) Chem Mater 20:6457
63. Vidal K, Rodríguez-Martínez LM, Ortega-San-Martin L, Martínez-Amesti A, Nó ML, Rojo T, Laresgoiti A, Arriortua MI (2009) ECS Trans 25:2427
64. Bidrawn F, Lee S, Vohs JM, Gorte RJ (2008) J Electrochem Soc 155:B660
65. Ju Y-W, Eto H, Inagaki T, Ida S, Ishihara T (2010) J Power Sources 195:6294
66. Park HC, Virkar AV (2009) J Power Sources 186:133
67. Lu XC, Zhu JH (2007) J Power Sources 165:678
68. Lu ZG, Zhu JH, Bi ZH, Lu XC (2008) J Power Sources 180:172
69. Lv H, Yang D, Pan X, Zheng J, Zhang C, Zhou W, Ma J, Hu K (2009) Mater Res Bull 44:1244
70. Savaniu C-D, Irvine JTS (2009) J Mater Chem 19:8119
71. Kurokawa H, Yang L, Jacobson CP, De Jonghe LC, Visco SJ (2007) J Power Sources 164:510
72. Fu QX, Tietz F, Stöver D (2006) J Electrochem Soc 153:D74
73. Kobsiriphat W, Madsen BD, Wang Y, Marks LD, Barnett SA (2009) Solid State Ionics 180:257
74. Tao S, Irvine JTS, Kilner JA (2005) Adv Mater 17:1734
75. Lu XC, Zhu JH (2007) Solid State Ionics 178:1467
76. Wan J, Zhu JH, Goodenough JB (2006) Solid State Ionics 177:1211
77. Peña-Martínez J, Marrero-López D, Ruiz-Morales JC, Savaniu C, Núñez P, Irvine JTS (2006) Chem Mater 18:1001
78. Zha S, Tsang P, Cheng Z, Liu M (2005) J Solid State Chem 178:1844
79. Zhu X, Lü Z, Wei B, Chen K, Liu M, Huang X, Su W (2009) J Power Sources 190:326
80. Tao S, Irvine JTS (2004) J Electrochem Soc 151:A252
81. Jiang SP, Ye Y, He T, Ho SB (2008) J Power Sources 185:179
82. Kim G, Lee S, Shin JY, Corre G, Irvine JTS, Vohs JM, Gorte RJ (2009) Electrochem Solid State Lett 12:B48
83. Bruce MK, van den Bossche M, McIntosh S (2008) J Electrochem Soc 155:B1202
84. El-Himri A, Marrero-López D, Ruiz-Morales JC, Peña-Martínez J, Núñez P (2009) J Power Sources 188:230
85. Zheng Y, Zhang C, Ran R, Cai R, Shao Z, Farrusseng D (2009) Acta Mater 57:1165
86. Haag JM, Madsen BD, Barnett SA, Poeppelmeier KR (2008) Electrochem Solid-State Lett 11:B51
87. Huang Y-H, Dass RI, Xing Z-L, Goodenough JB (2006) Science 312:254
88. Huang Y-H, Dass RI, Denyszyn JC, Goodenough JB (2006) J Electrochem Soc 153:A1266
89. Ji Y, Huang Y-H, Ying J-R, Goodenough JB (2007) Electrochem Commun 9:1881
90. Kharton VV, Yaremchenko AA, Naumovich EN (1999) J Solid State Electrochem 3:303
91. Hjalmarsson P, Søgaard M, Mogensen M (2009) Solid State Ionics 180:1395
92. Tsipis EV, Kiselev EA, Kolotygin VA, Waerenborgh JC, Cherepanov VA, Kharton VV (2008) Solid State Ionics 179:2170
93. Kharton VV, Viskup AP, Naumovich EN, Tikhonovich VN (1999) Mater Res Bull 34:1311
94. Kharton VV, Kovalevsky AV, Tikhonovich VN, Naumovich EN, Viskup AP (1998) Solid State Ionics 110:53
95. Simner SP, Bonnett JF, Canfield NL, Meinhardt KD, Sprenkle VL, Stevenson JW (2002) Electrochem Solid-State Lett 5:A173
96. Vogt UF, Sfeir J, Richter J, Soltmann C, Holtappels P (2008) Pure Appl Chem 80:2543
97. Vogt UF, Holtappels P, Sfeir J, Richter J, Duval S, Wiedenmann D, Züttel A (2009) Fuel Cells 9:899
98. Hansen KK (2010) Mater Res Bull 45:197
99. Pérez-Coll D, Aguadero A, Escudero MJ, Daza L (2009) J Power Sources 192:2
100. Kharton VV, Kovalevsky AV, Avdeev M, Tsipis EV, Patrakeev MV, Yaremchenko AA, Naumovich EN, Frade JR (2007) Chem Mater 19:2027
101. Kharton VV, Tsipis EV, Naumovich EN, Thursfield A, Patrakeev MV, Kolotygin VA, Waerenborgh JC, Metcalfe IS (2008) J Solid State Chem 181:1425
102. Tsipis EV, Naumovich EN, Shaula AL, Patrakeev MV, Waerenborgh JC, Kharton VV (2008) Solid State Ionics 179:57
103. Bannikov DO, Cherepanov VA (2006) J Solid State Chem 179:2721
104. Tsipis EV, Patrakeev MV, Waerenborgh JC, Pivak YV, Markov AA, Gaczyński P, Naumovich EN, Kharton VV (2007) J Solid State Chem 180:1902
105. Nakayama S, Kageyama T, Aono H, Sadaoka Y (1995) J Mater Chem 5:1801
106. Kharton VV, Shaula AL, Patrakeev MV, Waerenborgh JC, Rojas DP, Vyshatko NP, Tsipis EV, Yaremchenko AA, Marques FMB (2004) J Electrochem Soc 151:A1236
107. Shaula AL, Kharton VV, Marques FMB (2006) Solid State Ionics 177:1725
108. Bonhomme C, Beaudet-Savignat S, Chartier T, Geffroy P-M, Sauvet A-L (2009) J Eur Ceram Soc 29:1781
109. Kharton VV, Tsipis EV, Marozau IP, Viskup AP, Frade JR, Irvine JTS (2007) Solid State Ionics 178:101
110. Marrero-López D, Martín-Sedeño MC, Peña-Martínez J, Ruiz-Morales JC, Núñez P, Aranda MAG, Ramos-Barrado JR (2010) J Power Sources 195:2496
111. Bonhomme C, Beaudet-Savignat S, Chartier T, Pirovano C, Vannier RN (2010) Mater Res Bull 45:491
112. Yoshioka H, Mitsui T, Mineshige A, Yazawa T (2010) Solid State Ionics 181:1707
113. Kharton VV, Naumovich EN, Yaremchenko AA, Marques FMB (2001) J Solid State Electrochem 5:160
114. Jaiswal A, Wachsman ED (2009) Ionics 15:1
115. Kharton VV, Marques FMB, Atkinson A (2004) Solid State Ionics 174:135
116. Sun C, Stimming U (2007) J Power Sources 171:247
117. Tietz F, Nikolopoulos P (2009) Fuel Cells 9:867
118. Gorte RJ, Vohs JM (2009) Curr Opin Colloid Interface Sci 14:236
119. Kanjanaboonmalert T, Tzu TW, Sato K (2009) ECS Transact 16:23
120. Oishi N, Yoo Y (2010) Mater Lett 64:876
121. Ge XM, Chan SH (2009) J Electrochem Soc 156:B386
122. Tsipis EV, Kharton VV, Frade JR (2005) J Eur Ceram Soc 25:2623
123. Grgicak CM, Pakulska MM, O'Brien JS, Giorgi JB (2008) J Power Sources 183:26
124. Wang S, Hea Q, Liu M (2009) Electrochim Acta 54:3872
125. Ouweltjes JP, van Tuel M, Sillessen M, Rietveld G (2009) Fuel Cells 9:873
126. Rossmeisl J, Bessler WG (2008) Solid State Ionics 178:1694
127. Gross MD, Vohs JM, Gorte RJ (2007) J Mater Chem 17:3071

128. Kiratzis NE, Connor P, Irvine JTS (2010) J Electroceram 24:270
129. Nikolla E, Schwank J, Linic S (2009) J Am Chem Soc 131:2747
130. Hornés A, Gamarra D, Munuera G, Conesa JC, Martínez-Arias A (2007) J Power Sources 169:9
131. Sakai T, Zhong H, Eto H, Ishihara T (2010) J Solid State Electrochem 14:1777
132. Sholklapper TZ, Jacobson CP, Visco SJ, De Jonghe LC (2008) Fuel Cells 8:303
133. Deleebeeck L, Fournier JL, Birss V (2010) Solid State Ionics 181:1229
134. Chen XJ, Liu QL, Chan SH, Brandon NP, Khor KA (2007) J Electrochem Soc 154:B1206
135. Jiang SP, Chen XJ, Chan SH, Kwok JT, Khor KA (2006) Solid State Ionics 177:149
136. Aguadero A, de la Calle C, Alonso JA, Pérez-Coll D, Escudero MJ, Daza L (2009) J Power Sources 192:78
137. Blennow P, Hansen KK, Wallenberg LR, Mogensen M (2009) Solid State Ionics 180:63
138. Ruiz-Morales JC, Canalez-Vazquez J, Marrero-López D, Irvine JTS, Núñez P (2007) Electrochim Acta 52:7217
139. Marrero-López D, Peña-Martínez J, Ruiz-Morales JC, Gabás M, Núñez P, Aranda MAG, Ramos-Barrado JR (2010) Solid State Ionics 180:1672
140. Chen XJ, Liu QL, Khor KA, Chan SH (2007) J Power Sources 165:34
141. Zhang L, Chen X, Jiang SP, He HQ, Xiang Y (2009) Solid State Ionics 180:1076
142. Liu J, Madsen B, Ji Z, Barnett S (2002) Electrochem Solid-State Lett 5:A122
143. van den Bossche M, Matthews R, Lichtenberger A, McIntosh S (2010) J Electrochem Soc 157:B392
144. van den Bossche M, McIntosh S (2008) J Catal 255:313
145. Lay E, Gauthier G, Rosini S, Savaniu C, Irvine JTS (2008) Solid State Ionics 179:1562
146. Tao S, Irvine JTS (2004) Chem Mater 16:4116
147. Bernuy-Lopez C, Allix M, Bridges CA, Claridge JB, Rosseinsky MJ (2007) Chem Mater 19:1035
148. Tsipis EV, Kharton VV, Vyshatko NP, Shaula AL, Frade JR (2003) J Solid State Chem 176:47
149. Yano M, Tomita A, Sano M, Hibino T (2007) Solid State Ionics 177:3351
150. Kuhn M, Napporn TW (2010) Energies 3:57
151. Riess I (2008) J Power Sources 175:325
152. Ruiz de Larramendi I, Lamas DG, Cabezas MD, Ruiz de Larramendi JI, Walsöe de Reca NE, Rojo T (2009) J Power Sources 193:77
153. Morel B, Roberge R, Savoie S, Napporn TW, Meunier M (2009) J Power Sources 186:89
154. Nagao M, Yano M, Okamoto K, Tomita A, Uchiyama Y, Uchiyama N, Hibino T (2008) Fuel Cells 8:322
155. Morales M, Piñol S, Segarra M (2009) J Power Sources 194:961
156. Cabezas MD, Lamas DG, Bellino MG, Fuentes RO, Walsöe de Reca NE, Larrondo SA (2009) Electrochem Solid-State Lett 12:B34
157. Kuhn M, Napporn TW, Meunier M, Vengallatore S, Therriault D (2009) J Power Sources 194:941
158. Wei B, Lü Z, Huang X, Liu M, Jia D, Su W (2009) Electrochem Commun 11:347
159. Zhang C, Zheng Y, Ran R, Shao Z, Jin W, Xua N, Ahn J (2008) J Power Sources 179:640
160. Shao Z, Haile SM, Ahn J, Ronney PD, Zhan Z, Barnett SA (2005) Nature 435:795
161. Tomita A, Hirabayashi D, Hibino T, Nagao N, Sano M (2005) Electrochem Solid-State Lett 8:A63
162. Morel B, Roberge R, Savoie S, Napporn TW, Meunier M (2007) Applied Catal A 323:181
163. Hibino T, Hashimoto A, Inoue T, Tokuno J, Yoshida S, Sano M (2000) J Electrochem Soc 147:2888
164. Fisher JC II, Chuang SSC (2009) Catal Commun 10:772
165. Shao Z, Mederos J, Chueh WC, Haile SM (2006) J Power Sources 162:589
166. Kellogg ID, Koylu UO, Petrovsky V, Dogan F (2009) Int J Hydrogen Energy 34:5138
167. Buergler BE, Siegrist ME, Gauckler LJ (2005) Solid State Ionics 176:1717
168. Asahara S, Michiba D, Hibino M, Yao T (2005) Electrochem Solid-State Lett 8:A449
169. Asano K, Hibino T, Iwahara H (1995) J Electrochem Soc 142:3241
170. Hibino T, Asano K, Iwahara H (1994) Chem Lett 3:485
171. van Rij LN, Le J, van Landschoot RC, Schoonman J (2001) J Mater Sci 36:1069
172. Hibino T, Hashimoto A, Inoue T, Tokuno JI, Yoshida SI, Sano M (2000) Science 288:2031
173. Priestnall MA, Kotzeva VP, Fish DJ, Nilsson EM (2002) J Power Sources 106:21
174. Wang Z, Lü Z, Wei B, Huang X, Chen K, Liu M, Pan W, Su W (2010) Electrochem Solid-State Lett 13:B14
175. Akhtar N, Decent SP, Kendall K (2009) Int J Hydrogen Energy 34:7807
176. Akhtar N, Decent SP, Kendall K (2010) J Power Sources 195:7796
177. Evans A, Bieberle-Hütter A, Galinski H, Rupp JLM, Ryll T, Scherrer B, Tölke R, Gauckler LJ (2009) Monatsh Chem 140:975
178. Kuhn M, Napporn TW, Meunier M, Therriault D (2008) J Electrochem Soc 155:B994
179. Kuhn M, Napporn TW, Meunier M, Therriault D (2010) Solid State Ionics 181:332
180. Fleig J, Tuller HL, Maier J (2004) Solid State Ionics 174:261
181. Beckel D, Briand D, Bieberle-Hütter A, Courbat J, de Rooij NF, Gauckler LJ (2007) J Power Sources 166:143
182. Johnson AC, Lai B-K, Xiong H, Ramanathan S (2009) J Power Sources 186:252
183. Joo JH, Choi GM (2009) Solid State Ionics 180:839
184. Joo JH, Kim DY, Choi GM (2009) Electrochem Solid-State Lett 12:B65
185. Xiong H, Lai B-K, Johnson AC, Ramanathan S (2009) J Power Sources 193:589
186. Tsuchiya M, Lai B-K, Johnson AC, Ramanathan S (2010) J Power Sources 195:994
187. Yan Y, Rey-Mermet S, He ZB, Deng G, Muralt P (2009) Procedia Chem 1:1207
188. Doraswami U, Shearing P, Droushiotis N, Li K, Brandon NP, Kelsall GH (2009) Solid State Ionics. doi:10.1016/j.ssi.2009.10.013
189. Akhtar N, Decent SP, Kendall K (2010) J Power Sources 195:7818
190. Akhtar N, Decent SP, Loghin D, Kendall K (2009) J Power Sources 193:39
191. Luebbe H, Van Herle J, Hofmann H, Bowen P, Aschauer U, Schuler A, Snijkers F, Schindler H-J, Vogt U, Lalanne C (2009) Solid State Ionics 180:805
192. Roy BR, Sammes NM, Suzuki T, Funahashi Y, Awano M (2009) J Power Sources 188:220
193. Soderberg JN, Sun L, Sarkar P, Birss VI (2009) J Electrochem Soc 156:B721
194. Yang C, Li W, Zhang S, Bi L, Peng R, Chen C, Liu W (2009) J Power Sources 187:90
195. Yamaguchi T, Shimizu S, Suzuki T, Fujishiro Y, Awano M (2009) Electrochem Solid-State Lett 12:B151
196. Yamaguchi T, Shimizu S, Suzuki T, Fujishiro Y, Awano M (2009) J Am Ceram Soc 92:S107

197. Lawlor V, Griesser S, Buchinger G, Olabi AG, Cordiner S, Meissner D (2009) J Power Sources 193:387
198. Tuller HL, Litzelman SJ, Jung WC (2009) Phys Chem Chem Phys 11:3023
199. Mogensen M, Kammer K (2003) Annu Rev Mater Res 33:321
200. Pillai M, Lin Y, Zhu H, Kee RJ, Barnett SA (2010) J Power Sources 195:271
201. Pillai MR, Bierschenk DM, Barnett SA (2008) Catal Lett 121:19
202. Asamoto M, Miyake S, Sugihara K, Yahiro H (2009) Electrochem Commun 11:1508
203. Huang T-J, Huang M-C (2009) Chem Eng J 155:333
204. Jin C, Yang C, Zhao F, Coffin A, Chen F (2010) Electrochem Commun 12:1450
205. Klein J-M, Hénault M, Roux C, Bultel Y, Georges S (2009) J Power Sources 193:331
206. Ihara M, Hasegawa S, Saito H, Jin Y (2007) ECS Trans 7:1733
207. Tagawa Y, Saito H, Ihara M (2008) ECS Trans 16:287
208. Cao DX, Sun Y, Wang GL (2007) J Power Sources 167:250
209. Tao T (2004) US Patent 6692861
210. Nürnberger S, Bußar R, Desclaux P, Franke B, Rzepka M, Stimming U (2010) Energy Environ Sci 3:150
211. Gür TM (2010) J Electrochem Soc 157:B751
212. Lee AC, Mitchell RE, Gür TM (2009) J Power Sources 194:774
213. Li S, Lee AC, Mitchell RE, Gür TM (2008) Solid State Ionics 179:1549
214. Gür TM, Homel M, Virkar AV (2010) J Power Sources 195:1085
215. Lipilin AS, Balachov II, Dubois LH, Sanjurjo A, McKubre MC, Crouch-Baker S, Hornbostel MD, Tanzclla FL (2005–2007) Patent applications WO2005114770-A1; US2006/019132-A1; EP1756895-A1; AU2005246876-A1; CN1969415-A; IN200604273-P4; US2007/0269688-A1; BR200511332-A; JP2007538379-W; ZA200609977-A; RU2361329-C2
216. Balachov I, Wolk R (2010) Patent application US2010159295-A1
217. Pointon K, Lakeman B, Irvine J, Bradley J, Jain S (2006) J Power Sources 162:750
218. Jain SL, Lakeman JB, Pointon KD, Irvine JTS (2007) ECS Trans 7:829
219. Jain SL, Nabae Y, Lakeman BJ, Pointon KD, Irvine JTS (2008) Solid State Ionics 179:1417
220. Jain SL, Lakeman JB, Pointon KD, Marshall R, Irvine JTS (2009) Energy Environ Sci 2:687
221. Tao TT, Bai W, Rackey S, Wang G (2003) Int patent application WO/2003/001617
222. Tao TT, McPhee WA, Koslowske MT, Bateman LS, Slaney MJ, Bentley J (2008) ECS Trans 12:681
223. Tao T, Bateman L, Bentley J, Slaney M (2007) ECS Trans 5:463
224. Bronin DI, Karpachev SV, Sal'nikov VV (1982) Sov Electrochem 18:1299
225. Jayakumar A, Lee S, Hornés A, Vohs JM, Gorte RJ (2010) J Electrochem Soc 157:B365
226. Norby T (2007) J Chem Eng Japan 40:1166
227. Yang L, Wang S, Blinn K, Liu M, Liu Z, Cheng Z, Liu M (2009) Science 326:126
228. Haugsrud R, Norby T (2006) Nat Mater 5:193
229. Fontaine M-L, Larring Y, Haugsrud R, Norby T, Wiik K, Bredesen R (2009) J Power Sources 188:106
230. Kharton VV, Marozau IP, Mather GC, Naumovich EN, Frade JR (2006) Electrochim Acta 51:6389
231. Brandao AD, Antunes I, Frade JR, Torre J, Kharton VV, Fagg DP (2010) Chem Mater 22:6673
232. Bhella SS, Thangadurai V (2009) J Electrochem Soc 156:B634
233. Dailly J, Fourcade S, Largeteau A, Mauvy F, Grenier JC, Marrony M (2010) Electrochim Acta 55:5847
234. Chevallier L, Zunic M, Esposito V, Di Bartolomeo E, Traversa E (2009) Solid State Ionics 180:715
235. Taillades G, Dailly J, Taillades-Jacquin M, Mauvy F, Essouhmi A, Marrony M, Lalanne C, Fourcade S, Jones DJ, Grenier J-C, Rozière J (2010) Fuel Cells 10:166
236. Baker RT, Salar R, Potter AR, Metcalfe IS, Sahibzada M (2009) J Power Sources 191:448
237. Azimova MA, McIntosh S (2009) Solid State Ionics 180:160
238. Peng R, Wu T, Liu W, Liu X, Meng G (2010) J Mater Chem 20:6218
239. Ding H, Xue X (2010) Int J Hydrogen Energy 35:2486
240. Xu J, Lu X, Ding Y, Chen Y (2009) J All Compd 488:208
241. Sunding MF, Kepaptsoglou DM, Diplas S, Norby T, Gunnæs AE (2010) Surf Interface Anal 42:568
242. Quarez E, Noirault S, Le Gal La Salle A, Stevens P, Joubert O (2010) J Power Sources 195:4923
243. Patcharavorachot Y, Paengjuntuek W, Assabumrungrat S, Arpornwichanop A (2010) Int J Hydrogen Energy 35:4301
244. Perfilyev MV, Demin AK, Kuzin BL, Lipilin AS (1988) High-temperature electrolysis of gases. Nauka, Moscow
245. Ni M, Leung MKH, Leung DYC (2008) Int J Hydrogen Energy 33:2337
246. Hauch A, Ebbesen SD, Jensen SH, Mogensen M (2008) J Mater Chem 18:2331
247. Graves C, Ebbesen SD, Mogensen M, Lackner KS (2011) Renewable Sus Energy Rev 15:1
248. Brisse A, Schefold J, Zahid M (2008) Int J Hydrogen Energy 33:5375
249. Herring JS, O'Brien JE, Stoots CM, Hawkes GL, Hartvigsen JJ, Shahnam M (2007) Int J Hydrogen Energy 32:440
250. Laguna-Bercero MA, Kilner JA, Skinner SJ (2010) Solid State Ionics. doi:10.1016/j.ssi.2010.01.003
251. Chauveau F, Mougin J, Bassat JM, Mauvy F, Grenier JC (2010) J Power Sources 195:744
252. Graves C, Ebbesen SD, Mogensen M (2010) Solid State Ionics. doi:10.1016/j.ssi.2010.06.014
253. Kim-Lohsoontorn P, Brett DJL, Laosiripojana N, Kim Y-M, Bae J-M (2010) Int J Hydrogen Energy 35:3958
254. Bo Y, Wenqiang Z, Jingming X, Jing C (2010) Int J Hydrogen Energy 35:2829
255. Osinkin DA, Kuzin BL, Bogdanovich NM (2009) Russ J Electrochem 45:483
256. Ishihara T, Jirathiwathanakul N, Zhong H (2010) Energy Environ Sci 3:665
257. Ishihara T, Kannou T (2010) Solid State Ionics. doi:10.1016/j.ssi.2010.06.020
258. Liu Q, Yang C, Dong X, Chen F (2010) Int J Hydrogen Energy 35:10039
259. Yamaji K, Horita T, Ishikawa M, Sakai N, Yokokawa H (2009) Solid State Ionics 121:217
260. Patrakeev MV, Leonidov IA, Kozhevnikov VL, Kharton VV (2004) Solid State Sci 6:907
261. Yang X, Irvine JTS (2008) J Mater Chem 18:2349
262. Schiller G, Ansar A, Lang M, Patz O (2009) J Appl Electrochem 39:293
263. Ebbesen SD, Graves C, Hauch A, Jensen SH, Mogensen M (2010) J Electrochem Soc 157:B1419
264. Wang Z, Mori M, Araki T (2010) Int J Hydrogen Energy 35:4451
265. Mawdsley JR, Carter JD, Kropf AJ, Yildiz B, Maroni VA (2009) Int J Hydrogen Energy 34:4198
266. Virkar AV (2010) Int J Hydrogen Energy 35:9527
267. Jensen SH, Sun X, Ebbesen SD, Knibbe R, Mogensen M (2010) Int J Hydrogen Energy 35:9544
268. Koh J-H, Yoon D-J, Oh CH (2010) J Nucl Sci Tech 47:599
269. Lee AC, Mitchell RE, Gür TM (2010) Solid State Ionics. doi:10.1016/j.ssi.2010.05.034
270. Huang T-J, Chou C-L (2009) Electrochem Commun 11:477
271. Fu X-Z, Luo J-L, Sanger AR, Xu Z-R, Chuang KT (2010) Electrochim Acta 55:1145